technische universität
dortmund

Optical properties of vacancies in diamond at high magnetic fields

Dissertation

submitted in partial fulfillment of
the requirements for the degree of

Dr. rer. nat.

to the Faculty of Physics
TU Dortmund University, Germany

by

Dion Braukmann

Dortmund, April 2018

Date of the oral examination: 19th April 2018

Examination board:

Dr. Jörg Debus
Prof. Dr. Heinz Hövel
Prof. Dr. Shaukat Khan
Dr. Bärbel Siegmann

Contents

Summary

Polarization resolved photoluminescence spectroscopy measurements are performed on defect centers in diamond. The photoluminescence of the negatively charged as well as the neutral nitrogen vacancy center shows remarkable linear polarization degrees of about 20 % at room temperature. The anisotropic angular dependence of the linear polarization characteristics mirrors the crystallographic symmetry of the defect center. In contrast to the linear polarization, the circular polarization properties of the defect centers are rather weak due to the small orbital g-factors of the defect center electrons. The latter were measured via the Zeeman splitting of the defect center's zero-phonon lines, which also allows to define the symmetry and energetic ordering of the defect center energy levels.

A Fano resonance in the energy of the nitrogen vacancy center zero-phonon lines is observed via photoluminescence-excitation spectroscopy. This resonance is accompanied by a charge transfer between the two charge states of the nitrogen vacancy center which leads to an increase in the photoluminescence intensity of up to a factor of 30. It is shown that this recharging process is more important in diamonds with low nitrogen vacancy center concentration, while in diamonds with high concentration the recharging occurs via nitrogen impurities, which act as electron donors.

In addition, optical detection of magnetic resonances via application of microwaves with powers in the range of only a few nanowatts demonstrates the high sensitivity of the negatively charged nitrogen vacancy center to microwave radiation. Moreover, microwave amplification at nitrogen impurities might viably have been observed in the diamond crystal, which could make the diamond a possible candidate for a solid state maser that operates at room temperature.

Motivation

The investigation of impurities in diamond started in the early forties of the 20^{th} century. It was found that irradiation of diamond with high energetic photons, radioactive radiation, or particle beams, such as deuteron ions accelerated by a cyclotron, induces distinct color changes.[1] Techniques for synthetic diamond fabrication[2] developed in the fifties, facilitated the characterization of impurities in diamond by optical absorption[3, 4] and later also by electronic paramagnetic resonance.[5] However, the identification of the observed absorption bands with the corresponding defect centers took several years. One of these centers was the negatively charged nitrogen vacancy center,[6] which turned out to be suitable for observing electron spin resonance[7] and optically detected magnetic resonance. The latter was firstly reported by Eric van Oort et. al.[8, 9] in the late eighties and lead the path to a wide range of applications.

Although other defects in diamond show magnetic resonances as well,[10] it was the negatively charged nitrogen vacancy center which revealed itself to be the most promising spin system. Due to the coupling of the nitrogen vacancy centers' electronic spin to the nuclear spins of the ^{14}N and ^{13}C atoms[11, 12] surrounding the vacancy, remarkable coherence times, exceeding one second at room temperature, can be achieved via decoupling of the nuclear spin from the environment.[13] These long coherence times[14] as well as the temperature robustness make the negatively charged nitrogen vacancy center highly suitable for quantum information applications.

The ground state of the defect center can be simplified as a two-level quantum-mechanical system, and therefore it can serve as a qubit.[15] For instance, quantum registers[16] as well as entanglement[17] were already realized a few years ago. Since then methods of sample engineering have advanced. Ultrapure diamonds with single nitrogen vacancy centers[18] as well as accurately designed arrays of defect centers[19] can be grown allowing high-fidelity control of the qubit.[13, 20]

Moreover, the negatively charged nitrogen vacancy center in diamond is, due to its remarkable magneto-optical properties, a highly precise sensor for electric[21] and magnetic fields[22] as well as for crystal strain,[23] which offers a wide field of applications. For instance, simultaneous optical and magnetic imaging of living magnetotactic bacteria were performed with submicrometer resolution.[24] Embedded in single nanometer-sized diamonds, nitrogen vacancy center based sensors provide new possibilities for quantum based imaging in life science as well.[25, 26, 27]

Despite the fact, that the extensive research on the negatively charged nitrogen

vacancy center has persisted for almost a decade, its electronic structure has yet to be studied to be fully understood. Especially the neutral charge state of the nitrogen vacancy center is less investigated and neglected in most studies, although it is known that there is a charge state switching between neutral and negatively charged defect centers.[28] This charge state switching is particularly pronounced in high purity diamonds, which are used for most quantum information or sensing applications. Moreover, the optical properties of other quite common impurities, like substitutional nitrogen or single vacancy centers are rarely considered.

In this work optical characterization of the different charge states of the nitrogen vacancy center as well as the neutral single vacancy center in diamond are presented. By means of polarization measurements of the optical transitions, the energetic ordering, and the symmetry of the energy level structure of these defect centers is investigated and compared to current theoretical models and experimental observations. In Chapter 1 the physical properties of the host material diamond as well as a selection of the numerous defect centers are presented. Special focus is drawn to the electron structure of the negatively charged nitrogen vacancy center, which will be evolved via group theoretical methods. Moreover, the energy level structures and the optical transitions of the other investigated defect centers are discussed. A detailed exposition of the experimental methods of polarization sensitive photoluminescence and of photoluminescence excitation spectroscopy as well as of high frequency optically detected magnetic resonance is given in Chapter 2. In addition to that, the studied diamond crystal samples are briefly characterized by optical methods as well as X-ray diffraction.

In Chapter 3 the circular polarization properties of the examined defect centers are discussed. In this regard, the polarization characteristics of the defect center zero phonon lines are compared to theoretical expectations which arise from the energy states' symmetries. Subjected to high magnetic fields, effective orbital g-factors can be estimated by analyzing the Zeeman shift of the defect center photoluminescence. Subsequently, the linear polarization properties of the defect center photoluminescence are investigated in Chapter 4. The main focus lies on the influence of the crystal and defect center symmetry on the linear polarization of the emitted photoluminescence. In this regard, the polarization of the diamond Raman line will also be evaluated. Furthermore, the dependence of the linear polarization characteristics on excitation power, energy and temperature as well as magnetic field strength are thoroughly analyzed.

In Chapter 5 the observation of a Fano resonance behavior of the zero phonon line energy of the nitrogen vacancy centers via spectrally resolved photoluminescence excitation is demonstrated. The dependences of this resonance on excitation power, temperature, and magnetic field strength are presented. Additionally, the influence of nitrogen vacancy center recharging on the intensity of the zero phonon lines is revealed. In Chapter 6 the optical response of the negatively charged nitrogen vacancy to ultra low power microwave excitation is shown. In this context, the principle of optically detected magnetic resonance is discussed. Special focus is drawn to the magnetic resonance shift due to angular deviation of the magnetic field vector with respect to the crystal

symmetry axes. Chapter 7 forms a short outlook on state mixing at low magnetic fields, which provides further insight into the level structure of the negatively charged nitrogen vacancy centers. The suitability of defect centers in diamond as a medium for microwave amplification by stimulated emission of radiation is discussed in Chapter 8. In this context two experiments to detect microwave emission from a diamond crystal are presented.

Chapter 1

Theoretical background

This chapter provides detailed information on the theoretical background of the optical properties of defect centers in diamond. Firstly, the host material diamond is presented. In this context, the manufacturing of artificial diamonds is covered as well as the controlled creation of defect centers. The main focus lies on the negatively charged nitrogen vacancy center (NV^-), but also the neutral nitrogen vacancy center (NV^0) as well as the neutral single vacancy (V^0) center are discussed. The electronic structure of the NV^- center is developed in detail, using molecule orbital theory via a group theoretical approach, whereas the electronic structure of the NV^0 and the V^0 are presented only briefly. A closer look is taken at the optical transitions between the energetic levels of the defect centers. In this context, the zero-phonon lines (ZPLs) are of highest interest, since they are the most prominent features in the spectra of the defect centers which were studied.

1.1 The diamond crystal

Before introducing the various defect centers, which have been intensely researched in the recent decades, the focus will be directed at the host material diamond. It is one of the most famous gemstones due to its charming appearance, as well as the hardest naturally occurring material. In addition to that, it is the mineral with the highest thermal conductivity. Hence, diamond has several applications in modern technologies. As a cutting tool material diamond is used in drill bits or milling cutters, as well as in magnetic cartridge needles of high quality phonographs.

Diamond is a distinct crystalline modification of carbon. The four valence electrons of the sp^3-hybridized carbon atoms (C-atoms) covalently bond with the neighboring electrons, forming a face centered cubic (fcc) lattice with basis $\{(1,1,1)$ and $\left(\frac{1}{4},\frac{1}{4},\frac{1}{4}\right)\}$.[29] This lattice structure is also called the diamond structure. The covalent bonds are the reason for the diamond crystal's high stiffness. Due to the completely saturated valance electrons, the band gap energy is about 5.48 eV, making diamond an insulator which is transparent for visible light. This makes the material unsuitable for optical spectroscopy, since optical excitation in the visible range is in general too low in energy

to excite transitions between the valance (VB) and conduction band (CB).

However, impurities in the diamond lattice can lead to a coloring, and thus make the crystal excitable by visible light. Therefore, diamond is an interesting material for optical spectroscopy. Dependent on the nature of the impurity, the diamond can adopt various colors. Nitrogen leads to a yellow coloring, while boron impurities give a blue and lattice defects, like the single vacancy, a green or brown color.[30, 31] Such defects appear in natural as well as artificial diamond crystals.

In nature, diamonds are formed under high temperature and pressure, several hundred kilometers deep in the lithospheric mantle of the earth, when diamond is the stable configuration of carbon according to its phase diagram. Such natural growth, however, takes billions of years.[32] In order to artificially create diamonds, the growth conditions must be simulated. This method is called high pressure high temperature synthesis (HPHT) and involves heavy presses which can apply a pressure of $5{\cdot}10^4$ bar at a temperature of 1500°C.[2, 33] An alternative is chemical vapor deposition (CVD), a homoepitaxial technique in which the crystal is grown on a diamond seed layer in a plasma growth chamber at a pressure of about 30 mbar and at a temperature of 800°C.[34, 35] Under these conditions the preferred configuration of carbon is graphite, whereas diamond is just metastable. However, the plasma which mainly contains hydrogen or deuterium atoms with a minor amount of methane etches the graphite away and dangling bonds are created at the surface of the diamond seed crystal. The C-atoms of the methane can bind to these dangling bonds, allowing the diamond to grow layer by layer.

1.2 Defect centers in diamond

Natural as well as artificial diamonds contain imperfections in the crystal lattice. There are various kinds of such impurities, containing vacancies in the carbon lattice and alien atoms, such as the formerly mentioned nitrogen and boron, as well as nickel, silicon, hydrogen, and cobalt.[36] Such defects can affect the physical properties of the crystal, especially the electrical conductivity and the color. The latter is most important for optical characterization of the diamond crystal and identification of the impurity. For instance the defect type and density can be identified by infrared absorption.[37]

Due to the crystal symmetry of the diamond, the defect centers have distinct symmetry too. Usually, these symmetries are described by point groups, which indicate certain groups of invariant symmetry operations.[38, 39] It is common to use the Schoenflies notation, for instance T_d indicates a tetrahedral, D_{2d} a tetragonal and C_3 a trigonal symmetry.[40] Due to the defect, the symmetry of the diamond lattice is disturbed, this symmetry reduction can lead to infrared absorption, which is forbidden in pure diamond due to the inversion symmetry of the lattice.[30]

In order to characterize diamonds and to associate optical features, like absorption or emission lines with certain defect centers, the lines were labeled according to attributes of the investigated samples. For example, lines which were observed in natural diamonds were labeled N1 to N9, whereas lines which were seen after general irradiation of the

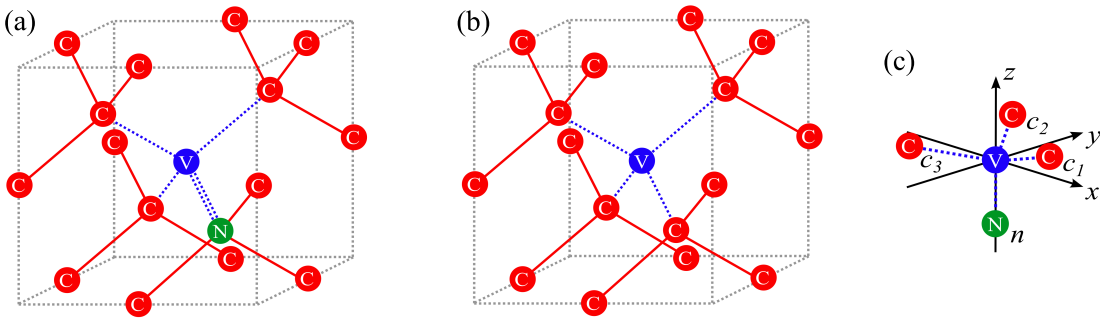

Figure 1-1: Unit cell (gray dotted line) of the diamond lattice with (a) an NV center and (b) a single vacancy defect center. The defect centers consist of an N-atom (green) and vacant lattice sites (blue) in the matrix of the carbon atoms (red). Solid red lines indicate electron-electron bindings between the atoms, whereas dotted blue lines indicate dangling bond electrons that are localized at the vacancies. (c) The NV center with its next neighbor atoms in the coordinate system of the tetrahedral sp^3 orbital.

diamond sample were labeled GR1 to GR8 or H1 to H18 when a certain heat treatment was applied before irradiation.[3]

As a fact, the quality of diamonds is rated by the amount of nitrogen impurities. Purest diamonds, the so called type IIa and IIb diamonds, contain less than one part per million (1 ppm) nitrogen or boron impurities respectively, whereas type Ib and Ia diamonds have a nitrogen impurity concentration of less than 500 and 3000 ppm respectively.[41]

Among the numerous impurities especially defects containing nitrogen show remarkable optical properties. One of the most investigated defect is the nitrogen vacancy (NV) center, which leads to a pink or at high concentrations deep red coloring of the diamond. It consists of a substitutional nitrogen atom (N-atom) with a carbon vacancy located on an adjacent lattice site. The atomic structure of such an NV center is shown in Fig. 1-1 (a). The defect center forms a C_{3v} symmetry group, which means that its symmetry is invariant under rotation of 120° around the symmetry axis z.[39] In case of the NV center, the symmetry axis is defined by the line connecting the vacancy and the N-atom.

For the formation of NV centers a significant amount of nitrogen impurities is essential. In the CVD synthesis for instance, the concentration of nitrogen can be controlled by adding nitrogen gas into the growth chamber. However, most of these N-atoms form single nitrogen defects (also referred as P1 center) or nitrogen clusters, especially at high nitrogen concentrations in type Ia diamonds.

In natural diamonds, NV centers are formed by vacancies migrating to the nitrogen impurities over time. In artificial diamonds this migration process can be enforced by annealing the diamond at about 800°C for some hours.[6] At this temperature the vacancies become mobile and move to the nitrogen impurities, forming NV centers. Especially for high concentration samples not only a high nitrogen density but also a

large amount of vacancies must be present in the diamond crystal. These vacancies can be produced via neutron-, ion- or electron-beam irradiation with energies of several MeV in a depth of a few μm.[42] Using nitrogen ions, implanting nitrogen impurities and creating vacancies can be done simultaneously. Moreover, the engineering of single NV centers or even NV center patterns is possible with a precision of about 10 nm in all three dimensions using focused ion beams[18] or masked implantation.[19] Such precise methods for the fabrication of arrays of single NV centers are essential in the realization of quantum information processing applications in diamond.

In addition to the NV center, this work also focuses on the neutral single vacancy V^0 center. As one can see in Fig. 1-1 (b), this center consists of a single vacancy in the carbon lattice. The defect center forms a T_d point group, which indicates a tetrahedral symmetry, comparable to methane molecules. It can be found in diamonds with a rather low nitrogen concentration which have not been annealed.[43] In contrast to the NV center, the V^0 is poorly investigated. There are some magnetic resonance studies on the dark $^5A_2$ state,[10] but in contrast to that, the research interest in the optically addressable states has been rather low during the last decades. However, the V^0 center was associated with a sharp absorption line, the so called GR1 band, which could be identified with a transition of the first excited and ground state of the center.[44] Nevertheless, a consistent picture of the electron structure has not been established yet.[45]

1.3 Electronic structure of the NV^- center

The NV center appears in different charge states, however, for the optical spectroscopy mostly the neutral NV^0 and the negatively charged NV^- are important, because other charge states are not optically addressable. Since this work mainly focuses on the optical properties of the NV^- center, the electronic structure of this defect will be developed in detail. A consideration of the electronic structure of NV^0 and V^0 will follow afterwards.

The electronic structure is mostly defined by the dangling bond electrons of the four atoms surrounding the vacancy. In contrast to the neutral NV^0, the negatively charged NV^- not only has the five electrons of the nearest neighbor atoms, three unpaired electrons from the C-atom and two from the N-atom, but also one additional captured electron. A detailed analysis of the charging process and the charge transfer between NV^0 and NV^- can be found in 5.4.1. In this context, the concentration of nitrogen defects, since they act as dopant atoms, plays a crucial role. For instance, most NV centers are negatively charged, when the nitrogen concentration is high compared to the NV center density, see 5.1.1. Hence, the NV^- has six electrons and a total charge of -1. These electrons are localized at the vacancy, and therefore the electronic structure can be well explained in terms of molecule orbitals. These orbitals can be constructed from the sp^3 atomic orbitals of the nearest neighbor atoms of the vacancy via group theoretical methods.

This conduction, which will be discussed in the following, was done by M. W. Doherty et al. in [46]. With the basis $\{n,c_1,c_2,c_3\}$, compare Fig. 1-1 (c), the

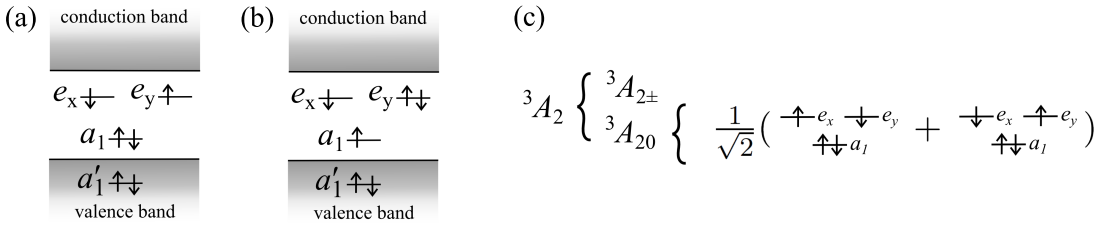

Figure 1-2: Electron occupation of (a) ground and (b) first excited molecule orbitals configuration of the NV^-. The arrows indicate electrons with spin up and down respectively. (c) The ground state triplet $^3A_2$ of the NV^- center consists of the states $^3A_{20}$ and $^3A_{2\pm}$. The state $^3A_{20}$ is the linear combination of two molecule orbital configurations $\Phi_1^{so} = \frac{1}{\sqrt{2}}(|111001\rangle + |110110\rangle)$.

following molecule orbitals can be approximated

$$a_1(N) = n \quad , \tag{1.1}$$

$$a_1(C) = \frac{c_1 + c_2 + c_3 - 3S_{nc}n}{\sqrt{3}\sqrt{1 + 2S_{cc} - 3S_{nc}^2}} \quad , \tag{1.2}$$

$$e_x = \frac{2c_1 - c_2 - c_3}{\sqrt{3}\sqrt{2 - 2S_{cc}}} \quad , \tag{1.3}$$

$$e_y = \frac{c_2 - c_3}{\sqrt{2 - 2S_{cc}}} \quad . \tag{1.4}$$

Here $S_{nc} = \langle n|c_1\rangle$ and $S_{cc} = \langle c_1|c_2\rangle$ are the orbital overlap integrals. Note that the orbitals described by Eq. (1.1) to (1.4) only imply contributions of the nearest neighbors. Moreover, interaction between the defect center molecule orbitals and the electronic orbitals of the crystal atoms is neglected. In addition to that, there is a mixing of the s-like $a_1(N)$ and $a_1(C)$ orbitals, which leads to the formation of the molecule orbitals a_1' and a_1. This lowers the energy of the a_1' orbital into the valance band of diamond. However, the energy of the other orbitals lies in the band gap of the diamond crystal. The electron occupation of the four molecule orbitals $\{a_1', a_1, e_x, e_y\}$ forms the energy states of the NV^- center.

For further consideration only the ground and first excited molecule orbital configuration are of particular interest. In both of these configurations, the lowest molecule orbital a_1' is occupied by two of the total six electrons of the NV center. Differences only lie in the occupation of the other three orbitals. Since the occupation of a_1' does not change, it has no influence on the optical properties of the NV^- center. Therefore, the a_1' orbital will be neglected in the following considerations. In Fig. 1-2 (a) the molecule orbital occupation of the ground configuration ($a_1^2e^2$) is shown. The high index represents the number of electrons in the a_1 and p-like $e_{x,y}$ orbitals respectively. In the first excited molecule orbital configuration ($a_1^1e^3$), which is depicted in Fig. 1-2 (b), one electron is lifted from the a_1 orbital to the e_x or e_y orbital.

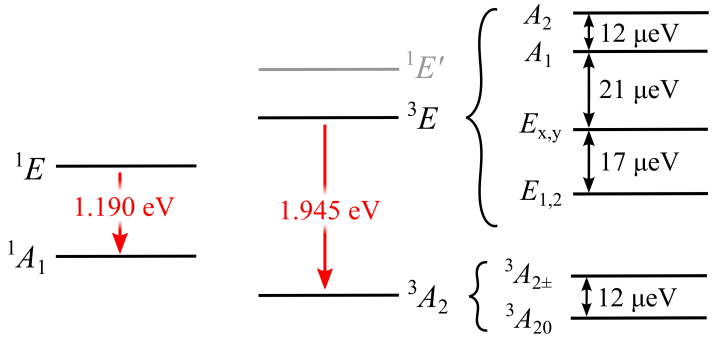

Figure 1-3: Energy level structure of the NV^- center including the fine structure of the triplet states with zero field splitting. Optical transitions (red arrows) can be observed between the triplets ^{3}E and $^3A_2$, as well as the singlets ^1E and $^1A_1$.[50] Note that the optically inactive state $^1E'$ is shaded in gray. The zero field splitting represents typical values for diamond crystals with low NV center density.[17, 51]

Taking the spin-orbit and spin-spin interaction into account, the symmetrized spin orbit states Φ_n^{so} can be constructed as linear combinations of the molecule orbitals defined via Eq. (1.1) to (1.4), weighted with the Clebsch-Gordan coefficients.[47] In table 1-1 these states are described in terms of Slater determinants of the molecule orbitals. The Slater determinant $|a_1\bar{a}_1e_x\bar{e}_xe_y\bar{e}_y\rangle$ indicates the occupation of the three molecule orbitals a_1, e_x and e_y. An entry with or without a bar visualizes an electron with spin up or spin down respectively. The states are ordered by their energy level n. Fig. 1-2 (c) shows how the spin orbit state is defined by the occupation of the molecule orbitals using the example of the NV^- ground state $^3A_2$. As one can see, the $^3A_2$ triplet state consists of the spin 1 states $^3A_{2\pm}$ and the spin 0 state $^3A_{20}$. The latter is a linear combination of the two molecule orbital configurations $|111001\rangle$ and $|110110\rangle$) with the Clebsch-Gordan coefficient $1/\sqrt{2}$. Note that the terminology $^3A_2$ refers to a spin triplet state (high index 3) and the irreducible representation A_2, which indicates a certain symmetry.[39, 48, 49]

The energy level structure, resulting from the unity of the symmetrized spin orbit states is presented in Fig. 1-3. It consist of the two spin triplet states $^3A_2$ and ^3E, as well as the three spin singlet states $^1A_1$, ^1E and $^1E'$.[52] Two optical transitions (red) can be identified, one between the $^3A_2$ and ^3E state with an energy of 1.945 eV[53] and another transition between the ^1E and $^1A_1$ state with an energy of 1.190 eV.[50] The optical transition between the ^3E and the $^3A_2$ state is a so called zero-phonon line, since the emission process itself is not accompanied by the emission or absorption of a phonon, which in turn means that the emission process of the ZPL is spin conserving. The ZPL is accompanied by a broad phonon side band (PSB) with its maximum at about 1.8 eV, which is especially prominent at high temperature, whereas at low temperature the NV^- ZPL is dominant. Spectra at room temperature are shown in Fig. 2-5 for diamond samples with various NV center concentrations and a spectrum at cryogenic

			Φ_n^{so}		
$a_1^2e^2$	$^3A_2$	$^3A_{20}$	Φ_1^{so}	=	$\frac{1}{\sqrt{2}}(\|111001\rangle + \|110110\rangle)$
		$^3A_{2+}$	Φ_{2x}^{so}	=	$\frac{-1}{\sqrt{2}}(-\|110101\rangle + \|111010\rangle)$
		$^3A_{2-}$	Φ_{2y}^{so}	=	$\frac{-i}{\sqrt{2}}(\|110101\rangle + \|111010\rangle)$
	^1E	$^1E_1$	Φ_{3x}^{so}	=	$\frac{1}{\sqrt{2}}(\|111100\rangle - \|110011\rangle)$
		$^1E_2$	Φ_{3y}^{so}	=	$\frac{1}{\sqrt{2}}(\|110110\rangle - \|111001\rangle)$
	$^1A_1$	$^1A_1$	Φ_4^{so}	=	$\frac{1}{\sqrt{2}}(\|111100\rangle + \|110011\rangle)$
a_1e^3	^3E	E_1	Φ_{5x}^{so}	=	$\frac{1}{2}[-i(\|101011\rangle + \|010111\rangle) - (-\|101110\rangle + \|011101\rangle)]$
		E_2	Φ_{5y}^{so}	=	$\frac{1}{2}[-(-\|101011\rangle + \|010111\rangle) + i(\|101110\rangle + \|011101\rangle)]$
		E_x	Φ_{6x}^{so}	=	$\frac{-1}{\sqrt{2}}(\|101101\rangle + \|011110\rangle)$
		E_y	Φ_{6y}^{so}	=	$\frac{1}{\sqrt{2}}(\|100111\rangle + \|011011\rangle)$
		A_1	Φ_7^{so}	=	$\frac{1}{2}[(-\|101011\rangle + \|010111\rangle) + i(\|101110\rangle + \|011101\rangle)]$
		A_2	Φ_8^{so}	=	$\frac{1}{2}[-i(\|101011\rangle + \|010111\rangle) + (-\|101110\rangle + \|011101\rangle)]$
	$^1E'$	$^1E'_1$	Φ_{9x}^{so}	=	$\frac{1}{\sqrt{2}}(\|100111\rangle - \|011011\rangle)$
		$^1E'_2$	Φ_{9y}^{so}	=	$\frac{1}{\sqrt{2}}(\|101101\rangle - \|011110\rangle)$

Table 1-1: Symmetrized spin orbit states Φ_n^{so} of the NV^- center. The occupation of the molecule orbitals is defined by the Slater determinate $|a_1\bar{a}_1e_x\bar{e}_xe_y\bar{e}_y\rangle$. An entry with or without a bar indicates an electron with spin up or spin down respectively, occupying the corresponding molecule orbital. Where a 1 indicates an occupied and a 0 a free electronic state.

temperature is depicted in Fig. 2-7 for a sample with rather low NV center density.

The other optical transition between the ^1E and $^1A_1$ state is spin conserving as well. The whole emission process involves a relaxation from the excited ^3E state to the intermediate ^1E state, which is not spin conserving, as well as a relaxation from the intermediate $^1A_1$ state to the ground state $^3A_{20}$. Therefore, the total transition via the intermediate states is not spin conserving. Hence, a spin polarization into $m_S = 0$ occurs after some excitation circles.[54] It is worthwhile mentioning that the energetic ordering of the singlet states is not completely understood, since there is evidence that $^1A_1$ is in fact higher in energy than ^1E.[55] A detailed discussion about the correct energetic ordering will be made in Sec. 3.1.3 and Chapter 7. In contrast to the NV^- ZPL, the singlet states transition (SST) and its optical properties are barely investigated. Despite the fact that the SST was identified in 2008,[50] when the research interest in the NV^-

center began to increase in the physics community, most optical methods still focus on the ZPL at 1.945 eV and the corresponding PSB.

Since this work focuses on the optical properties of defect centers in the visible range, the optical transition between the two triplet states is of particular interest. Nevertheless, also the SST will be discussed on account of its circular polarization properties in Chapter 3. However, for now, the focus lies on the ZPL. Therefore, only the triplet states will be considered in detail, whereas the singlet states will be mostly neglected for further considerations. A mathematically more compact way to describe the relevant states are the orbital functions

$$|E_0\rangle = |e_x e_y - e_y e_x\rangle \quad \text{and} \tag{1.5}$$
$$|E_\pm\rangle = |a_1(\mp e_x - i e_y) - (\mp e_x - i e_y) a_1\rangle \quad . \tag{1.6}$$

The index stands for the contribution of the orbital angular momentum to the total angular momentum of the orbital, in this context $\pm$ stands for ± 1. By using the spin states $|0\rangle$ and $|\pm 1\rangle$, which describe the total angular momentum of the spin orbit state, the relevant states can be written as a linear combination of orbital function and spin state:

$$|^3\mathrm{A}_{20}\rangle = |E_0\rangle\,|0\rangle \quad , \tag{1.7}$$
$$|^3\mathrm{A}_{2+}\rangle = |E_0\rangle\,|+1\rangle \quad , \tag{1.8}$$
$$|^3\mathrm{A}_{2-}\rangle = |E_0\rangle\,|-1\rangle \quad , \tag{1.9}$$
$$|\mathrm{E}_1\rangle = \frac{1}{\sqrt{2}}(|E_-\rangle\,|-1\rangle - |E_+\rangle\,|+1\rangle) \quad , \tag{1.10}$$
$$|\mathrm{E}_2\rangle = \frac{1}{\sqrt{2}}(|E_-\rangle\,|-1\rangle + |E_+\rangle\,|+1\rangle) \quad , \tag{1.11}$$
$$|\mathrm{E}_x\rangle = \frac{1}{2}(|E_-\rangle + |E_+\rangle)\,|0\rangle \quad , \tag{1.12}$$
$$|\mathrm{E}_y\rangle = \frac{i}{2}(|E_-\rangle - |E_+\rangle)\,|0\rangle \quad , \tag{1.13}$$
$$|\mathrm{A}_1\rangle = \frac{1}{\sqrt{2}}(|E_-\rangle\,|+1\rangle - |E_+\rangle\,|-1\rangle) \quad , \tag{1.14}$$
$$|\mathrm{A}_2\rangle = \frac{1}{\sqrt{2}}(|E_-\rangle\,|+1\rangle + |E_+\rangle\,|-1\rangle) \quad . \tag{1.15}$$

The main advantage of this compact description is that the total spin and the orbital angular momentum can be seen directly. This is of particular interest when discussing the polarization properties of the ZPL, especially in the presence of an external magnetic field. A detailed discussion will follow in Sec. 3.1.1, in which the optical selection rules and the resulting ZPL polarization will be presented; not only for the NV^- centers but also for the NV^0 and the V^0 centers. The latter neutral defect centers and their energy structure will now be discussed.

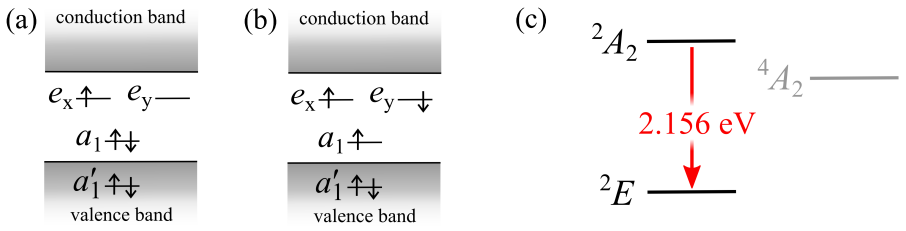

Figure 1-4: Electron occupation of (a) ground and (b) first excited molecule orbitals configuration of the NV^0 center. The arrows indicate electrons with spin up and down respectively. (c) Energy level structure of the NV^0 center. An optical transition (red arrow) can be observed between the doublets ^2E and $^2A_2$. The gray shaded $^4A_2$ state does not show an optical transition.

1.4 Electronic structure of the NV^0 and V^0 center

In addition to the negatively charged NV^-, also the neutral NV^0 center is of particular interest in this work, since Chapter 5 focuses on the interaction between these two charge states. The main difference between these two centers is that the NV^0 has one electron less. The five electrons are the unpaired electrons of the C- and N-atoms adjacent to the vacancy. However, the symmetry of the defect center is basically the same, hence the group theoretical approach to gain the molecule orbitals can easily be adopted.[56, 57] With two electrons occupying the a_1' molecule orbital, the orbital occupation of the ground configuration is $a_1^2e^1$, whereas the first excited molecule orbital configuration is $a_1^1e^2$, as shown in Fig. 1-4 (a) and (b). Note that the energy of the molecule orbitals is slightly different compared to the NV^-.[58]

Analog to the NV^-, an energy level structure can be constructed for the NV^0 center too. As one can see in Fig. 1-4 (c), it consists of the ground state ^2E and the first excited state $^2A_2$, which are both spin doublets, as well as the intermediate spin quadruplet state $^4A_2$.[59] There is only an optical transition between the two doublet states. Similarly to the NV^- center this transition with an energy of 2.156 eV is a ZPL too.

Besides the two optically active charge states of the NV center, the neutral single vacancy center V^0 should be considered also. The V^0 has four electrons, located at the vacancy. Due to the T_d symmetry, these electrons occupy the s-like a_1 and the p-d-like t_2 molecule orbitals,[10] compare Fig. 1-5 (a) and (b). The configuration $a_1^1t_2^2$ gives rise to the states $^1A_1$, ^1E, $^3T_1$, and $^1T_2$, whereas the configuration $a_1^1t_2^3$ gives rise to the states $^5A_2$, $^3A_2$, ^3E, ^1E, $^3T_1$, $^1T_1$, $^3T_2$, and $^1T_2$.[60, 10] The energetic ordering of these states is not established so far. Most magnetic resonance studies focus on the spin triplet state $^5A_2$, but a detailed picture of the electronic structure is missing so far.[45] In the frame of this work, only the optically active states will be discussed. The reduced level structure of the V^0 is illustrated in Fig. 1-5 (c). The ground states $^1A_1$ and ^1E, as well as the first excited state $^1T_2$ are spin singlets. There are two distinct ZPLs, one at about 1.674 eV from the $^1T_2$ excited state to the ^1E ground state and a second

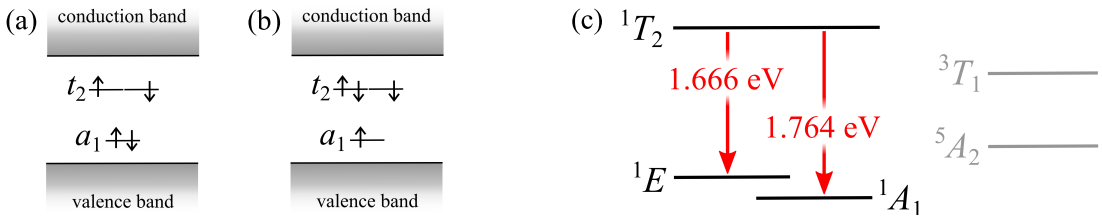

Figure 1-5: Electron occupation of (a) ground and (b) first excited molecule orbitals configuration of the V^0. The arrows indicate electrons with spin up and down respectively. (c) Energy level structure of the V^0 center. Optical transitions (red arrows) can be observed between the singlets $^1T_2$ and $^1A_1$ as well as between $^1T_2$ and ^1E. The optically inactive states are shaded in gray. Energetic ordering of the states according to [10].

one to the $^1A_1$ ground state at 1.666 eV. Note that the assignment of the two ZPLs to transitions into the corresponding ground states are based on their energetic ordering according to [10]. However, the circular polarization characteristics of the ZPLs suggest a different ordering, which will be presented in Sec. 3.1.5.

Chapter 2

Experimental methods

This chapter portrays a clear focus on the experimental details. Firstly, the basic experimental setup, which was used for polarization sensitive photoluminescence and photoluminescence excitation (PLE) experiments are illuminated and thoroughly discussed in Sec. 2.1. Subsequently, the confocal setup used for sample characterization is visualized in Sec. 2.2. In addition, the method of high frequency optically detected magnetic resonance is presented in Sec. 2.3. Finally, the diamond samples used in the experiments are characterized in Sec. 2.4. Particular focus is put on the influence of defect center concentration and sample geometry on the optical properties.

2.1 Polarization sensitive PL and PLE

All experimental techniques presented here aim to detect the emitted PL of the diamond samples. However, dependent on the specific task of measurement, the experimental requirements differ and hence, various setups were used. A confocal Raman spectrometer was used for sample characterization. Due to the sensitivity and high degree of automation of such a stand alone system, a big number of samples could be characterized in an appropriate time. Yet, for a precise measurement of PL polarization or for probing magnetic field dependences, a more flexible experimental setup had to be utilized. Especially when it comes to PLE experiments, the usage of tunable laser systems is inevitable.

A simplified scheme of such an PLE setup is depicted in Fig 2-1. For excitation three different continuous wave (CW) laser systems could be used. For high energetic excitation with an energy of 2.33 eV a frequency doubled, diode pumped neodymium-doped yttrium orthovanadate (Nd:YVO_4) laser (Ligthhouse Photonics, Sproud-G or Coherent, Verdi V-10) was used. The maximum output power of the lasers was 10 W. In addition, two tunable dye lasers were used for excitation with lower energy. Both lasers were pumped with a frequency doubled, diode pumped Nd:YVO_4 laser (Coherent, Verdi V-10) and were equipped with different dye liquids to cover a broad spectral range. The first dye laser (Tekhnoscan, Amethyst) was equipped with either Rhodamin-6G to

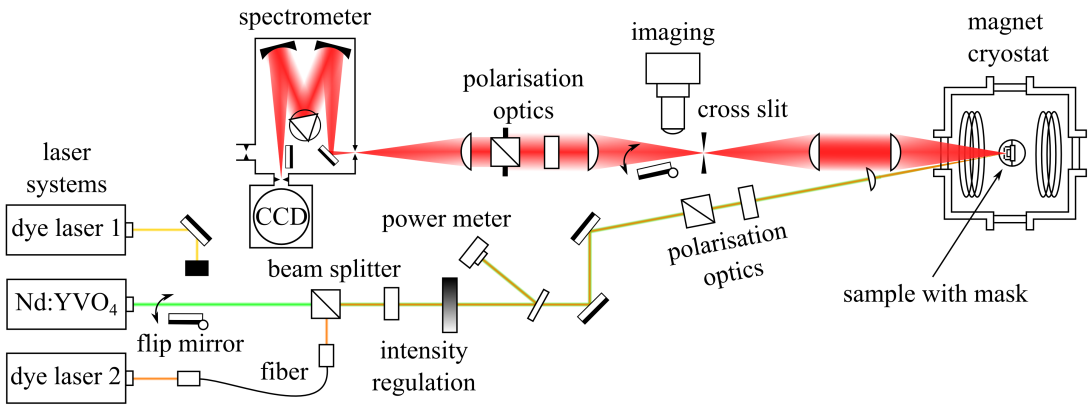

Figure 2-1: Experimental setup used for polarization sensitive PL spectroscopy and PLE measurements. Three different laser systems could be used to excite the sample which was mounted in a magnet cryostat. Here the simultaneous excitation with two lasers (green and orange) is shown. While the third laser beam (yellow) is blocked. The polarization of the exciting laser as well as the detected PL (red) could be controlled individually.

cover an energy range from 2.10 to 2.23 eV or with DCM for excitation with 1.96 to 2.02 eV. The linewidth was about 0.4 meV. When pumped with 7 W the maximum output power was about 250 mW with Rhodamin-6G and 200 mW with DCM. The second dye laser (Coherent, 899) was able to cover an energy range from 1.98 to 2.22 eV when equipped with Rhodamin-6G and a range from 1.92 to 2.08 eV when equipped with Rhodamin-B. The linewidth was about 0.1 meV. The maximum output power when pumped with 8 W was 930 mW for Rhodamin-6G and 710 mW for Rhodamin-B.

Via using the same excitation path for all three lasers, a quick change between the laser systems was possible, by using flip mirrors. At the same time, the readjustment after switching to another laser was minimized. Note that the second dye laser was coupled with an optical fiber. More precisely, it was a polarization preserving single mode fiber optimized for the wavelength of the emitted laser. By using specific fiber couplers, designed to fit the characteristics of the fiber, the power losses were reduced to less than 20 %. Moreover, for simultaneous excitation with two lasers, a beam splitter was used to overlap the beams of the Nd:YVO_4 and the second dye laser. In order to achieve optimal overlapping of the two beams, beam splitter and fiber coupler, were mounted on xyz-axis positioning stages.

To adjust the intensity of the excitation laser, a half-wave plate as well as a gradient filter were used. Whereas a gradient filter directly effects the laser power, a half-wave plate just rotates the polarization plane of the laser. However, the intensity regulation with the half-wave plate was achieved in combination with the Glan-Thompson prism of the polarization optics. The prism only transmitted a certain polarization, by rotating the polarization plane with the half-wave plate, the transmission ratio could be adjusted.

Unstable laser power was a great obstacle in reaching high accuracy of measurement.

Especially when measuring PL polarization characteristics, which were determined by differential spectra, power variations led to high uncertainties. As a countermeasure, a small percentage of the laser was reflected by a glass plate into a power meter. The laser power was detected during the whole measurement for subsequent normalization of the recorded spectra. Doing so, the systematical error due to unstable laser power was minimized, as long as the intensity of the PL showed a linear power dependence in the region of interest.

To control the polarization of the exciting laser, a Glan-Thompson prism was used to define the polarization plane. The prism was set to the vertical position, hence the exciting laser was vertical linearly polarized. For circularly polarized excitation a quarter wave plate, optimized for the laser wavelength, was installed after the Glan-Thompson prism.

The laser was focused on the sample with a lens. The spot of the exciting laser was varied between 60 and 210 μm. The sample itself was mounted in a variable temperature inset (VTI) of a split coil magnet cryostat (Cryogenic, 10 T). With the VTI the temperature T was varied between 1.8 and 300 K. The magnetic field B was aligned along the detection path (Faraday geometry) and was varied between 0 and $\pm$9 T. Note that due to the small angle of about 5° between excitation and detection path, the geometry of the magnetic field was not an exact, but a slightly tilted Faraday geometry. However, the angle was considered small enough to approximate the optical axis (z-axis) being identical for both, excitation and detection path.

The sample was strain free embedded in a black cardboard envelope, which was fixed with strews or glue (Pattex, contact adhesive Classic) on the sample holder mounted in the VTI. Moreover, the sample was covered with a plastic mask (PVC or Torlon) to define the region of excitation. This was of great importance, since inhomogeneities in the sample made the PL signal dependent on the excitation spot. Therefore, one had to ensure that the excitation spot on the sample was the same for all measurements.

The PL emitted by the sample was collected with an achromatic lens optimized for the wavelength of the defect centers' ZPL. Due to the dimensions of the cryostat, the distance between sample and lens was about 30 cm, hence just the small part of the PL which was emitted roughly along the optical axis was detected. Therefore, the PL yield was rather small. For sample characterization a much more sensitive system was used, see Sec. 2.2. To make sure that only light coming from the sample was detected, the PL was focused on a cross slit which cut off stray light. For measurements near the laser line an additional color filter (e.g. OG12) was inserted in the detection path.

Directly behind the cross slit a flip mirror was applied to couple a camera connected to a microscope objective into the optical path. The camera was used for imaging the sample and adjusting the spot of the exciting laser. This was necessary especially for excitation with two laser beams, to ensure optimal beam alignment. In addition to that, for angle resolved measurements, a specific sample holder was used which allows rotation of the sample around the optical axis. By using the imaging system, the angle of the sample could be adjusted with a precision of $\pm$1°.

For polarization sensitive detection of the PL, polarization optics, containing a half-wave plate for linear and a quarter wave plate for circular polarization as well as a

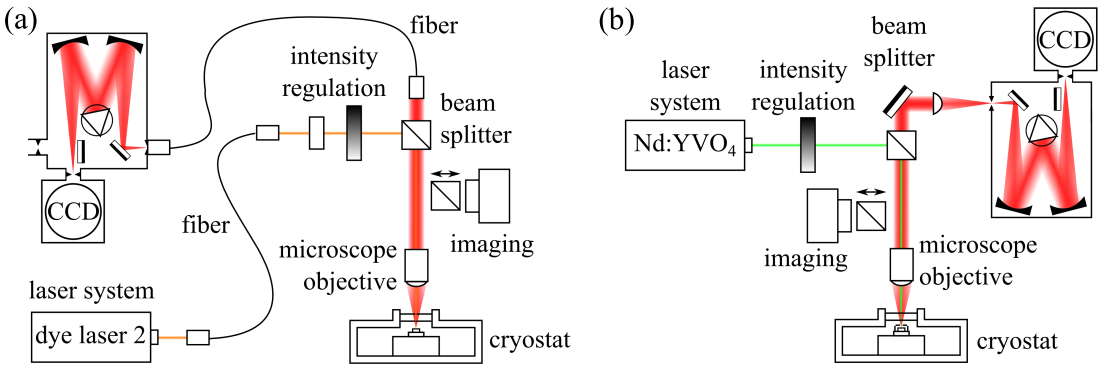

Figure 2-2: Confocal setups used for (a) PLE experiments with high excitation power densities and (b) sample characterization. A microscope objective was used to increase PL intensity. Three different laser systems could be used used to excite the sample.

Glan-Thompson prism were placed in the detection path. Note that the prism was set to the horizontal position, because the refraction grating symmetry of the spectrometer was optimized for horizontal linearly polarized light. Moreover, laser stray light was reduced by this setting, since the Glan-Thompson prism in the excitation path only transmitted vertical linearly polarized light. Another measure to reduce stray light was blocking light which hit the spectrometer from the side by covering the detection path with tubes or screens.

Another achromatic lens optimized for the wavelength of the defect centers ZPL focused the PL on the entrance slit of a spectrometer. The spectrometer (first stage of Acton, TriVista 555), used to spectrally split up the PL, had a focal length of 0.5 m and was used with a holographic grating having 1800 groves per mm. The spectra were recorded with a nitrogen cooled charge-coupled device (CCD) camera (Princeton Instruments).

2.2 Spatially resolved PL

The previously described setup had two disadvantages, which made it unsuitable for certain measurements. One disadvantage was the small PL yield, the other was the limited excitation power density which could be accomplished. In order to prevent damaging of the sample or the used equipment, laser excitation powers should not exceed 100 mW. With a minimal spot size of 60 μm, the maximal power density was about 3.5 kWcm^{-2}. However, for some experiments an excitation power density in the order of MWcm^{-2} was essential. Such high power density and a larger PL yield could be achieved with a few micrometer resolution.

The basic principle of such a confocal setup is shown in Fig 2-2 (a). The main difference to the previously discussed experimental setup was the use of a microscope objective, which reduces the excitation spot to about (2$\pm$1) μm, and a different cryostat

suitable for the microscope objective. For excitation the second dye laser system was used with a fiber. For intensity regulation a half-wave Fresnel-rhombus retarder and a variety of gray filters were used. The laser was aligned with the detection path via a polarizing beam splitter. A microscope objective with a magnification of 50 focused the laser on the sample, which was mounted in a flow cryostat (CryoVac, KONTI). In this cryostat the sample was directly glued on a cold finger using a silver based electrically conductive adhesive to reduce the strain on the sample. The distance between cryostat window and sample was just a few millimeters, therefore the microscope could be used closely to the sample. As a consequence, the PL yield was much higher compared to the previously described setup. The PL was collected with the microscope objective and coupled into a multi-mode fiber, which was connected to the spectrometer. it is characteristic for a confocal setup that the excitation and detection path lie on the same optical axis. Note that for imaging the sample a beam splitter, which was connected to a camera, was inserted in the detection path.

In order to characterize the samples a different setup was used. For sample characterization a high PL yield was useful to reduce the acquisition time per sample. Moreover, a higher PL yield made PL characterization at room temperature possible which could be performed with less effort compared to measurements at low temperatures. Therefore, sample characterization was executed at a confocal Raman spectrometer system (S&I, MonoVista CRS+). A simplified scheme of the system is illustrated in Fig 2-2 (b). A frequency doubled Nd:YVO_4 laser (Cobolt Samba^{TM} 100) was used for excitation. Intensity was adjusted with a variety of gray filters. The detection part of the confocal Raman system, including the spectrometer (Acton, SP-750), was mostly identical with the confocal setup described in the first part of this section.

2.3 High frequency optically detected magnetic resonance

In addition to optical excitation with a laser, low energetic excitation with high frequency microwaves (MWs) was used to optically detect magnetic resonances. In order to do so, the setup described in Sec. 2.1 had to be modified. While the setup was more or less the same regarding optical excitation and spectrally resolved PL detection, a special sample holder, which was inserted in the VTI of a split coil magnet cryostat (Oxford Spectromag, 7 T) was used for resonant MW application. The sample itself was mounted inside a MW cavity, which was optimized for a frequency of (60.000 ± 0.002) GHz. The resonance frequency was adjusted by slightly changing the diameter of the cavity with a micrometer tuning plunger. The MW were emitted by a MW generator system, coupled to the cavity via waveguides.

A scheme of the MW setup is shown in Fig. 2-3. The MW emitted by the generator (red solid arrow) were pulsed. Pulse duration as well as repetition frequency were preset by a master oscillator (frequency synthesizer). Typically 0.1 to 1 s pulses with a repetition frequency of 10 to 1 Hz were used. Note that the pulsing was achieved by internal damping of the MW output power of the generator about -40 dB. An attenuator,

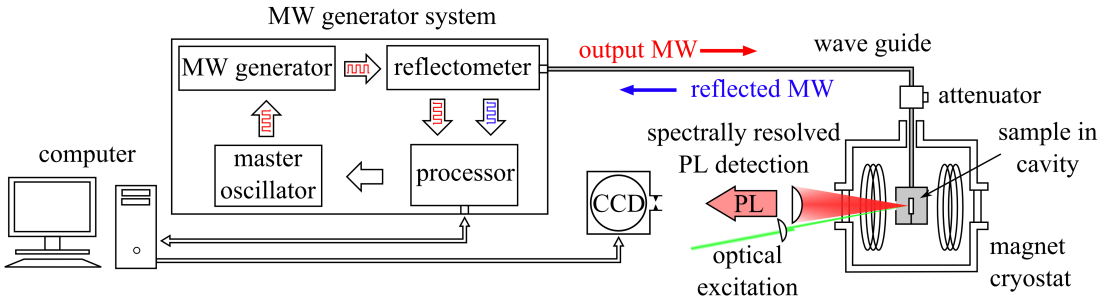

Figure 2-3: Setup with MW generator system for measuring optically detected magnetic resonances. Placing the sample in a cavity enables simultaneous excitation with laser light and 60 GHz MW radiation. With a reflectometer the output and the reflected MW radiation can be monitored to ensure optimal MW application inside the cavity.

coupled in the waveguide between generator system and cavity, was used to adjust the MW power between 8 nW and about 100 mW. A fraction of the MW radiation was reflected in the cavity (blue solid arrow) and monitored together with the MWs emitted by the generator by using a reflectometer. The processor, which was the interface to a computer with the controlling software, provided the control over the master oscillator as well as the readout of the reflectometer. By comparing the power of the output and reflected MW radiation, the quality factor of the cavity could be determined and optimized by sweeping the MW frequency or manually tuning the cavity.

The MW pulse sequence was synchronized with the readout of a CCD camera, coupled to a spectrometer. This allowed the alternating detection of spectra with and without additional MW excitation, as well as the direct measurements of differential spectra. The latter was essential for the detection of optically magnetic resonances, which is discussed in detail in Chapter 6. It is worthwhile mentioning that the magnetic field was varied in small steps of 0.1 mT. The magnet power supply of the Oxford Spectromag cryostat was capable of such precise variations as well as remote operation by the MW generator control software, whereas the magnet power supply of the Cryogenic cryostat was not. However, the Cryogenic magnet could be operated by the Oxford power supply too, but in this case the magnetic field calibration of the Oxford magnet power supply was not valid. When operating the Cryogenic cryostat magnet with the Oxford magnet power supply a current of 10.3929 AT^{-1} had to be applied.

2.4 Details on samples

The samples studied in this work were synthetic diamonds which contained different amounts of impurities. They can be subdivided in two groups, dependent on their crystal symmetry. Firstly, the samples grown along the (111) direction of the crystal are considered. Then a sample grown in (001) direction is discussed:

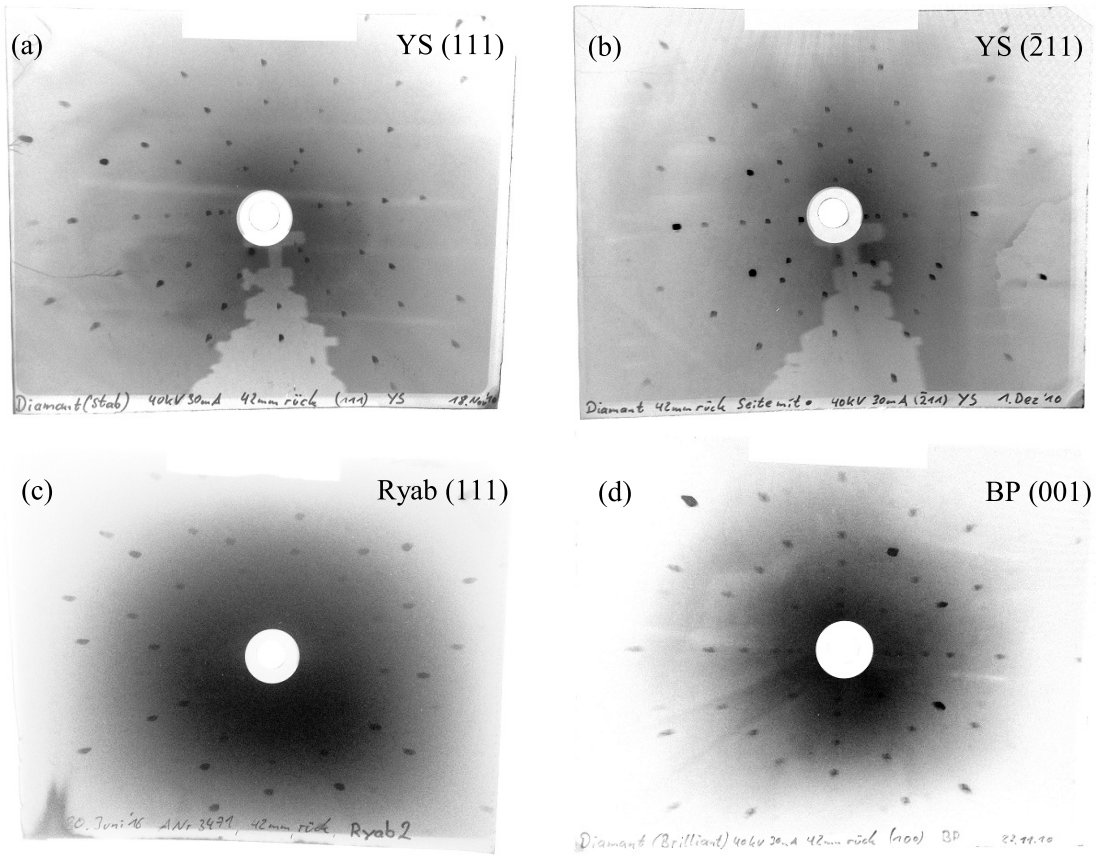

Figure 2-4: Laue diffraction images of (a,b) YS, (c) Ryab and, (d) BP, measured along the optically addressable directions, reveal the corresponding symmetry axes of the diamond crystals.

Four plane bulk type Ib diamond samples, "Ryabzev2" (Ryab), "NVReference" (NVRef), DC7 and D01 were studied. All of them were grown by the HPHT technique along the (111) direction in the Rzhanov Institute of Semiconductor Physics, SB RAS in Novosibirsk. In addition, another HPHT grown bulk diamond sample, which was formed like a rectangular prism was investigated. The latter had an NV center density of $\rho_{\mathrm{NV}} = 2.9$ ppm ($5.1{\cdot}10^{17}$ cm^{-3}). Due to the high amount of nitrogen impurities of about 30 ppm (type Ib diamond) this sample had a distinct yellow color and was internally labeled by "Yellow Submarine" (YS). This sample was produced by Sumitomo Electric Industries, Ltd., irradiated at 2 MeV with an electron fluence of 10^{17} cm^{-2} and subsequently annealed.[61] In contrast to the other samples, YS could be sufficiently excited along two directions, which were identified with the corresponding crystal symmetry axes by the Laue method.[62] In Fig. 2-4 (a) and (b) the transmission images for YS along the two optically addressable axes are shown. By analyzing the diffraction pattern of the crystal one can identify the symmetry axes to be (111) and (2̄11). Apparent in Fig. 2-

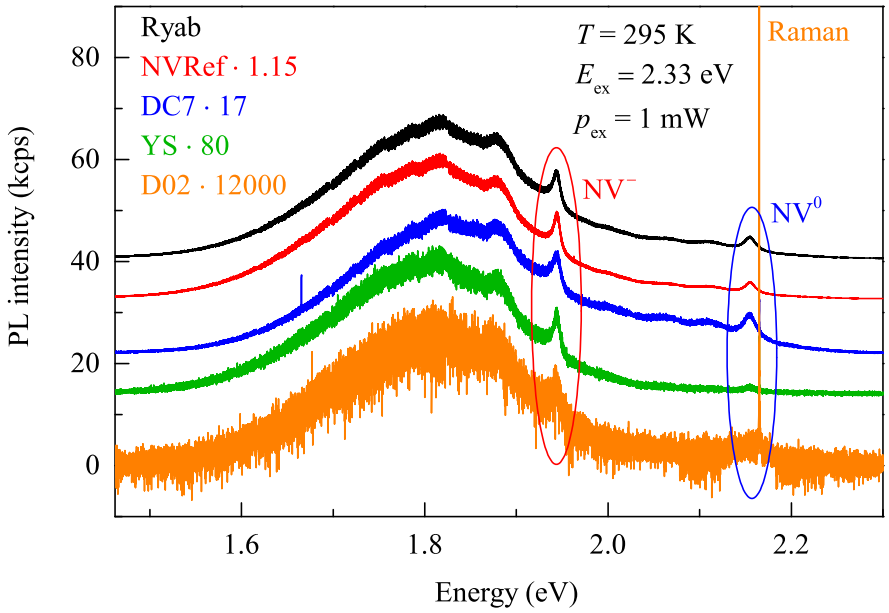

Figure 2-5: PL spectra of the (111) diamond samples. Note that for visibility, the spectra are shifted by an offset and scaled with a factor of 1.15 for NVRef (red), 17 for DC7 (blue), 80 for YS (green), and 12000 for D02 (orange). The ZPLs of the NV^- centers are circled in red, the ZPLs of the NV^0 centers in blue.

4 (c), the symmetry axes of Ryab is confirmed to be (111), as the diffraction pattern is quite similar to the one of YS in 111 direction.

The NV center concentration of Ryab was the highest among the studied samples. It was estimated to exhibit $\rho_{NV} = 3.8$ ppm ($6.7 \cdot 10^{17}$ cm^{-3}), giving the sample a deep red color. A similar coloring could be seen in NVRef, which had a concentration of $\rho_{NV} = 2.3$ ppm ($4.0 \cdot 10^{17}$ cm^{-3}). Both samples were irradiated with energies in the order of few MeV and subsequently annealed. The concentration of DC7 was claimed to be $\rho_{NV} = 25$ ppm ($44 \cdot 10^{17}$ cm^{-3}). However, the irradiation depth for this sample was not very great. Since the sample was irradiated with an energy of about 30 keV, one could expect the irradiation depth to be in nm-scale. Hence, the high concentration was only present near the surface of the sample. PL measurements showed that NV center ZPLs could only be observed when the front side of the sample was excited. Excitation of the back side led to no measurable NV center PL (data not shown). Therefore, the effective NV center concentration of the examined space laid somewhere between the concentration of NVRef and YS. The sample D01 had a rather small NV center concentration; the PL signal was barely measurable.

In Fig 2-5 the PL spectra of all samples grown along the (111) direction are shown. The PL measurements were performed on the confocal Raman spectrometer, compare Fig 2-2 (b). The spectra have more or less the same shape for all samples. The ZPL of

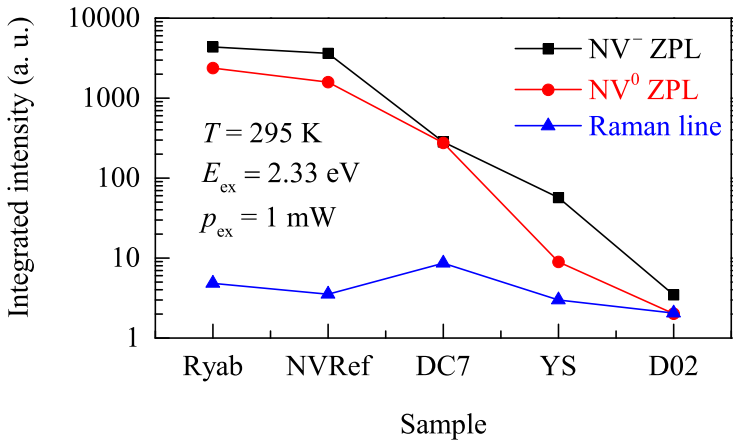

Figure 2-6: Spectrally integrated intensity of NV^- (black) and NV^0 ZPL (red), as well as Raman line (blue) of the (111) diamond samples. Intensity of ZPLs scales with NV center concentration, whereas the Raman intensity does not.

the NV^0 center is observed at about 2.156 eV (blue oval), whereas the NV^- ZPL can be seen at 1.946 eV (red oval). The latter is accompanied by a broad phonon side band (PSB). Moreover, the 1332 cm^{-1} Raman line of the diamond lattice[63, 64] is detected at 2.165 eV as well. Note that the spectra are scaled for the sake of comparison. It is obvious that the PL intensity drastically decreases for samples with low NV center concentration.

In order to compare the PL spectra of the different samples, the spectrally integrated intensities of both ZPLs and the Raman line are illustrated in Fig 2-6. The NV^0 and NV^- ZPL intensities for Ryab and NVRef are roughly the same, but for samples with lower NV center concentration the intensity decreases. Noteworthy is that the NV^- ZPL intensity is almost always larger than the NV^0 ZPL intensity. The only exception is the sample DC7; here both intensities are more or less equal. The main difference between DC7 and the other samples is that it was irradiated with an energy of about 30 keV. In contrast to the ZPLs of the NV centers, the Raman line intensity does not depend on the NV center concentration.

Further measurements will focus on the samples Ryab as an example of high NV center concentration and YS as an example of medium concentration. The other samples will not be further investigated. NVRef is almost identical to Ryab, therefore one can not expect to gain relevant information by additionally studying this sample. DC7 is not suitable for investigation due to its inhomogeneous NV center distribution. The low PL signal of D02 makes this sample unsuitable for further measurements.

As an example of a sample with low NV center concentration a bulk rose cut diamond with $\rho_{NV} = 0.14$ ppm ($0.25 \cdot 10^{17}$ cm^{-3}) was used. It was grown with the CVD method by Apollo Diamond Inc. in Boston.[61] This sample showed no noticeable coloring, the nitrogen concentration was about 0.05 ppm (type IIa diamond). However, it contained

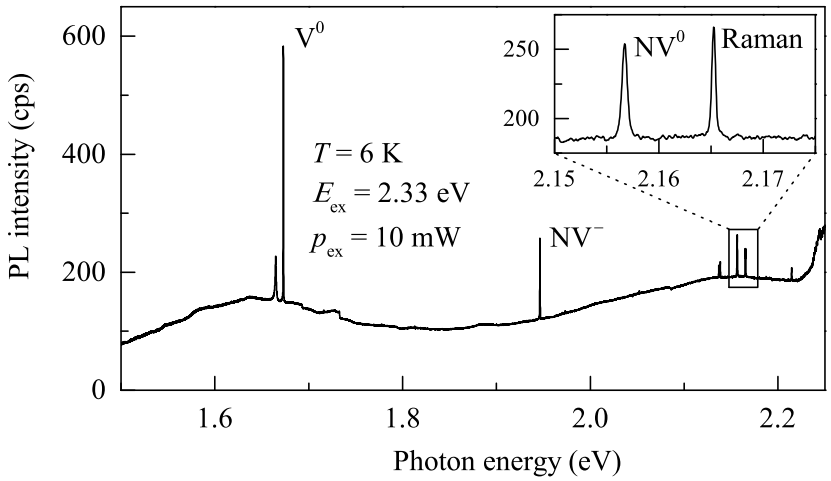

Figure 2-7: PL spectrum of BP with optical axis along the (001) direction. The sample contains NV and V^0 centers. The insert shows the PL spectrum around 2.16 eV in detail.

a macroscopic black inclusion, which had the form of a pyramid; hence, the sample was internally labeled "Black Pyramid" (BP). Because of the sample shape, optical excitation was only possible along one direction, which was identified through the Laue method to be the (001) axis, compare Fig. 2-4 (d). A detailed discussion of sample geometries and the orientation of NV centers can be seen in 4.2.

Due to the relative low concentration of NV centers in BP, the emitted PL is rather small, approximately 30 times smaller than that of YS. Hence, sample characterization at room temperature is not sufficient, compare D02 spectra shown in Fig 2-5 (green line). In Fig 2-7 the PL spectra of BP, measured at the PL setup is depicted. At low temperatures the intensity of the broad PSB of the NV^- center is negligibly small compared to the strong ZPLs signals of the impurities. One can easily assign the observed lines to the respective defect centers. At an energy of 1.674 eV the main ZPL of the V^0 center can bee seen, whereas the less intense ZPL is observed at 1.666 eV. The NV^- ZPL lies at 1.945 eV and the NV^0 emits an ZPL at 2.156 eV. Moreover the Stokes-Raman line can be identified at 2.165 eV, which is about 1.332 cm^{-1} away from the exciting laser at 2.33 eV.

Chapter 3

Circular polarization properties of defect center PL

This chapter provides insight into the circular polarization characteristics of the NV^-, NV^0, and V^0 ZPL as well as of the NV^- SST. Firstly, the optical selection rules for the NV^- ZPLs are discussed in Sec. 3.1.1. Special focus is drawn to the energy splitting of the lines in the presence of an external magnetic field due to the Zeeman effect. Secondly, by measuring the Zeeman splitting, effective orbital g-factors are estimated and the orderings of the defect center energy levels are determined for the NV^- triplet (Sec. 3.1.2) and singlet states (Sec. 3.1.3), as well as for the NV^0 (Sec. 3.1.4) and V^0 centers (Sec. 3.1.5). A detailed analysis of the circular polarization degree in the presence of an external magnetic field is presented in Sec. 3.2. Additionally, the influence of temperature and the orientation of the crystal with respect to the polarization of the exciting laser is thoroughly discussed. Concluding remarks can be found in Sec. 3.3. The results presented in this chapter were obtained with the experimental setup presented in Sec. 2.1. The samples BP excited along the (001) direction and YS excited along the (111) direction were used. Note that the content covered in this chapter has been published in [65].

3.1 Zeeman effect in the defect center PL

In the following, the circular polarization properties of the PL emitted by the defect centers will be discussed, starting with a detailed consideration of the NV^- level structure and the ZPL emission process with particular focus on the influence of an external magnetic field. In this context, primarily the circular-polarized states, which are affected by the Zeeman effect, will be considered. An analysis of the linear polarization characteristics in the presence of high magnetic fields is presented in Sec. 4.4.

	A_1	A_2	E_x	E_y	E_1	E_2
${}^3A_{2+}$	σ^-	σ^-			σ^+	σ^+
${}^3A_{20}$			π	π		
${}^3A_{2-}$	σ^+	σ^+			σ^-	σ^-

Table 3-1: ZPL polarization dependent on the states involved in the emission process; $\sigma^{+(-)}$ indicates right (left) circular polarization, whereas π stands for linear polarization.[68].

3.1.1 Optical properties of the NV^- center

In order to learn about the circular and linear polarization of defect center ZPLs, the NV^- is considered first. An analysis of the ZPLs of the other defect centers will follow. As already discussed in Sec. 1.3, the NV^- ZPL is associated with the optical transition between excited triplet ${}^3E$ and the triplet ground state ${}^3A_2$. The emission process is governed by the selection rules which arise from the dipole approximation. According to these, an optical transition is only allowed between states with a total angular momentum difference of 0 or ± 1. The emission process of the ZPL in general is spin conserving, but spin flip processes can be observed.[66] However, the latter processes can be neglected, since the transition rates are less than 1 % of the spin conserving transition rates.[67] In contrast to the total spin, the orbital angular momentum is not conserved during the emission process of the ZPL. As a result of angular momentum conservation, the absorbed or emitted photon must carry the missing angular momentum.

The angular momentum of a photon is defined by its polarization. In this context, right (σ^+) or left circular (σ^-) polarization indicates an angular momentum of ± 1 respectively, while linear (π) polarization describes a superposition of σ^+ and σ^- polarization with an angular momentum expectation value of 0. For instance, from the excited states E_x and E_y with spin projection $m_S = 0$ only transitions to the $m_S = 0$ ground state ${}^3A_{20}$ are spin conserving. Here, the transition goes from an $|E_\pm\rangle\,|0\rangle$ to the $|E_0\rangle\,|0\rangle$ spin orbit state, compare Eq. (1.7), (1.12), and (1.13). The emitted ZPL is linearly polarized; hence, the orbital angular momentum projection m_L, displayed by the index of the orbital function $|E_{\pm,0}\rangle$, does not change. Spin conserving transitions from the other excited states $A_{1,2}$ and $E_{1,2}$ to the corresponding ground states ${}^3A_{2\pm}$ include a change of the total orbital angular momentum projection by ± 1. Therefore, the ZPL is σ^+ or σ^- polarized. The individual polarization for each dipole-allowed transition can be seen in Tab. 3-1.

The specific states inside the triplet states ${}^3A_2$ and ${}^3E$ are energetically separated by only a small zero field splitting in the order of 10 μeV,[68] compare Fig. 1-3. In addition, intrinsic or externally applied strain as well as spin-spin and spin-orbit interaction can induce an energy splitting too.[69, 17] However, in order to reach a large energy splitting, which makes the individual states distinguishable by optical spectroscopy, high magnetic

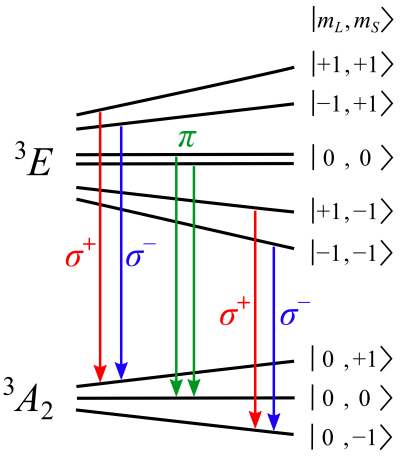

Figure 3-1: Level structure scheme of NV^- triplet states at high magnetic fields, $B \gg 0$. The optical ZPL transitions are indicated with arrows. Solid red and blue arrows indicate right and left circularly polarized transitions respectively, whereas green arrows stand for linear polarized transitions. Note that only optically active states are displayed. The states are described by their orbital angular momentum projection m_L and spin projection m_S.

fields have to be applied to the diamond crystal. The splitting in a magnetic field $\mathbf{B}$ is in accordance with the spin and orbital components of the Zeeman Hamiltonian

$$H_Z = \mu_B g_S \mathbf{B} \cdot \mathbf{S} + \mu_B g_L \mathbf{B} \cdot \mathbf{L} + \mathcal{O}(\mathbf{B}^2). \tag{3.1}$$

Here, g_S and g_L indicate the spin and orbital g-factor respectively; μ_B is the Bohr magneton; $\mathbf{S}$ and $\mathbf{L}$ are the spin and orbital angular momentum quantum number. Terms of quadratic magnetic field dependence are denoted by $\mathcal{O}(\mathbf{B}^2)$.

The Zeeman effect is caused by an interaction of a macroscopic external magnetic field and a microscopic magnetic moment, which is created by a moving electric charge. This microscopic movement can stem from the spin or orbital angular momentum of the charge carrier. In case of the NV center, the magnetic moment is created by both the spin $\mathbf{S}$ and the orbital angular momentum $\mathbf{L}$ of the orbital states.

It is accepted at large that the spin g-factor has a value of about $g_S = 2.0$, which is the value of a free electron.[70] The orbital g-factor, however, is significantly smaller: $g_L \approx 0.1$.[71] Therefore, the Zeeman splitting due to the spin contribution is much larger than the splitting due to the orbital contribution. In Fig. 3-1 the energy splitting due to the Zeeman effect of the ground and first excited state of the NV^- center is shown. For instance, the ground states $^3A_{2\pm}$ with spin momentum projection $m_S = \pm 1$, which have the same energy without application of a magnetic field, are shifted apart in the presence of an external magnetic field. The state $^3A_{2+}$ with $m_S = +1$ is shifted to higher energies, whereas the $m_S = -1$ state $^3A_{2-}$ is shifted to lower energies. The excited states additionally exhibit a splitting due to their non-zero orbital angular momentum projection m_L.

Since the ZPL is, however, a spin conserving transition, the contribution of the spin momentum projection to the Zeeman splitting cannot be seen in an energy shift of the ZPL. This is because both involved states, the excited and the ground state, are equally shifted in energy, since one can expect the spin g-factor for the ground state g_S^{gs} to be equal to the excited state g-factor g_S^{es}. The PL spectra of the NV^- center in BP at an external magnetic field of $B = 10$ T for different polarization configurations

($\sigma^{\pm}$, $\sigma^{\pm}$) are depicted in Fig. 3-2 (a). Here, the first entry indicates the polarization of the exciting laser and the second visualizes the polarization of the detected PL. For comparison, a spectrum at zero magnetic field (gray dashed line) is depicted as well. One can clearly see that the NV$^-$ ZPL at about 1.948 eV exhibits an energy shift in the presence of a high magnetic field. The σ^+ polarized ZPL (red and blue lines) is shifted to higher energies, whereas the σ^- polarized ZPL (black and green lines) is shifted to lower energies.

3.1.2 Zeeman splitting of the NV$^-$ ZPL

The Zeeman splitting ΔE_{Z} can be determined as the difference between the peak energy $E_{\mathrm{ZPL}}^{\sigma^{\pm}}$ of the σ^+ and σ^- polarized ZPL, estimated via Gaussian fits: $\Delta E_{\mathrm{Z}} = E_{\mathrm{ZPL}}^{\sigma^+} - E_{\mathrm{ZPL}}^{\sigma^-}$. In Fig. 3-3 (a) the Zeeman splitting of the NV$^-$ ZPL in BP is illustrated dependent on the magnetic field for excitation with σ^+ (red circles) and σ^- (blue squares) polarized light. One can clearly see that ΔE_{Z} evolves linearly with the magnetic field and is inverse symmetric around $B = 0$ T; the zero field splitting is negligibly small. For both excitation polarizations the energy difference amounts to $\Delta E_{\mathrm{Z}} = (-84 \pm 2)$ μeV at $B = -9$ T and $\Delta E_{\mathrm{Z}} = (87 \pm 2)$ μeV at 9 T. Therefore, one can conclude that the opposite circularly polarized NV$^-$ ZPLs are split in an external magnetic field by about 9.5 μeV/T.

As mentioned before, only the orbital contribution to the Zeeman effect can be seen in the energy shift of the ZPL, since the spin projection is conserved during the emission process of the ZPL. Hence, the Zeeman splitting evaluated from the experimental data is given by

$$\Delta E_{\mathrm{Z}} = \mu_{\mathrm{B}} g_L B + \delta_0. \tag{3.2}$$

Here, B is the magnetic field strength and δ_0 the zero field splitting. It is assumed that the spin splitting for the ground and excited states is equal ($g_S^{\mathrm{gs}} = g_S^{\mathrm{es}}$) and that nonlinear Zeeman Hamiltonian terms are independent of the ZPL polarization. A linear fit according to Eg. (3.2) gives an effective orbital g-factor of $g_L = 0.164 \pm 0.002$ and a zero field splitting of $\delta_0 = (2 \pm 1)$ μeV for the NV$^-$ ZPLs in BP.

The NV$^-$ ZPLs in YS show similar Zeeman splitting, like it is illustrated in Fig. 3-3 (b). Again the differences between σ^- and σ^+ polarized excitation are negligible. Here, the energy shift ranges from $\Delta E_{\mathrm{Z}} = (-68 \pm 4)$ μeV at -9 T to $\Delta E_{\mathrm{Z}} = (110 \pm 2)$ μeV at 9 T. According to Eq. (3.2), one can calculate an effective orbital g-factor $g_L = 0.167 \pm 0.005$, which is well in line with the g-factor measured in BP. The zero field splitting of $\delta_0 = (21 \pm 1)$ μeV is, however, remarkably larger. This is most likely due to the strain in the sample, which is supposed to be larger compared to BP, because of the NV center concentration in YS being one order of magnitude higher.[69, 17] Note that the observed effective orbital g-factor for the NV$^-$ center is significantly larger than the g-factor of 0.10 ± 0.01 determined via spectral hole burning[53, 71] and ODMR[72] from samples with comparable low NV center concentrations. The Jahn-Teller-coupling (compare Sec. 4.3) is much stronger in these samples compared to the ones investigated in this thesis. Hence, there is a stronger reduction of the orbital angular momentum, resulting in smaller effective orbital g-factors. In contrast to that, an orbital g-factor

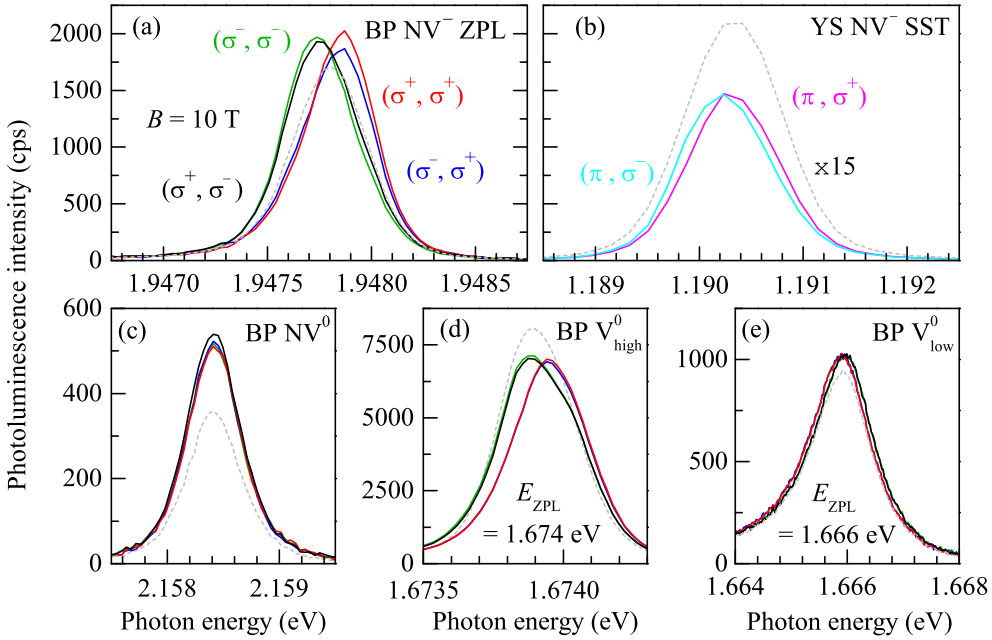

Figure 3-2: PL spectra at $B = 10$ T for different circular polarization configurations (solid lines) and at $B = 0$ T (gray dashed lines) of (a) NV^- ZPL in BP, (b) NV^- singlet states transition in YS, (c) NV^0 ZPL, and (d, e) V^0 ZPLs in BP; $T = 6$ K, $E_{ex} = 2.33$ eV. The polarization configuration is indicated by ($\sigma^{\pm}$, $\sigma^{\pm}$) or (π, $\sigma^{\pm}$); the first entry stands for the polarization of the exciting laser, the second describes the polarization of the detected PL.

of 0.22, which is even higher than the g-factors observed in BP and YS, was found in a sample with higher NV center concentration subjected to magnetic field strengths of up to 150 T.[73]

Before taking a look at the Zeeman splitting of the NV^- SST, as well as of the NV^0 and V^0 ZPLs in order to gain information about the level structure of these defect centers, the NV^- ZPLs observed in BP and YS will be investigated more closely. In Fig. 3-4 (a) the energy ΔE_{ZPL} of the NV^- ZPL in BP is depicted dependent on the magnetic field for different polarization configurations ($\sigma^{\pm}$, $\sigma^{\pm}$). Again, the first entry denotes the polarization of the exciting laser and the second entry gives the polarization of the detected PL. Note that $\Delta E_{ZPL}(B)$ is shown as the deviation of the ZPL energy E_{ZPL} from the arithmetic mean $\bar{E}_{ZPL}(0)$ of the ZPL energies measured in all four polarization configurations at $B = 0$ T: $\Delta E_{ZPL}(B) = E_{ZPL}(B) - \bar{E}_{ZPL}(0)$. As one can see, the ZPL energies exhibit quadratic magnetic field dependences in BP. Therefore, quadratic fit functions (solid lines) describe the data quite well. However, this is not reflected in the Zeeman splitting, compare Fig. 3-3 (a). Hence, one can conclude that the quadratic contribution $\mathcal{O}(\mathbf{B}^2)$ to the Zeeman Hamiltonian, compare Eq. (3.1), is equal for the ground and excited states.

However, when looking at the NV^- ZPL of YS no quadratic dependence on the

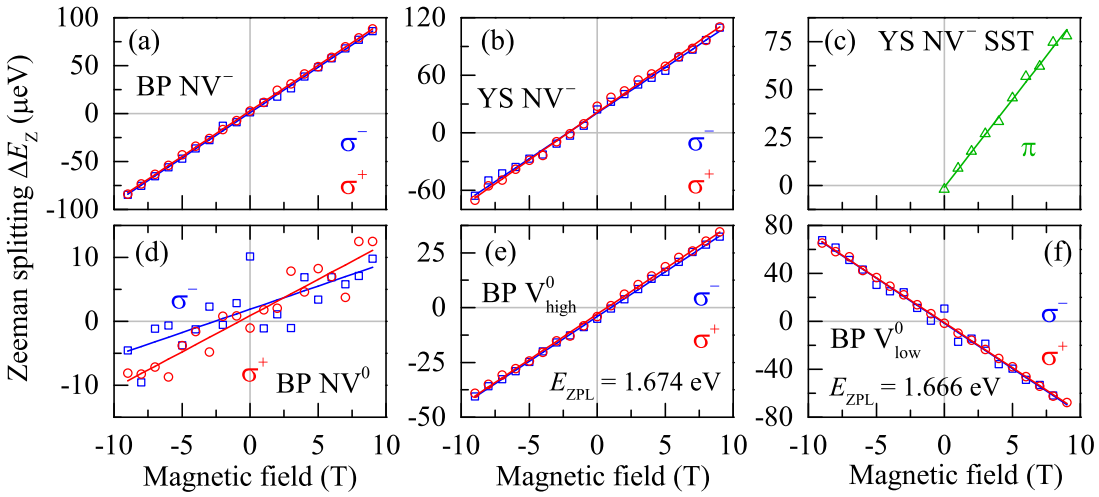

Figure 3-3: Zeeman shift of the investigated lines dependent on the external magnetic field under σ^- (blue squares), σ^+ (red circles), or π (green triangles) polarized excitation. NV^- ZPL in (a) BP in the (001) direction and (b) YS in the (111) direction. (c) NV^- singlet states transition in YS in the (111) direction, (d) NV^0 ZPL as well as the V^0 center ZPL at (e) 1.674 eV and (f) 1.666 eV in BP excited along the (001) axis. The straight lines are fits according to Eq. (3.2). $T = 6$ K, $E_{ex} = 2.33$ eV. The experimental error does not exceed the symbol size.

magnetic field can be observed. As on can see in Fig. 3-4 (b), the evolutions of $\Delta E_{ZPL}(B)$ can be fitted well by linear functions (dashed lines). Therefore, one can conclude that the nonlinear evolution of the ZPL energies in BP results from the mixing of states, which is, however, not present in YS. In contrast to BP, the NV center and nitrogen impurity concentration in YS is much higher, as is the strain, resulting in a higher zero field splitting. As a consequence, the zero field splitting lifts the degeneracy of the energy levels in YS, hence state mixing is reduced. Note that the zero field splitting of ground and excited state is not only influenced by strain but also by spin-spin as well as spin-orbit interaction. Furthermore, it is worthwhile noticing that BP was excited along the (001) axis of the diamond crystal, while YS was excited along the (111) direction. However, the observation is rather related to the NV center concentration and growth technique than to the measurement geometry. A more detailed analysis of ground state mixing in the NV^- centers at low magnetic fields is provided in Chapter 7.

Moreover, one can see a significant deviation of NV^- ZPL energies $E_{\sigma\pm}$ measured with σ^+ and σ^- polarized excitation. In Fig. 3-4 (c) the deviation $\Delta E_\sigma = E_{\sigma^+} - E_{\sigma^-}$ is depicted for BP and YS for both PL polarizations. Note that ΔE_σ of the σ^+ polarized NV^- ZPL in YS (black squares) is also indicated in Fig. 3-4 (b) at $B = 9$ T as a demonstrative example. For BP ΔE_σ is negligibly small at $B = 0$ T in both polarizations, whereas a zero field splitting of about 14 μeV for σ^+ and 8 μeV for σ^- NV^- ZPL polarization can be seen for YS. With rising magnetic field, ΔE_σ increases for both samples, independent of the ZPL polarization. The evolutions of ΔE_σ with

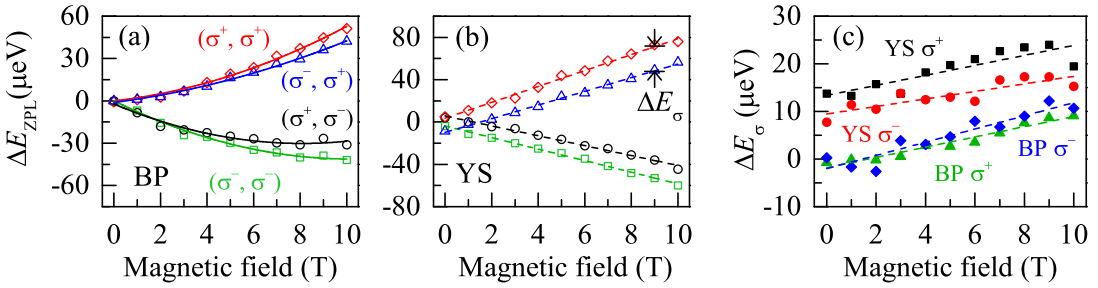

Figure 3-4: ZPL energy ΔE_{ZPL} of the NV$^-$ center in (a) BP and (b) YS normalized to the arithmetic mean at $B = 0$ T for different polarization configurations (open symbols). (c) ZPL energy difference ΔE_σ between excitation with σ^+ and σ^- polarized light. The straight lines are cubic, the dashed lines linear fits. $T = 6$ K, $E_{\mathrm{ex}} = 2.33$ eV. The experimental error does not exceed the symbol size.

the magnetic field can be fitted best with a linear function (dashed lines). Within the experimental accuracy the slope can be determined to be (1.1 ± 0.2) μeVT^{-1} for both samples and polarizations. The deviation ΔE_σ can be attributed to a difference in the spin splittings of the ground and excited states. In order to describe the experimental data, one has to assume that the spin splitting of the excited states is larger than that of the ground states. In terms of the g-factor, this implies that $g_S^{\mathrm{es}} = g_S^{\mathrm{gs}} + 0.019 \pm 0.004$. Additionally, one can assume that the excited states with positive (negative) m_S are predominantly excited by σ^+ (σ^-) polarized light.

3.1.3 Zeeman splitting of the NV$^-$ singlet state transition

The NV$^-$ ZPL, which is thoroughly analyzed in the previous section, is the transition between the triplet states of the NV$^-$ center. Next, the transition between the ^1E and $^1A_1$ singlet states will be discussed. In Fig. 3-2 (b) the σ^+ (magenta) and σ^- (cyan) polarized SST of the NV$^-$ center in YS is shown at $B = 10$ T for excitation with a π polarized laser. For comparison, a spectrum at $B = 0$ T (gray) is also shown. Note that the intensity of the SST is scaled with a factor of 15. However, the small intensity compared to the NV$^-$ ZPL is mainly due to the low quantum efficiency of the InGaAs-CCD camera compared to the Si-CCD camera used for the measurements in the visible range. Similar to the NV$^-$ ZPL, the σ^+ polarized SST is shifted to higher energies and the σ^- polarized SST is shifted to lower energies. Since the SST of the NV$^-$ center is a spin conserving transition too,[50] the SST Zeeman splitting, depicted in Fig. 3-3 (c), appears comparable to the Zeeman splitting of the NV$^-$ ZPL in BP, compare Fig. 3-3 (a). A fit according to Eq. (3.2) gives an effective orbital g-factor of $g_L = 0.157 \pm 0.004$, which is in good agreement with the g-factor observed for the NV$^-$ center in BP and a negligible $\delta_0 = (-1 \pm 1)$ μeV. Taking the results obtained from the Zeeman spitting of the NV$^-$ ZPL in YS into account as well, one can conclude that the effective orbital g-factor of the NV$^-$ center is about $g_{\mathrm{L}} = 0.16 \pm 0.01$. Since the electronic states of the NV$^-$ triplets and singlets arise from the same molecule orbitals,

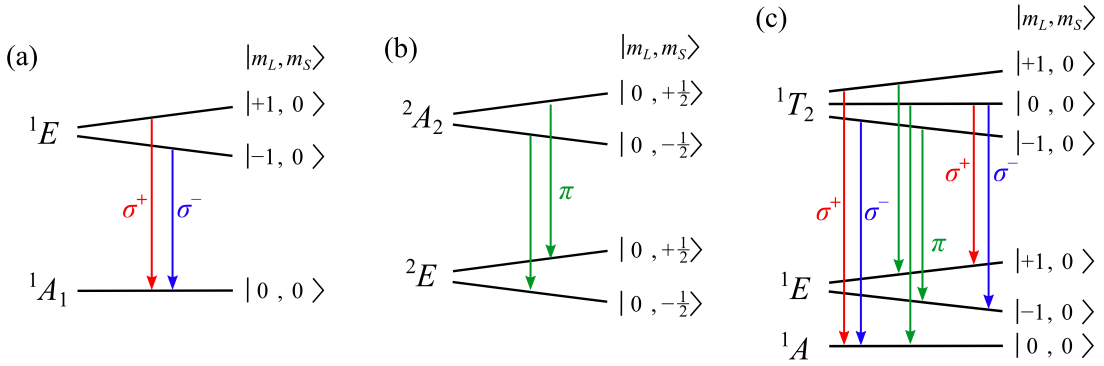

Figure 3-5: Level structure scheme of (a) NV^- singlet states, (b) NV^0 doublet states, and (c) V^0 states at high magnetic fields ($B \gg 0$). The optical ZPL transitions are indicated with arrows. Solid red and blue arrows indicate right (σ^+) and left (σ^-) circularly polarized transitions respectively, while green arrows stand for linear (π) polarized transitions. Note that only optically active states are displayed. The states are simplistically described by their orbital angular momentum projection m_L and spin projection m_S.

the orbital contribution to the Zeeman splitting is equal for the corresponding states.

Moreover, the energetic ordering of the singlet states can be determined by the Zeeman splitting. It is evident that the energy of the σ^+ polarized transition is higher than the energy of the σ^- polarized transition. Therefore, the ^1E state must be higher in energy than the $^1A_1$ state, as is illustrated in Fig. 3-5 (a). An inverted energetic ordering, as it has been proposed by Delaney et al.,[55] would lead to an inverted Zeeman splitting, resulting in a shift of the σ^+ (σ^-) polarized SST to lower (higher) energies, which is, however, not the case.

3.1.4 Zeeman splitting of the NV^0 ZPL

In addition to the negatively charged NV^- centers, the neutral NV^0 centers will be considered now. The spectra of the NV^0 ZPL in BP at 2.158 eV are illustrated in Fig. 3-2 (c) for different polarization configurations at $B = 10$ T. In contrast to the NV^- ZPL, there are no significant differences observable between the PL measured in σ^+ and σ^- polarization. The intensity of the NV^0 ZPL is about four times smaller compared to the NV^- ZPL. This is most likely due to the NV^- being the preferred charge state of the defect center under the given excitation conditions, compare Sec. 5.1.1. The Zeeman splitting of the NV^0 ZPL, shown in Fig. 3-3 (d), is about one order of magnitude smaller than that of the NV^- ZPL. An increase in ΔE_Z from about -10 μeV at -9 T to 10 μeV at 9 T is observed for σ^+ polarized excitation. Hence, the effective orbital g-factor can be determined to $g_L = 0.020 \pm 0.002$ according to Eq. (3.2). However, for σ^- excitation the shift is significantly smaller: $g_L = 0.012 \pm 0.002$.

In contrast to the NV^-, the NV^0 center consists of only five electrons. Due to the odd number of electrons, the ground state ^2E as well as the first excited state $^2A_2$ are spin doublets with $m_S = \pm\frac{1}{2}$,[56, 57] for details see Sec. 1.4. As depicted in Fig. 3-

5 (b), the excited state $^2A_2$ is split into the states $|0, +\frac{1}{2}\rangle$ and $|0, -\frac{1}{2}\rangle$. Note that the first entry indicates the orbital angular momentum projection m_L and the second entry stands for the spin projection m_S. For the ground state with ^2E symmetry one would expect a splitting into the four states $|\pm 1, +\frac{1}{2}\rangle$ and $|\pm, -\frac{1}{2}\rangle$. Accordingly, one should observe the σ^+ and σ^- polarized ZPLs being separated in energy by the orbital Zeeman splitting. In contrast to the NV^- center, for which the orbital contribution to the Zeeman effect leads to a splitting of the excited states only, since all ground states have $m_L = 0$, the orbital Zeeman splitting of the NV^0 ground state would lead to an inverted Zeeman splitting of the NV^0 ZPL. In such a case, the σ^+ polarized ZPL would be shifted to lower energies when a positive magnetic field is applied, whereas the σ^- polarized ZPL would be shifted to higher energies. This is, however, not the case. In fact, the observed Zeeman splitting is positive and one order of magnitude smaller than the orbital Zeeman splitting of the NV^- ZPL. Therefore, it can be concluded that the ground state ^2E splits into the two states $|0, +\frac{1}{2}\rangle$ and $|0, -\frac{1}{2}\rangle$, as shown in Fig. 3-5 (b). In such a scenario, the emitted ZPL is not associated with a change of the orbital angular momentum projection and is therefore always linearly polarized. Hence, the NV^0 ZPL exhibits no Zeeman splitting at the presence of an external magnetic field. The observed Zeeman splitting might be due to a difference in the spin splitting of the ground and excited states, since the value is quite comparable with the deviation ΔE_σ in the NV^- ZPL energy, which is caused by unequal spin g-factors.

3.1.5 Zeeman splitting of the V^0 ZPL

Besides the NV centers, also the V^0 centers are investigated. Fig. 3-2 (d) and (e) show the ZPLs of the V^0 centers in BP for different circular polarization configurations at $B = 10$ T. The more intense ZPL can be seen at 1.674 eV, whereas the less intense ZPL is observed at 1.666 eV. Comparably to the NV^- centers, an energy shift of the ZPL at 1.674 eV to higher energies in σ^+ polarization and to lower energies in σ^- polarization can be observed at 10 T. Remarkably, the ZPL at 1.666 eV shows an opposite behavior. Here, the σ^+ polarized line is shifted to lower energies, while the σ^- polarized line is shifted to higher energies.

The Zeeman shift of the V^0 ZPL at 1.674 eV (also denoted as V^0_{high}) is pictured in Fig. 3-3 (e) dependent on the magnetic field. Similar to the NV^- center, a linear Zeeman effect, which shows no big difference between σ^- and σ^+ polarized excitation, is observed. The energy shift varies between $\Delta E_{\text{Z}} = (-40 \pm 1)$ μeV at -9 T and $\Delta E_{\text{Z}} = (33 \pm 2)$ μeV at 9 T. According to Eq. (3.2), the effective orbital g-factor can be determined to $g_L = 0.071 \pm 0.001$. Note that the zero field splitting of $\delta_0 = (3.6 \pm 0.7)$ μeV leads to a slightly asymmetric Zeeman splitting around $B = 0$ T.

In Fig 3-3 (f) ΔE_{Z} is shown for the less intense V^0 ZPL at 1.666 eV (also denoted as V^0_{low}) as a function of the magnetic field. A fit according to Eq.(3.2) gives an effective orbital g-factor of $g_{\text{L}} = -0.128 \pm 0.001$. This is remarkable, because the g-factor has, on the one hand, a negative sign and, on the other hand, is about twice the value of the effective orbital g-factor one obtains from the more intense V^0 ZPL at 1.674 eV. Note that the zero field splitting $\delta_0 = (-1 \pm 1)$ μeV is negligibly small.

In order to explain the observed Zeeman splittings, the level structure presented in Sec. 1.4 has to be revisited, compare also Fig. 1-5 (c). In Fig. 3-5 (c) the energy level structure of the V^0 center is depicted, the ZPL transitions are indicated by red and blue arrows for σ^+ and σ^- polarization, respectively. The high energetic ZPL is associated with the transition to the ground state which is lower in energy. Since this ZPL exhibits a positive ΔE_Z for positive magnetic fields, which means the energy of the σ^+ polarized ZPL is higher than of the σ^- polarized ZPL, it must be a transition to the ^1A ground state. As one can see in Fig. 3-5 (c), a transition from the $^1T_2$ excited state to the ^1E ground state would result in a ZPL which is higher in energy in σ^- than in σ^+ polarization (blue arrow is longer than red arrow). Hence, the ZPL would show a negative Zeeman splitting for positive magnetic fields, as is observed for the low energetic V^0 ZPL at 1.666 eV. Therefore, one can conclude that the ^1E state is the ground state with higher energy.

Although, the values of the g-factors obtained for the V^0 centers are comparable to the orbital g-factor determined for the NV^- centers, they are significantly different. Since the orbital g-factor is mainly defined by overlap integrals of the vacancy envelope wave function with the orbitals centered at the neighboring ions, one can assume that g_L increases with increasing average radius of the envelope function.[74] Thus, one may claim that the spatial distribution of the respective envelope functions is narrower for the ^3E states of the NV^- and for ^1E states of the V^0 center, than for the $^1T_2$ states of the V^0 centers, since the latter might be more likely to be affected by non-spherical distortions of the ion orbitals. Note that the observed g-factors for the V^0 are about one order of magnitude higher than the value of about 0.0168, which was determined by magnetic circular dichroism measurements.[75] It was claimed that the orbital angular momentum is strongly delocalized over the four dangling bonds of the highly symmetric defect center.[76]

In this context, it is worthwhile mentioning that the V^0 ZPL energies change linearly with increasing magnetic field and the ZPL energies for σ^+ and σ^- polarized excitation coincide with each other (data not shown). The latter is obviously due to the fact that the ground and excited states are spin singlets. The former indicates the absence of a state mixing, although neither the ground nor the excited states are split at zero field. This absence of state mixing may arise from the large energetic separation of about 8 meV between the ^1E and ^1A states, which results from a dynamic Jahn-Teller distortion.[77]

3.2 Circular polarization degrees of defect center PL

For further investigation, the circular polarization of the defect center ZPLs and the NV^- SST will be investigated. In order to provide a measure for the circular polarization of the PL, the degree of circular polarization, which is given by the third Stokes parameter,[78] is defined to

$$P_c^\pi = \frac{I_{\sigma^+}^\pi - I_{\sigma^-}^\pi}{I_{\sigma^+}^\pi + I_{\sigma^-}^\pi} \quad . \tag{3.3}$$

Here, $I^{\pi}_{\sigma^{\pm}}$ is the intensity of the PL. The lower index determines the polarization of the detected PL being right- or left-handed circularly polarized. The upper index gives the polarization of the exciting laser, which in this case is linearly polarized. For the magnetic field induced circular polarization degree, the alternative definition

$$P_{\mathrm{c}}^{\sigma} = \frac{1}{2}\left(\frac{I^{\sigma^+}_{\sigma^+} - I^{\sigma^+}_{\sigma^-}}{I^{\sigma^+}_{\sigma^+} + I^{\sigma^+}_{\sigma^-}} + \frac{I^{\sigma^-}_{\sigma^+} - I^{\sigma^-}_{\sigma^-}}{I^{\sigma^-}_{\sigma^+} + I^{\sigma^-}_{\sigma^-}}\right) \tag{3.4}$$

is used. Here, the upper index of the PL intensity $I^{\sigma^{\pm}}_{\sigma^{\pm}}$ indicates right- or left- handed circularly polarized excitation. Note that P_{c}^{σ} represents the mean value of the circular polarization degree obtained for circularly polarized excitation, whereas P_{c}^{π} gives the circular polarization degree under linearly polarized excitation. Moreover, the optical orientation is defined to

$$P_{\mathrm{oo}} = \frac{1}{2}\left(\frac{I^{\sigma^+}_{\sigma^+} - I^{\sigma^+}_{\sigma^-}}{I^{\sigma^+}_{\sigma^+} + I^{\sigma^+}_{\sigma^-}} - \frac{I^{\sigma^-}_{\sigma^+} - I^{\sigma^-}_{\sigma^-}}{I^{\sigma^-}_{\sigma^+} + I^{\sigma^-}_{\sigma^-}}\right) = \frac{1}{2}\left(\frac{I^{\sigma^+}_{\sigma^+} - I^{\sigma^-}_{\sigma^+}}{I^{\sigma^+}_{\sigma^+} + I^{\sigma^-}_{\sigma^+}} + \frac{I^{\sigma^-}_{\sigma^-} - I^{\sigma^+}_{\sigma^-}}{I^{\sigma^-}_{\sigma^-} + I^{\sigma^+}_{\sigma^-}}\right) \tag{3.5}$$

as a measure for the difference between the circular polarization degree under σ^+ and σ^- polarized excitation. Alternatively, P_{oo} can be understood as the mean of the circular polarization degrees with a specific circular polarization of the PL under σ^+ and σ^- polarized excitation.[79]

In the following section, the magnetic field dependence of the three polarization degrees P_{c}^{π}, P_{c}^{σ}, and P_{oo} of the defect centers PL will be addressed. In Fig 3-6 (a) the circular polarization degree P_{c}^{π} for linear polarized excitation is shown for magnetic field strengths varying between -9 and 9 T. For the NV^- ZPL in YS (red diamonds) and the high energetic V^0 ZPL in BP (blue triangles) one observes a magnetic field dependence of P_{c}^{π} symmetric around $B = 0$ T; P_{c}^{π} shows maximum values of about +4 % at highly negative fields and minimal values of about -3 % at positive fields. The magnetic field dependence of the circular polarization degree P_{c}^{σ} under circularly polarized excitation, depicted in Fig 3-6 (b) is quite comparable for the two ZPLs. The main difference is their deviation from zero at $B = 0$ T of about +2 % for the high energetic V^0 ZPL in BP and +4 % for the NV^- ZPL in YS. The latter is most likely an effect of strain due to the high concentration of nitrogen impurities in this sample.

Since a positive P_{c}^{π} or P_{c}^{σ} indicates that the ZPL is more σ^+ than σ^- polarized, this magnetic field dependence shows that at high negative magnetic fields the σ^+ polarized excited states of the NV^- or V^0 center are more likely to be occupied than the σ^+ polarized states, because their energy is smaller due to the Zeeman splitting. At high positive magnetic fields, however, it is the other way around; the σ^+ polarized states are lower in energy and therefore are more likely to be occupied. As a consequence, the ZPL is more σ^- polarized, and hence P_{c}^{π} and P_{c}^{σ} decrease. Since the Zeeman splitting of the ZPLs is rather small, due to the small orbital g-factors, the probabilities of occupation are not affected significantly. Hence, the circular polarization degrees are small, even at high magnetic fields.

For the NV^- ZPL in BP (black dots) the same tendency of P_{c}^{σ} can be seen as for the NV^- ZPL in YS and the high energetic V^0 ZPL in BP. Contrarily, for the NV^0 ZPL

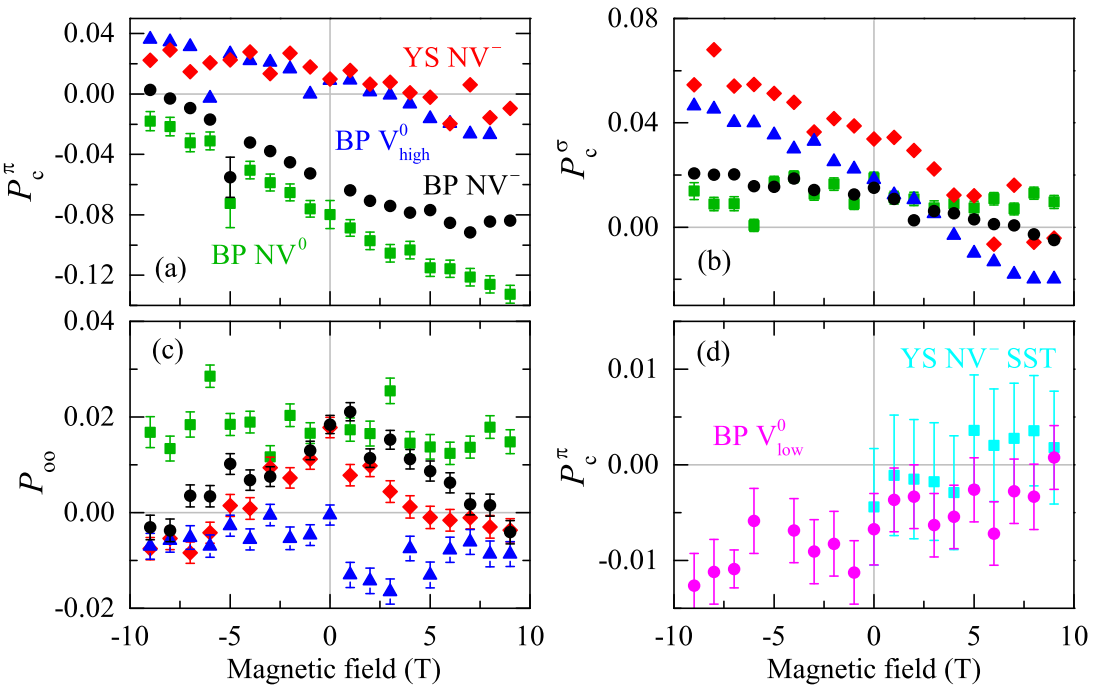

Figure 3-6: Magnetic field dependence of the circular polarization degrees (a) P_c^π, (b) P_c^σ and (c) P_{oo} of the NV^- ZPL in BP (black dots) and YS (red diamonds), as well as the NV^0 (green squares) and the high energetic V^0 ZPL (blue triangles) in BP. (d) Magnetic field dependence of the circular polarization degree P_c^π of the NV^- SST in YS (cyan squares) and the low energetic V^0 ZPL in BP (magenta dots). $T = 6$ K, $E_{ex} = 2.33$ eV. Unless shown otherwise, the experimental error does not exceed the symbol size..

in BP (green squares) a variation of P_c^σ with the magnetic field cannot be observed, see Fig. 3-6 (b). This is in accordance with the small Zeeman splitting observed for the NV^0 ZPL, compare Fig. 3-3 (d). In contrast to the rather low P_c^σ, one can observe a remarkable magnetic field dependence of P_c^π, as shown in Fig 3-6 (b). For the NV^- ZPL, P_c^π is about zero at -9 T, but strongly decreases down to about -9 % at positive fields. For the NV^0 ZPL the P_c^π values are even more pronounced; one observes -2 % at -9 T and -13 % at 9 T. This high circular polarization of the ZPLs at excitation with linear polarized light might arise from the more symmetric NV center orientation in this excitation geometry.[80]

BP is excited along the (001) direction, in this geometry the two dimensional projection of the tetrahedral NV center orientation, indicated by the four NV center symmetry axes (111), $(1\bar{1}\bar{1})$, $(\bar{1}1\bar{1})$, and $(\bar{1}\bar{1}1)$,[81] is reduced to a rectangular cross, as can be seen in Fig. 3-7 (b). A detailed explanation of this symmetry transformation including a discussion of the influence of the NV center orientation on its polarizability is given in Sec. 4.1. In Fig. 3-7 (a) the circular polarization degree P_c^π of the NV^- ZPL is depicted dependent on the sample rotation around the (001) axis for

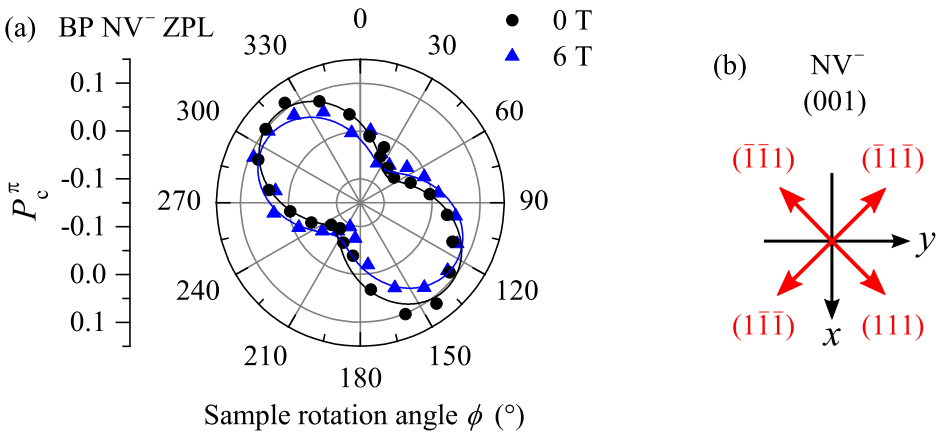

Figure 3-7: (a) Angular dependence of the NV^- ZPL circular polarization degree P_c^π at $B = 0$ T (black dots) and 6 T (blue triangles). The solid lines are sine based fits according to Eq. (3.6). The experimental error does not exceed the symbol size. (b) 2D projection of the NV^- center symmetry axes (red arrows) in the (001) direction.

$B = 0$ T (black dots). Note that the exciting light is linearly vertically polarized. One can clearly see that P_c^π varies between -10 % and $+10$ % and shows a 180° periodicity. A fit with a sine function according to

$$P_c^\pi(\phi) = A_c \cdot \sin(2\phi + \phi_0) + b_c \quad , \tag{3.6}$$

with amplitude $A_c = 0.088 \pm 0.004$, phase shift $\phi_0 = (90 \pm 1)°$, and offset $b_c = 0.016 \pm 0.003$ describes the data well. It becomes apparent that P_c^π is maximal at about 135° and 315°, at this angle the polarization plane of the exciting laser light is parallel to the 2D projection of the NV centers oriented along the (111) and the $(\bar{1}\bar{1}1)$ directions, compare Fig. 3-7 (b). Since the dipoles of the NV centers are oriented perpendicular to the symmetry axes of the NV center,[70] such an excitation is not an efficient for these centers.[17] However, in this geometry the polarization plane of the exciting laser is parallel to the dipole moments of the NV^- centers oriented along the $(\bar{1}1\bar{1})$ and $(1\bar{1}\bar{1})$ directions. Hence, these centers can efficiently be excited. This leads to the conclusion that these centers mainly emit σ^+ polarized ZPLs. Vice versa, the NV^- centers which are efficiently excited at a sample rotation of 45° and 225°, which are the centers oriented along (111) and $(\bar{1}\bar{1}1)$, mainly emit σ^- polarized ZPLs. At sample rotation angles of 0°, 90°, 180°, and 270° all NV^- centers are excited. Hence, no ZPL polarization is preferably emitted and therefore P_c^π is close to zero. It is worthwhile mentioning that the NV^- centers which preferably emit σ^+ polarized ZPLs are inclined towards the optical axis ($z = 1$) and the NV^- centers which preferably emit σ^- polarized ZPLs are inclined away from the optical axis ($z = -1$).

The presence of an external magnetic field of $B = 6$ T (blue triangles) does not widely affect the amplitude $A_c = 0.075 \pm 0.005$ or offset $b_c = 0.011 \pm 0.004$, but a remarkably different phase shift $\phi_0 = (79 \pm 2)°$ can be observed. The latter indicates

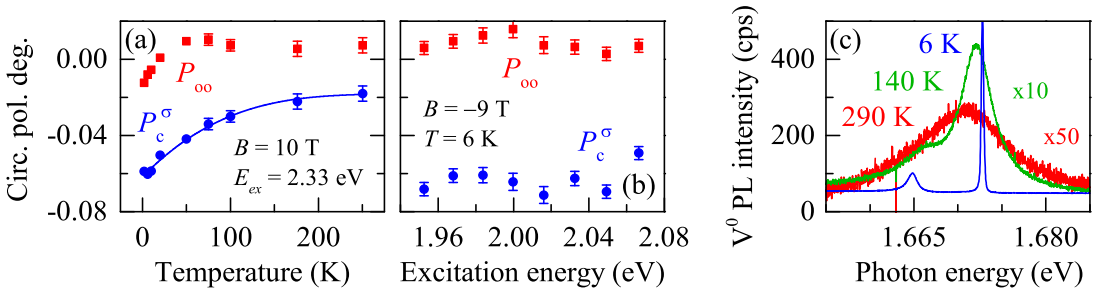

Figure 3-8: Circular polarization degrees P_c^σ (blue dots) and P_{oo} (red squares) of the NV^- ZPL in YS at $B = 10$ T dependent on (a) temperature and (b) excitation energy. The solid line is a third-order polynomial fit. If not shown otherwise, the experimental error does not exceed the symbol size. (c) PL spectra of the V^0 ZPLs in BP at different temperatures. Note that the green (red) spectrum is scaled with a factor of 10 (50). $E_{ex} = 2.33$ eV.

a magnetic field induced phase shift of $\Delta\phi_0 = (11 \pm 2)°$. This rotation of the angular dependence of the NV^- ZPL polarization can be explained by a tilting of the NV^- center dipole axis due to a magnetic torque of the external field acting on the magnetic moments of the NV^- centers electrons.[82, 83, 84] A similar behavior is seen for the linear polarization degree, too. Here, a phase shift of $\Delta\phi_0 = (27 \pm 1)°$ can bee observed at $B = 6$ T, which will be addressed in Sec. 4.4.

The magnetic field dependence of the optical orientation P_{oo} of the defect centers' ZPLs is depicted in Fig. 3-6 (c). The NV^0 (green squares) as well as the high energetic V^0 ZPL (blue triangles) show no dependence on the external magnetic field; they are more or less constant at a value of about 2 % and −1 %, respectively. In contrast to that, P_{oo} is about 2 % at $B = 0$ T for the NV^- ZPL in BP (black dots) and YS (red diamonds), but vanishes at high magnetic field strengths.

The SST of the NV^- center in YS (cyan squares) and the low energetic V^0 ZPL in BP (magenta dots) show no significant circular polarization. As one can see in Fig. 3-6 (d), P_c^π is approximately zero in terms of accuracy. However, one may attribute a positive slope to the P_c^π evolution of the low energetic V^0 ZPL, which would be in good agreement with the negative Zeeman splitting observed for this center; compare Sec. 3.1.5.

Finally, the temperature dependence of the circular polarization degrees should be addressed. In Fig 3-8 (a) P_c^σ (blue dots) and P_{oo} (red squares) of the NV^- ZPL in YS are depicted dependent on the temperature at a magnetic field of $B = 10$ T. Both polarization degrees converge to zero with rising temperature. While P_{oo} increases from about −1 % at low temperatures to 1 % at about 50 to 70 K and then slowly decreases to zero, P_c^σ reduces in absolute terms from −6 % at low temperature to about −2 % at 250 K. The evolution of P_c^σ can be fitted well with a polynomial function of third order ($\propto T^3$); see solid blue line. The decrease of polarization at high temperatures is most likely due to polarization destroying electron-phonon coupling, since such processes become more likely at high temperatures due to the higher phonon densities. In contrast

to the circular poalrization degrees, the linear polarization degree is comparably high at room temperature, compare Sec. 4.3. Therefore, one can conclude that the phonons couple more efficiently to the excited states with non-zero spin and orbital angular momentum. This effective spin-orbit coupling plays a major role for the states involved in the emission process of the circularly polarized ZPLs. Note that a saturation of the polarization degree is not expected at low temperatures, since the corresponding Zeeman splittings are smaller than the thermal energy $E_T = k_\mathrm{B}T$ (with k_B being the Boltzmann constant) for the whole range of external magnetic field strengths. Therefore, it would be a viable conclusion to study the circular polarization degrees at temperatures below 1 K to exclude any phonon coupling contributions.

It is worthwhile to mention that the circular polarization degrees of the NV^- and NV^0 ZPLs in BP demonstrate similar temperature dependences (data not shown). The circular polarization degrees of the V^0 ZPLs decrease even more rapidly with rising temperature. In Fig 3-8 (c) the respective ZPLs measured at different temperatures are shown. The ZPLs strongly broaden with increasing temperature; from 6 K (blue line) to 140 K (green line) the linewidths of the ZPLs enhance by more than one order of magnitude. At room temperature (red line), the two ZPLs related to the V^0 centers cannot be distinguished anymore.

The dependence of the circular polarization degrees P_{oo} and P_c^σ on the excitation energy is presented in Fig 3-8 (b), for $B = -9$ T and $T = 6$ K. As one can see, P_c^σ and P_{oo} remain fairly constant at about -6 % and 0.5 % respectively, for tuning the excitation energy between 1.95 and 2.07 eV. Thus, the variation in the excitation energy has a negligible impact on the circular polarization degrees.

3.3 Conclusion

A significant Zeeman splitting is observed for the NV^- and V^0 ZPLs, but not for the NV^0 ZPL. However, due to the small effective orbital g-factor compared to typical electron g-factors, which are about one order of magnitude larger, the Zeeman splittings are rather small. As a consequence, the circular polarization degrees exhibit only a few percent, even at high magnetic field strengths. However, the degree of polarization can be enhanced to about 10 % by selectively exciting NV^- centers with specific geometry. The orientation of the NV^- center dipole with respect to the optical axis results in a preference of the emitted ZPL for circular polarization. Furthermore, the energetic ordering of the defect centers' energy level structures can be verified for the NV^- center, whereas the V^0 level structure of the ground state had to be reordered in comparison with previously published data. In addition, it is found that the ground state of the NV^0 center, which has ^2E symmetry, actually shows an orbital angular momentum contribution comparable to a ^2A symmetry, due to a mixing of the corresponding spin orbit states with $m_\mathrm{L} = \pm 1$.

Chapter 4

Linear polarization characteristics of defect center PL

In this chapter the linear polarization properties of the PL for different defect centers in diamond are thoroughly analyzed. While the main focus lies on the NV^- center, the NV^0 and the V^0 center are considered as well. In Sec. 4.1 the experimental details are outlined and basic physical measures to describe the linear polarization characteristics of light are defined. For the investigation of the polarization features, particular attention is drawn to the crystal orientation with respect to the electric field of both, the exciting laser light as well as the emitted PL. In Sec. 4.2 distinctive anisotropies in the angular dependence of the linear polarization of the defect center emission are presented. In this context, a theoretical approach based on the symmetry and dipole orientation of the NV center is developed, in particular for the (001) direction, in order to explain the observed polarization anisotropies. Additionally, the effect of temperature, excitation energy, and power on the linear polarization characteristics are investigated in Sec. 4.3. Sec. 4.4 contains a detailed analysis of the influence of high magnetic fields on the linear polarization properties of the defect centers ZPL emission. This chapter closes with concluding remarks in Sec. 4.5. Note that this chapter covers the results published in [80].

4.1 Sample geometry and linear polarization degree

The linear polarization experiments were performed on the setup visualized and described in Sec. 2.1. Sample BP was used for excitation along the (001) axis, whereas for excitation along the (111) and the $(\bar{2}11)$ direction YS served as the sample, compare Sec. 2.4. In Fig. 4-1 (a) sketches of both samples are depicted, together with the corresponding optically excitable axes, which were used in the experiment. Note that the $(01\bar{1})$ axis in YS was not investigated. Due to the rather small base face and the rod shape of the sample, optical excitation along the $(01\bar{1})$ direction is barely feasible.

In order to characterize the polarization properties of the PL, the linear polarization

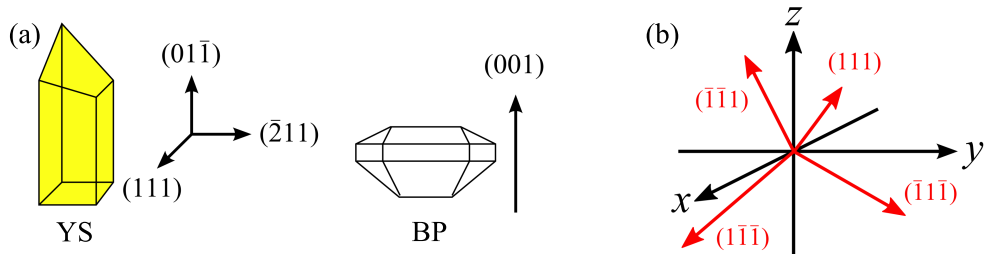

Figure 4-1: (a) Scheme of the examined samples YS and BP, with their optically accessible symmetry axes. (b) Tetrahedral orientations of NV centers (red arrows) in a diamond crystal.

degree is defined to

$$P_{\text{lin}} = \frac{\sqrt{S_1^2 + S_2^2}}{S_0} \quad , \tag{4.1}$$

determined by the Stokes parameters $S_0 = I_{0°} + I_{90°}$, $S_1 = I_{0°} - I_{90°}$ and $S_2 = I_{45°} - I_{135°}$.[78] The index of PL intensity I indicates the angle of the detected linear polarization plane with respect to the polarization plane of the exciting light, which was retained unchanged throughout the measurements. By analogy with the Faraday rotation angle, we define the rotation of the linear polarization plane by

$$\theta = \frac{180°}{2\pi} \arctan\left(\frac{S_2}{S_1}\right) \quad . \tag{4.2}$$

For analyzing the angular dependence of the linear polarization, the rotation degree θ can be understood as the angular change of P_{lin}.

4.2 Angular dependence of the linear polarization

In this section the influence of the diamond-crystal and the defect-center symmetry-axes orientation on the polarization properties of the corresponding ZPL will be investigated. Therefore, the geometry of the NV center will be discussed in the following section. Due to the lattice symmetry of the diamond crystal, there are only four possible orientations for the NV center, which are the (111), (1$\bar{1}\bar{1}$), ($\bar{1}$1$\bar{1}$), and ($\bar{1}\bar{1}$1) direction.[81] Note that this applies for the NV^- as well as for the NV^0 center. In Fig. 4-1 (b) these orientations of NV centers, which are described by the C_{3v} symmetry group, are illustrated. The NV center orientations (red arrows) correspond to the electron bonding axes between the carbon atoms of the diamond crystal. In context of the experiment however, only the two-dimensional (2D) projections along the optically accessible crystallographic axes are important, since these projections represent the symmetry of the NV centers in direction of the light field.

All excitation geometries will be discussed for the linear polarization of the NV^- ZPL in the following, starting with the (001) direction, including the deduction of a

theoretical description in Sec. 4.2.1. The NV^0 and V^0 center as well as the Raman line will be elaborated subsequently in Sec. 4.2.2 for the (001) direction only. Fig. 4-2 (a) shows the 2D projection along the (001) direction; one can clearly see that the three-dimensional configuration of NV center axes according to a tetrahedral symmetry is reduced to a rectangular cross (see red arrows) lying in the xy-plane. The dependence of P_{lin} of the NV^- ZPL on the diamond crystal rotation around the (001) direction is depicted to the right of this projection in Fig. 4-2 (a). The value of P_{lin} varies periodically between 0.09 and 0.32. A fit with a sine function according to

$$P_{\text{lin}}(\phi) = K \sin\left(\frac{2\pi}{p}\phi + \phi_0\right) + \kappa, \tag{4.3}$$

gives the four independent fitting parameters amplitude $K = 0.098 \pm 0.008$, periodicity $p = (90.6 \pm 0.9)°$, phase shift $\phi = (0 \pm 2)°$, and offset $\kappa = 0.215 \pm 0.005$. The pronounced 90° periodicity becomes apparent: at about $\phi = 45°$, P_{lin} reaches a maximum. At this angle the polarization plane, more specifically the electric field vector of the NV^- ZPL emission, coincides with the NV center symmetry axis $(\bar{1}1\bar{1})$. Further maxima of P_{lin} can be observed at about $\phi = 135°$, 225°, and 315°. They are in line with the other three symmetry axes of the NV center. The minima, however, can be found, when the polarization plane is in between two of the NV center symmetry axes at about $\phi = 0°$, 90°, 180° and 270°. Apparently this strong anisotropic angular dependence of P_{lin} mirrors the rectangular symmetry of the 2D projection of the NV center orientations.

Similar observations can be made for P_{lin} of the NV^- ZPL emitted along the (111) direction. As shown in Fig. 4-2 (b), the total polarization is weaker and the variation in the polarization degree is only about 0.04, yet one can still see a clear 120° periodicity. In fact, this mirrors the tripod symmetry of the corresponding 2D projection of the NV centers orientation in (111) direction. The tripod symmetry appears because the NV centers oriented along the (111) axis coincide with the optical axis. The maximal P_{lin} of about 0.17 can be observed at roughly 90°, when the polarization plane is perpendicular to the $(\bar{1}1\bar{1})$ direction, whereas the minimum of about 0.13 can be found around 270°.

In contrast to the afore described symmetries, the P_{lin} of the NV^- ZPL emitted along the $(\bar{2}11)$ direction demands a more complex explanation, as shown in Fig. 4-2 (c). Here P_{lin} varies between 0.32 and 0.15 with a 90° periodicity, similar to the one shown in Fig. 4-2 (a), whereas the 2D projection of the NV center orientation shows just a reflection symmetry along the x-axis, but no periodicity. Another main difference of this 2D projection in comparison to the others is that the projections of the NV-center symmetry axes differ in length. For example, the $(1\bar{1}\bar{1})$ axis is almost parallel to the optical axis. Therefore its projection vector is rather short. However, there is at least some relation between the P_{lin} angular dependence and the 2D projection, since the maximum of P_{lin} at about 0° coincides with the (111) axis. In contrast to that, such a simple relation can not be found for the other three maxima of P_{lin} and the corresponding NV center directions.

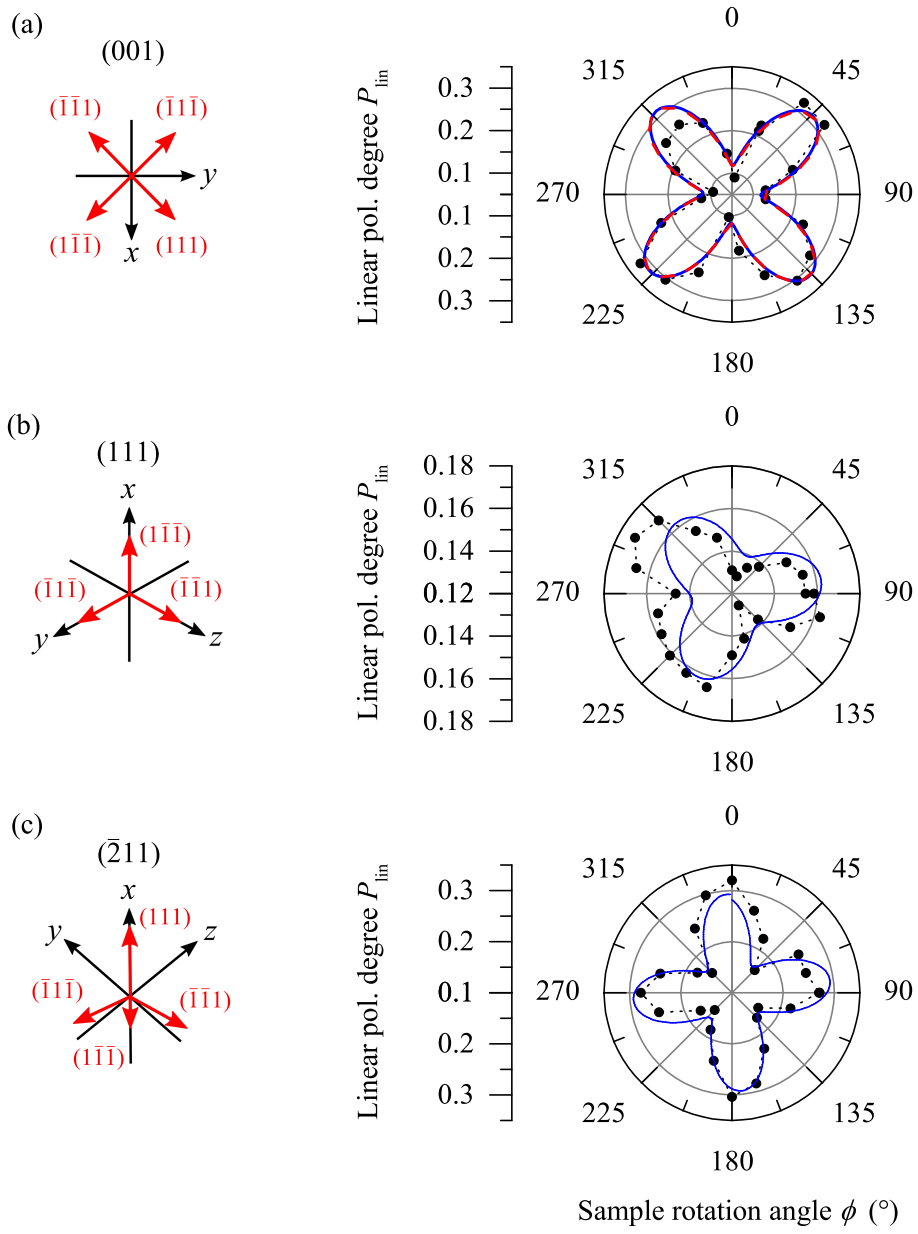

Figure 4-2: 2D projection of the NV center orientation (red arrows) and linear polarization degree P_{lin} (black dots) of the NV^- ZPL with optical axis along (a) the (001), (b) the (111), and (c) the $(\bar{2}11)$ direction, as a function of the sample rotation degree ϕ; $T = 6$ K, $B = 0$ T, $E_{\mathrm{ex}} = 2.33$ eV for the (001), 2.21 eV for the (111) and $(\bar{2}11)$ direction, $p_{\mathrm{ex}} = 10$ mW for the (001), 5 mW for the (111), 3 mW for the$(\bar{2}11)$ direction. The blue solid lines are sine based fit functions according to Eq. (4.3), the red dashed line is a fit function based on Eg. (4.6). Dashed black lines are guides to the eye. The experimental error does not exceed the symbol size.

4.2.1 Symmetry based theoretical description for the (001) direction

In order to explain the correlation between the anisotropies of P_{lin} and the orientation of the NV center, the observations along the (001) direction will be discussed in further detail because of the high symmetry in this geometry. In the following considerations and for further investigations the main focus will therefore lie on this geometry.

As a phenomenological approach, a relation between the polarization degrees of the exciting laser light and the NV^- PL is calculated by taking only the diamond crystal symmetry and the NV center orientation into account. This relation can be mathematically expressed with the rank-four tensor A_{ijkn} as follows:

$$\langle E_i^{\mathrm{PL}} E_j^{\mathrm{PL}*} \rangle = A_{ijkn} \langle E_k^{\mathrm{ex}} E_n^{\mathrm{ex}*} \rangle \quad . \tag{4.4}$$

Here, E_i^{PL} and E_i^{ex} are the components of the electric field vectors of the emitted PL and, respectively, the exciting light. Hence, $\langle E_i^{\mathrm{PL}} E_j^{\mathrm{PL}*} \rangle$ and $\langle E_k^{\mathrm{ex}} E_n^{\mathrm{ex}*} \rangle$ are the components of the non-normalized polarization tensor.[85] Since it is a phenomenological expression, A_{ijkn} only depends on the symmetry of investigated object. Therefore, it is necessary to have a closer look at the symmetry of the NV^- center in diamond.

For an excitation along the (001) direction, only the 2D projection on the xy-plane is important. This projection, which is depicted in Fig. 4-2 (a), is shaped like a rectangular cross; accordingly, the complex three-dimensional symmetry of the four NV^- center symmetry axes can be reduced to a cubic symmetry. For a cubic symmetry, one obtains $A_{iiii} = A_{11}$, $A_{iijj} = A_{12}$, $A_{ijij} = A_{44}$ and $A_{ijji} = A_{47}$ with $i \neq j$, while all other tensor components are zero.[86] Furthermore, only linear polarization is considered and it is assumed, in good agreement with the experimental conditions (compare Sec. 2.1), that the exciting laser beam and the emitted PL emission are parallel to the (001) axis. The linear polarization degree is then defined by

$$P_{\mathrm{lin}}(\phi) = \frac{b}{2a} \cos(4\phi + \phi_0) + \frac{b + 2c}{2a} \quad . \tag{4.5}$$

The parameters are given by $a = A_{11} + A_{12}$, $c = A_{44} + A_{47}$ and $b = A_{11} - A_{12} - A_{44} - A_{47}$. Finally, $P_{\mathrm{lin}}(\phi)$ can be described by

$$P_{\mathrm{lin}}(\phi) = A \cos(4\phi + \phi_0) + d \quad , \tag{4.6}$$

with the two independent parameters amplitude A and offset d according to

$$A = \frac{b}{2a} \quad \text{and} \quad d = \frac{b + 2c}{2a} \quad . \tag{4.7}$$

In addition, a relation for the angular dependence of the rotation θ of the polarization plane is deducted, due to the fact that θ can be understood as the angular change of P_{lin}:

$$\frac{\mathrm{d}P_{\mathrm{lin}}(\phi)}{\mathrm{d}\phi} \propto \theta(\phi) = C \cos(4\phi + \phi_0 + 45^\circ) + e \quad , \tag{4.8}$$

with the amplitude C and offset e. A fit based on Eq. (4.6) (red dashed line) describes the angular dependence shown in Fig. 4-2 (a) quite well. The fitting parameters $A = 0.098 \pm 0.008$, $\phi_0 = (-1 \pm 1)^\circ$ and $d = 0.216 \pm 0.005$ are very similar to the ones obtained by the sine based fit function (blue solid line) according to Eq. (4.3).

In order to gain further insight into the observed P_{lin} anisotropy of the NV^- ZPL, the ZPL emission process should be discussed in detail by taking the fine structure of the NV^- center into account, compare Sec. 1.3. The NV^- ZPL is a spin conserving optical transition between the first-excited state ^3E and the ground state $^3A_2$. Since linear polarization properties are analyzed, the focus lies on the linearly polarized transitions only. These involve the states with zero spin and orbital angular momentum projections, namely the excited states E_x, E_y and the $^3A_{20}$ ground state. The ZPL photons, emitted during the relaxation process involving these states, are linearly polarized along the dipole axis, which is perpendicular to the symmetry axis of the NV^- centers.[6, 70] Vice versa, in order to excite an electron to the linearly polarized states, the polarization of the exciting light must be perpendicular to the NV^- centers' symmetry axes too, especially, for resonant excitation.[17]

In the case of optical excitation along the z-axis, the exciting light is for instance polarized along the xy-diagonal, compare Fig. 4-2 (a). Thus, only two NV^- centers are linearly excited. In turn, solely these two NV^- centers contribute to the emission process of the linearly polarized ZPL. Since the dipoles of these centers are oriented parallel, the polarization plane of the ZPLs emitted by these NV^- centers are parallel too; hence P_{lin} is maximized. However, when the exciting light is polarized along the x- or y-axis, every NV^- center is excited and contributes to the emission process of the ZPL. But, since the dipole orientations of the $(\bar{1}\bar{1}1)$ and (111) NV^- centers are perpendicular to the orientations of the $(\bar{1}1\bar{1})$ and $(1\bar{1}\bar{1})$ NV^- center dipoles, the polarization planes of the ZPL emissions by these centers are perpendicular too. Therefore, the total linear polarization is reduced and P_{lin} decreases. Note that a linearly polarized excitation of the NV^- centers in fact creates electrons in both linearly and circularly polarized excited states. As a consequence, the ZPL emission consists of linearly as well as circularly polarized contributions. A detailed analysis of the circular polarization properties of the NV^- center PL is presented in Chapter 3.

4.2.2 Linear polarization anisotropies in the (001) direction

In order to verify the quality of the deduction, the phenomenological approach will be extended to the linear polarization characteristics of other defect centers too. In this context not only the NV^0 and the V^0 center, but also the 1332 cm^{-1} Raman line of diamond will be investigated.

In Fig. 4-3 (a) P_{lin} of the neutral NV^0 center ZPL is depicted as a function of the sample rotation angle. Since the symmetry is the same for NV^0 and NV^-, again an anisotropy with a 90° periodicity is seen. Here P_{lin} varies between 0.02 and 0.25, and therefore it is about 0.07 smaller compared to the NV^- ZPL. The angular shape can be described sufficiently by Eq. (4.6).

Furthermore, the polarization properties of the 1332 cm^{-1} Raman line, which

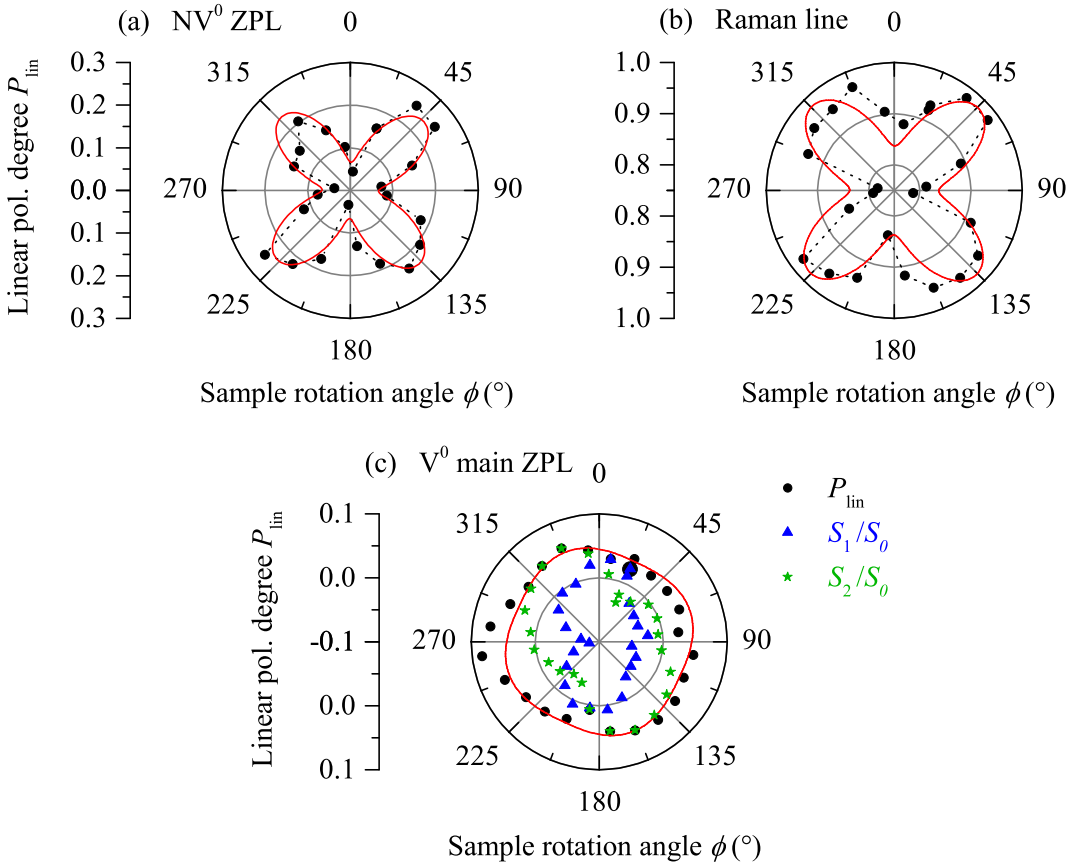

Figure 4-3: Linear polarization degree P_{lin} (black dots) of (a) the NV^0 ZPL, (b) Raman line and (c) V^0 main ZPL together with the normalized Stokes parameters S_1/S_0 (blue triangles) and S_2/S_0 (green stars) as functions of the sample rotation angle ϕ; $T = 6$ K, $B = 0$ T, $E_{\text{ex}} = 2.33$ eV, $p_{\text{ex}} = 10$ mW. The optical axis is oriented along (001). The fit curves (red solid lines) are cosine functions according to Eq. (4.6). Dashed lines are guides to the eye. The experimental error does not exceed the symbol size.

indicates a vibration of the two diamond Bravais lattices relative to each other, are investigated.[63, 64] As it is shown in Fig. 4-3 (b), the Raman line is strongly linearly polarized; P_{lin} varies between 0.97 and 0.78. As in the case of the NV center, the angular evolution can be modeled in good agreement with Eq. (4.6). Hence, our phenomenological approach is valid not only for PL, but also for inelastic light scattering. This is well in line with previous investigations. In [87] J. Mossbrucker et al. observed a similar anisotropy in the linear polarization degree of the Raman line in diamond along the (001) direction. They found that the linear Raman-line polarization is maximized, as shown in our case, when the polarization of the incident light is parallel to the 2D projections of the diamond lattice and the optical axis. In order to mathematically describe this anisotropy, they used the approach that

interaction with light induces a dipole moment in a polarizable material. The polarizability, however, depends on the configuration of the material, which is a function of the vibrational motion of the nuclei. Analog to our phenomenological approach, presented in Sec. 4.2.1, J. Mossbrucker et al. take only the symmetry of the examined structure into account. Their experimental findings are, similar to the observations presented here, that the polarization of the Raman line is maximal when the polarization of the incident light is parallel to the 2D projections of the diamond lattice along the optical axis. In this configuration the polarizability of the diamond crystal is maximal, therefore the polarization of the photons is preserved during the Raman scattering process and the observed P_{lin} is close to unity.

To complete the picture, the V^0 center is additionally studied. This center has a tetrahedral T_d symmetry, which is quite comparable to the NV center C_{3v}, since the four axes which connect the vacancy with the four next neighbor C-Atoms are the four NV-center symmetry axes (111), $(1\bar{1}\bar{1})$, $(\bar{1}1\bar{1})$ and $(\bar{1}\bar{1}1)$.[43] Therefore, the theoretical approach should also apply for this defect center and Eq. (4.6) should be valid too. The P_{lin} of the V^0 main ZPL is presented in Fig. 4-2 (c) dependent on the sample rotation angle ϕ. In contrast to the previous findings, P_{lin} is quite small. It exhibits values between 0.02 and 0.08; the variation with angle is barely higher than the experimental error. A fit to the data according to Eq. (4.6) gives acceptable results, but does not seem appropriate. In contrast to the NV center, the V^0 center has no static dipole moment due to the high symmetry of its electron distribution. As a result, P_{lin} is small and a significant anisotropy in the angle dependence cannot be observed.

There is, however, an anisotropic deviation at about 270°, but in terms of accuracy its significance is questionable. In order to get a more detailed picture, a closer look at the Stokes parameters, which were measured to calculate P_{lin}, see Eq. (4.1), is taken. In contrast to P_{lin}, the normalized Stokes parameters S_1/S_0 (blue triangles) and S_2/S_0 (green stars) both show an 180° anisotropy with symmetry axes around 0° for S_1/S_0 and 135° for S_2/S_0. This anisotropy is in line with the V^0 centers T_d symmetry, which is also invariant under rotation around 180°. Moreover, the anisotropy indicates a symmetry reduction, which might be due to Jahn-Teller coupling. Static Jahn-Teller coupling would lead to reduction of the T_d symmetry to a tetragonal D_{2d} symmetry, resulting in an electric dipole moment along the (100) direction.[30] However, theoretical calculations have shown that the T_d is maintained due to dynamic Jahn-Teller distortion. At low temperatures, the formation energies for T_d and D_{2d} symmetry only differ by about 3 meV. Hence, some V^0 center might actually have D_{2d} symmetry.[77]

In addition to the linear polarization degree, the rotation θ of the linear polarization plane is a useful measure to understand the polarization characteristics of the defect center ZPLs. Again, the NV^- ZPL will be considered first. Fig. 4-4 (a) shows the dependence of θ on the sample rotation ϕ, which is in good agreement with Eq. (4.8). As one can see, θ varies between -23° and 8° with 90° periodicity. One gets a similar picture for the NV^0 ZPL, depicted in Fig. 4-4 (b). The periodicity is the same, while the amplitude of θ is even bigger than for the NV^-; one can observe a variation between -40° and 32°. Again, a fit function based on Eq. (4.8) describes the anisotropy quite well. The fact that the rotation of the linear polarization plane changes its sign indicates

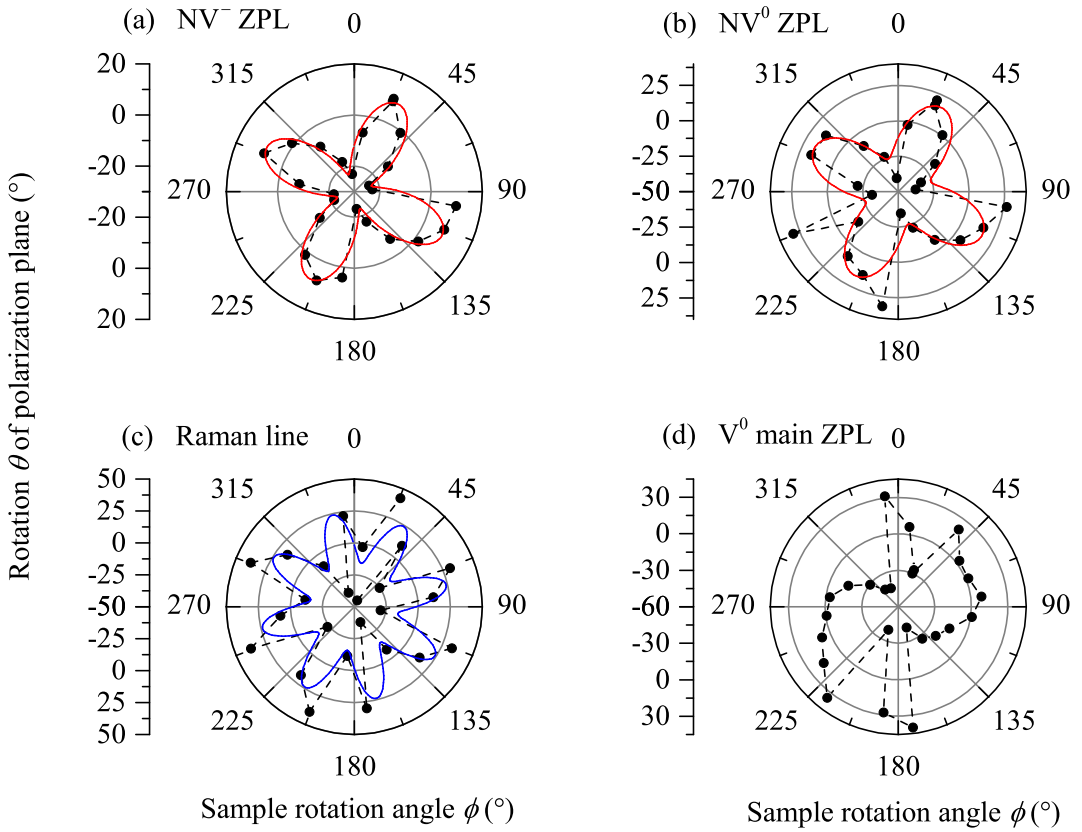

Figure 4-4: Rotation of polarization plane θ of (a) the NV^- and (b) NV^0 ZPL, (c) Raman-line, and (d) V^0 main ZPL as functions of the sample rotation angle ϕ; $T = 6$ K, $B = 0$ T, $E_{ex} = 2.33$ eV, $p_{ex} = 10$ mW. The optical axis is oriented along the (001) direction. The fit curves (red line) are cosine functions according to Eq. (4.8), the blue line is a sine fit function. Dashed lines are guides to the eye. The experimental error does not exceed the symbol size.

a switching between radiative electron states of orthogonal linear polarizations. In this context, the rotation of the crystal by 45° can be understood as a binary polarization modulation, which selects the orthogonal transition dipoles[70] which contribute to the linearly polarized ZPL emission.

Once more, Raman scattering is taken into account. In Fig. 4-4 (c) the angular dependence of θ is pictured. A rather strong variation with its minimum at -44° and maximum at 42° is observed. In contrast to the angular dependence of P_{lin}, which had a 90° periodicity, now a 45° periodicity is observed for θ, which can be fitted best with a sine function. Moreover, the polarization of the V^0 main ZPL, presented in Fig. 4-4 (d), provides another, different picture. While P_{lin} is quite small, compare Fig. 4-3 (c), θ varies between -42° and 40°. In contrast to all other periodicities observed so far, the here observed 180° periodicity can not be fitted well with a simple sine function. Apparently, the phenomenological approach to deduct an equation for θ seems only valid

for NV centers rotated around the (001) direction, but neither for Raman scattering nor the V^0 center. It is, however, valid to describe the angular dependence of P_{lin} for the NV ZPLs and the Raman line because the assumption of a cubic symmetry applies here.

4.3 Temperature, excitation energy, and power dependence of the linear polarization

To investigate the influence of the experimental conditions on the polarization properties of the defect center PL, namely energy and power of the exciting laser light as well as the temperature of the sample, the focus will now lie on the polarization characteristics of primarily the NV^- ZPL. A detailed analysis on the influence of an external magnetic field will follow separately. Note that all temperature measurements were performed for YS with the optical axis along the (111) direction. To ensure good results, a sample rotation angle of $\phi = 90°$ was chosen, since P_{lin} of the NV^- ZPL is maximal at this angle. Measurements to determine the excitation energy and power dependence were executed for BP in (001) direction with a sample rotation angle of $\phi = 45°$.

Fig. 4-5 (a) shows the temperature dependence of P_{lin} (black dots) and θ (red triangles) of the NV^- ZPL. At temperatures below 4.2 K P_{lin} reaches 0.25, but rapidly decreases when the temperature rises. However, it reaches a value of 0.13 ± 0.01 at about 10 to 20 K and does not decrease any further; even at room temperature the linear polarization degree remains at about 13 %. In contrast to this, θ shows a weak temperature dependence. For temperatures below 50 K, θ is around $(-11 \pm 2)°$. However, above 50 K it slightly increases to about $(-8 \pm 2)°$. It is worthwhile mentioning that the polarization is higher in other geometries. When the optical axis is oriented along the $(\bar{2}11)$ direction, P_{lin} is about 0.32 at 6 K and 0.22 at room temperature (data not shown). Note that only the linear polarization has a high temperature robustness. In contrast to that, the circular polarization decreases strongly with temperature, compare Fig. 3-8.

For single NV centers it was found that all polarization of the ZPL emission vanishes due to a population transfer between the excited states of the NV^- center at temperatures above 40 K.[88, 89] This population transfer is coupled to a degenerated vibrational mode, which is a consequence of the Jahn-Teller effect.[90, 91] In addition to the decrease of polarization, another consequence of this population transfer is the strong broadening of the NV^- ZPL, following a T^5 dependence. The observed temperature dependences are however much weaker. As illustrated in the inset of Fig. 4-5 (b), the full width at half maximum (FWHM) of the NV^- ZPL shows a dependence according to $T^{1.9\pm0.1}$. This temperature dependence of the FWHM hints at a weak inhomogeneous broadening of the NV center ensemble, which might be due to a high homogeneity of the diamond crystal. Furthermore, the energy of the NV^- ZPL shows a dependence following $T^{2.9\pm0.2}$. In Fig. 4-5 (b) the energy shift $\Delta E_{\mathrm{ZPL}}(T) = E_{\mathrm{ZPL}}(T = 1.8\ \mathrm{K}) - E_{\mathrm{ZPL}}(T)$ (red triangles) is illustrated as a function of the sample temperature. The temperature dependence of the energy shift can be

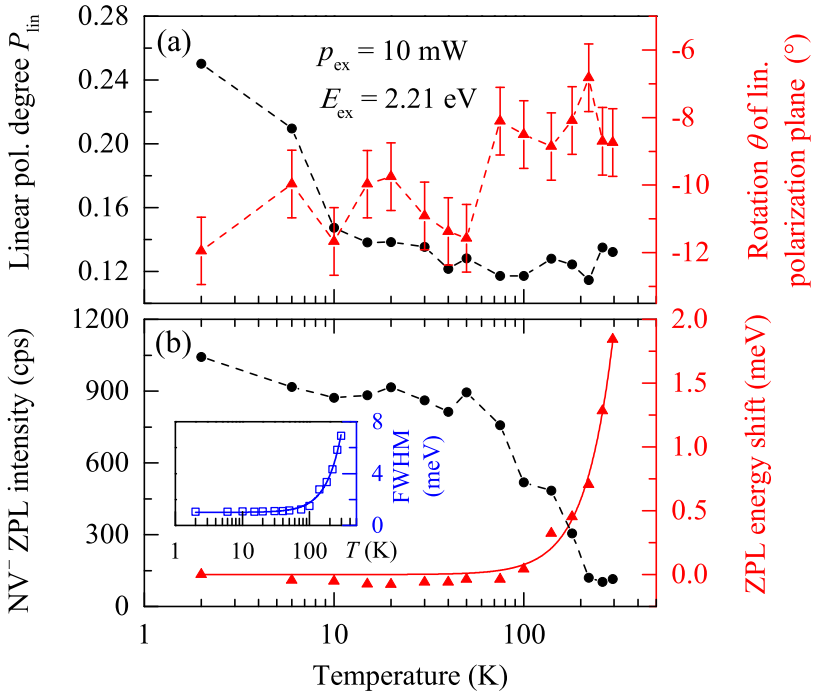

Figure 4-5: (a) Dependence of linear polarization degree P_{lin} (black dots, left scale) and rotation of polarization plane θ (red triangles, right scale) of the NV^- ZPL on the temperature. (b) Intensity (black dots, left scale) and ZPL peak energy shift (red triangles, right scale) of the NV^- ZPL as a function of the temperature. The inset shows the temperature dependence of the full width at half maximum of the NV^- ZPL (blue squares). The optical axis is oriented along the (111) direction. The fit functions (solid curves) are power functions. Dashed lines are guides to the eye. Unless shown otherwise, the experimental error does not exceed the symbol size.

related to an electron-phonon coupling resulting from a long-range interaction between the NV centers and other defects, which is modulated by long-wave acoustic phonons[92] and a softening of the NV centers' bonds, which leads to an enhanced low-energy phonon density in the excited states.[93] A Raman process, however, can be neglected, since it typically shows temperature dependences of higher order.[94] Moreover, the NV^- ZPL intensity (black dots) decreases with increasing temperature, see Fig. 4-5 (b). At low temperatures one observes an intensity of about 1000 cps, but at temperatures above 50 K the intensity decreases to about 100 cps at room temperature. In addition, the high P_{lin} at room temperature is an evidence that the Jahn-Teller effect is less important for an ensemble of NV centers and that an orbital averaging of the excited states to practically one excited state at high temperatures is not present in the samples studied in the frame of this thesis.[72, 67]

A variation of the excitation energy of the laser from 2.01 to 2.21 eV does not show a significant change in the NV^- ZPL P_{lin}, as illustrated in Fig. 4-6 (a). In terms of accuracy, P_{lin} is more or less constant at a value of about 0.21 ± 0.01. Apparently, the

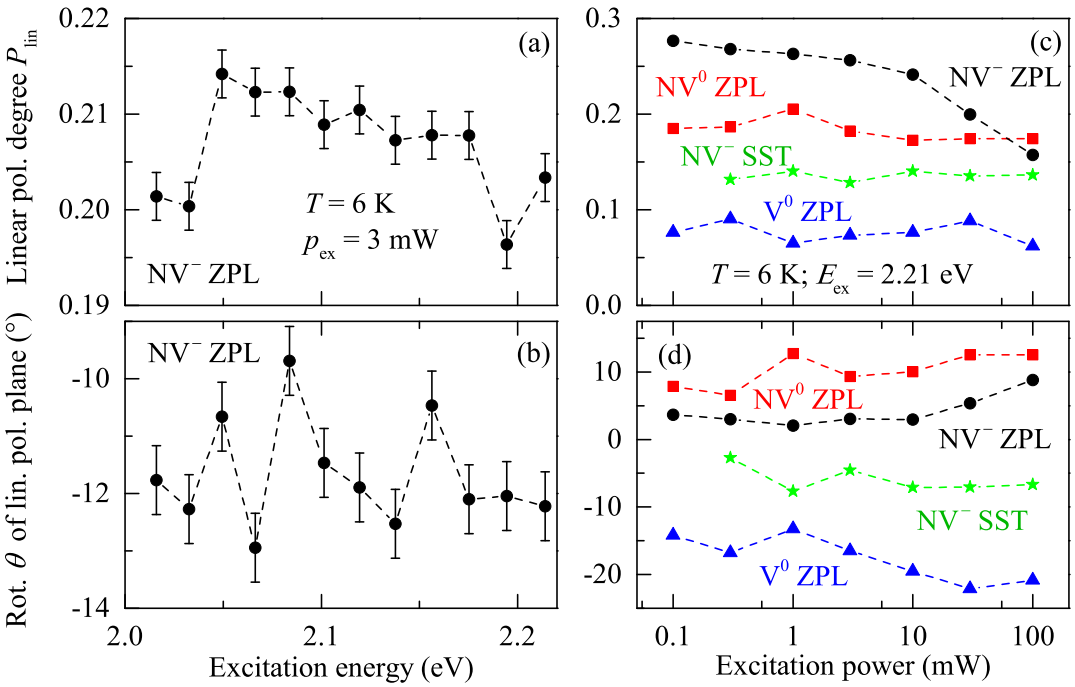

Figure 4-6: Dependence of the (a) linear polarization degree P_{lin} and (b) rotation θ of polarization plane of the NV^- ZPL on excitation energy. (c) P_{lin} and (d) θ of the NV^- ZPL (black dots), NV^0 ZPL (red squares), V^0 main ZPL (blue triangles), and the singlet state transition of the NV^- center (green stars) as a function of the excitation power; the optical axis is oriented along the (001) direction. Dotted lines are guides to the eye. If not shown, the experimental error does not exceed the symbol size.

excitation energy is of minor relevance in the region of highest absorption.[42] Even at quasi-resonant excitation with 2.01 eV an enhancement of the linear polarization is not observed. One may claim that resonant excitation would lead to an increase in P_{lin} due to a reduction in the probability of angular momentum changing relaxation processes between excited states, which shall however not be the case for excitation energies above 2.01 eV. Also, like P_{lin}, θ of the NV^- ZPL does not depend on the excitation energy. As one can see in Fig. 4-6 (a), θ has a constant value of about $(11 \pm 2)°$.

In contrast to the latter, the power of the exciting laser plays a crucial role for the NV^- polarization. In Fig. 4-6 (c) the power dependence of P_{lin} of the NV^- ZPL is depicted (black dots). For a low laser power, P_{lin} stays constant at a value of 0.27, but when the power increases above about 3 mW, it decreases down to 0.16 at 30 mW. Note that this is not the case for the P_{lin} of the NV^0 (red squares) or V^0 (blue triangles) ZPLs. In addition, the singlet state transition (SST)[50] of the NV^- center at 1.186 eV (green stars) remains stable as well.

The decrease of P_{lin} might be due to an increase in the local sample temperature, which is unavoidable at high power excitation. The decrease of P_{lin} at high powers

is comparable to the decrease at temperatures of about 10 K, compare Fig. 4-5 (a). However, at high excitation powers an increase in θ is observed only for the NV^- ZPL, see Fig. 4-6 (d), whereas an increase in θ is not observed for temperatures below 50 K. Since it can be assumed that the temperature increase due to high power excitation is far below such values, the increase in θ with rising power cannot be explained by heating effects only. A possible explanation would be a change in the refractive indices of right- and left-circularly polarized components of the ZPL emission, which is induced by the high power of the exciting laser.

4.4 Magnetic field dependence of the linear polarization

Besides the crystallographic properties, the polarization characteristics of the defect center ZPLs may also be influenced by the coupling of an external magnetic field with the angular momenta of the vacancy center electrons. In order to investigate this influence, polarization measurements at high magnetic fields up to 10 T were executed. Again the focus of this section lies on the polarization of the NV^- ZPL only and the P_{lin} will be discussed firstly. The angular dependence of P_{lin} shows similar 90° periodicity at magnetic fields of 0, 3, 6 and 9 T, as depicted in Fig. 4-7 (a) for the optical axis oriented along the (001) direction. The amplitude of the oscillation does not vary significantly with the strength of the applied magnetic field. This is most likely due to the fact that the linearly polarized excited states involved in the emission process of the ZPL, which have spin projection $m_S = 0$, differ only in their orbital angular momentum projection. Because of the small effective orbital g-factor (about 0.16), compare Sec. 3.1, the Zeeman splitting is rather small. Hence, strong changes in the population of the excited states cannot be created with magnetic field up to 9 T.

However, when looking at the angular anisotropy of P_{lin}, a phase shift can be seen. At zero magnetic field, P_{lin} hits its maximum at about $\phi = 45^\circ$, but at 9 T the maximum is shifted to about $\phi = 11^\circ$. This phase shift $\alpha(B)$ is shown in Fig. 4-8 (a) as a function of the applied magnetic field. Apparently, the phase shift increases with rising magnetic field. In order to mathematically describe the anisotropy in the presence of an external magnetic field, Eq. (4.6) must be modified in the following way:

$$P_{\mathrm{lin}}(\phi) = A\cos[4\phi + \phi_0 + \alpha(B)] + d \quad . \tag{4.9}$$

This equation is used to fit the data shown Fig. 4-7 (a).

The phase could result from the magnetic torque of the external field, acting on the magnetic moments of the NV^- center electrons.[82, 83, 84] As a result, they tend to align in such a way that the total magnetic energy is minimized. Such a rotation of the magnetic moments would in turn lead to a rotation of the angular dependence of the NV^- ZPL P_{lin}, since the polarization plane of the ZPL emission is perpendicular to the dipole orientation. An alternative explanation is that the observed phase shift occurs due to a mixing of states with different magnetic moments under the application of a magnetic field, which is specifically oriented with respect to the NV^- center symmetry axes.

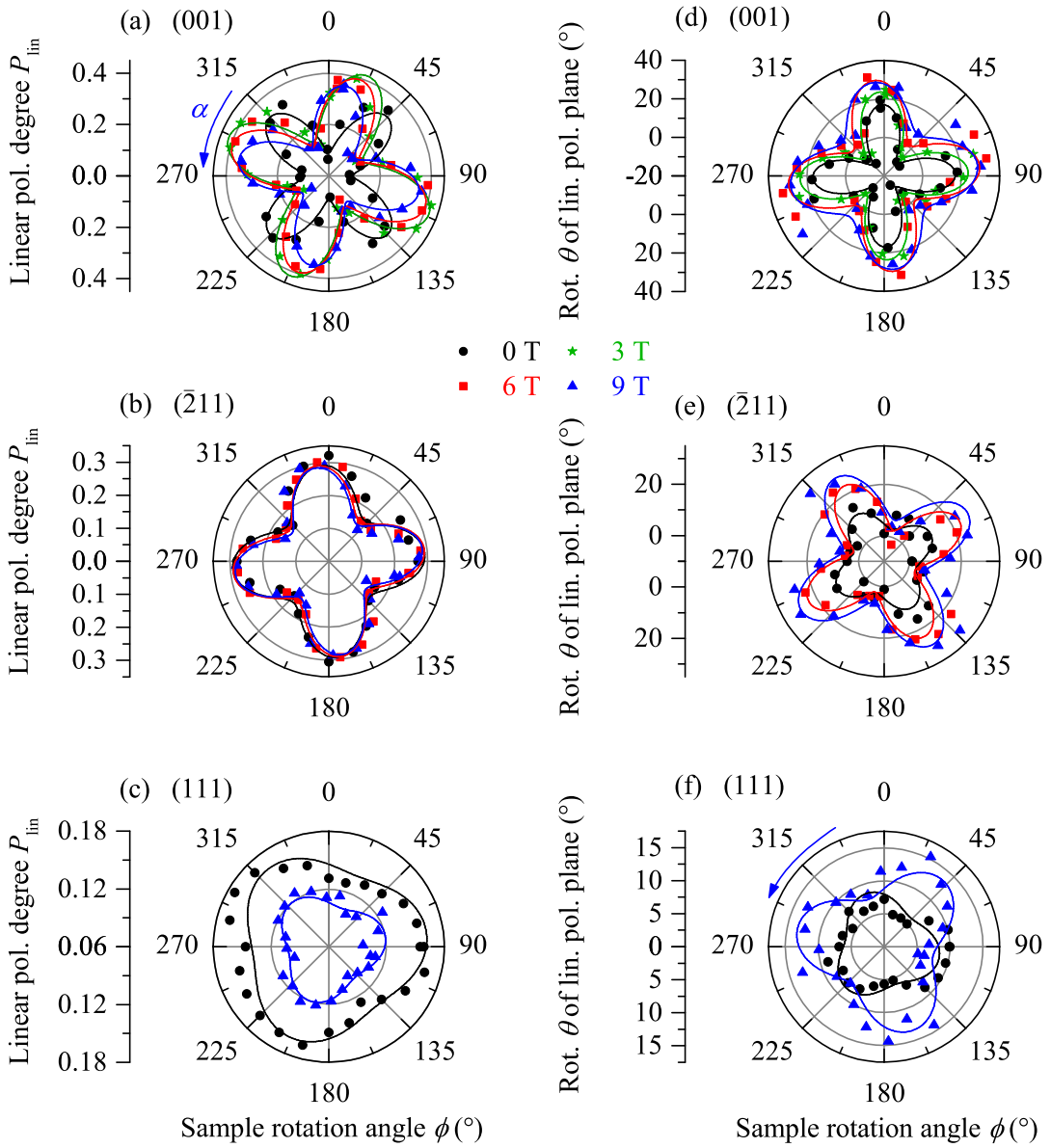

Figure 4-7: Linear polarization degree P_{lin} and rotation of polarization plane θ of NV^- ZPL along (a,d) the (001), (b,e) the $(\bar{2}11)$ and (c,f) the (111) direction as functions of the sample rotation angle ϕ at a magnetic field of $B = 0$ (black dots), 3 (green stars), 6 (red squares), and 9 T (blue triangles). The curves are fits based on Eq. (4.9) and (4.8), or, in case of the (111) direction a function $\propto \sin(3\phi)$. $T = 6$ K, $E_{\mathrm{ex}} = 2.21$ eV, $p_{\mathrm{ex}} = 10$ mW (for the (001) direction), 5 mW (for the $(\bar{2}11)$ direction), and 3 mW (for the (111) direction). The experimental error does not exceed the symbol size.

However, this phase shift of the P_{lin} of the NV^- ZPL can only be seen in the (001) direction. As depicted in Fig. 4-7 (b) there is no significant phase shift in the $(\bar{2}11)$ direction. Here the angular dependence looks almost the same regardless of the magnetic field. Additionally, no variation of the P_{lin} amplitude can be seen. In Fig. 4-7 (c) the angle dependence of P_{lin} along the (111) direction is shown. Equal to the $(\bar{2}11)$ direction, no phase shift of P_{lin} is seen with rising magnetic field, but a small increase of about 0.03 from 0 to 9 T can be observed in this geometry. Note that this increase is in the order of the experimental error for the (001) and $(\bar{2}11)$ direction, and therefore one cannot certainly conclude that such an increase is absent in these directions.

In contrast to the angular dependence of P_{lin}, the polarization rotation θ, illustrated in Fig. 4-7 (d) for the optical axis oriented along the (001) direction, shows no significant phase shift with rising magnetic field, but the total value of the 90° periodic oscillation increases drastically. At zero magnetic field θ varies between $-14°$ and $19°$, whereas at 9 T the variation lies between $2°$ and $32°$. In Fig. 4-8 (b) the dependence of θ on the magnetic field is shown for (001) direction (red dots) at $T = 6$ K. Note that the sample rotation angle ϕ was set to a value of maximal linear polarization degree. It becomes apparent that θ increases linearly with rising magnetic field. To describe the anisotropic behavior of $\theta(\phi)$, Eq. (4.8) must be extended with a variable offset via

$$e = e_0 + e(B) \cdot B \quad . \tag{4.10}$$

with $e_0 = (11.4 \pm 0.3)^\circ$ and $e(B) = (1.20 \pm 0.07))°/\mathrm{T}$ for (001) direction. It is worthwhile mentioning that the Faraday rotation of the cryostat windows, which would also cause an increase of θ with rising magnetic field, was separately measured and corrected in Eq. (4.10).

This linear increase of θ with the magnetic field can be observed for all studied directions. In Fig. 4-7 (e) the angular dependence of θ in $(\bar{2}11)$ direction is depicted. Equal to the (001) direction, no phase shift can be seen, but again θ increases with rising magnetic field. The slope can be evaluated to $e(B) = (0.79 \pm 0.04)°/\mathrm{T}$, compare Fig. 4-8 (b) (black filled squares). In addition, an increase of θ can be observed in the (111) direction too. The magnetic field dependence of the NV^- ZPL θ in (111) direction is presented in Fig. 4-7 (f) and with blue filled triangles in Fig. 4-8 (b), a fit according to Eq. (4.10) results in $e_0 = (-11.4 \pm 0.3)^\circ$ and $e(B) = (1.13 \pm 0.05)°/\mathrm{T}$.

Apparently, the increase of θ with rising magnetic field seems to be independent of the crystal orientation, since it is of a similar value in all three observed geometries. The arithmetic mean of this increase is $e(B) = (1.04 \pm 0.09)°/\mathrm{T}$. For the NV^0 ZPL (green stars) in (001) direction, a significant smaller increase of θ is observed with rising magnetic field. A fit according to Eq. (4.10) results in $e_0 = (10.4 \pm 0.4)^\circ$ and $e(B) = (0.44 \pm 0.08)°/\mathrm{T}$. Note that for the NV^- singlet state transition at 1.19 eV, P_{lin} is about 0.15 irrespective of the magnetic field strength, and θ rises with $e(B) = (2.0 \pm 0.4)°/\mathrm{T}$ measured along the (111) direction at $T = 6$ K (data not shown).

It is worthwhile mentioning that θ of the NV^- ZPL is not influenced significantly by temperature, as one can see in Fig. 4-5 (a). Even at room temperature the anisotropy of θ as well as its magnetic field dependence are more or less the same. However, the

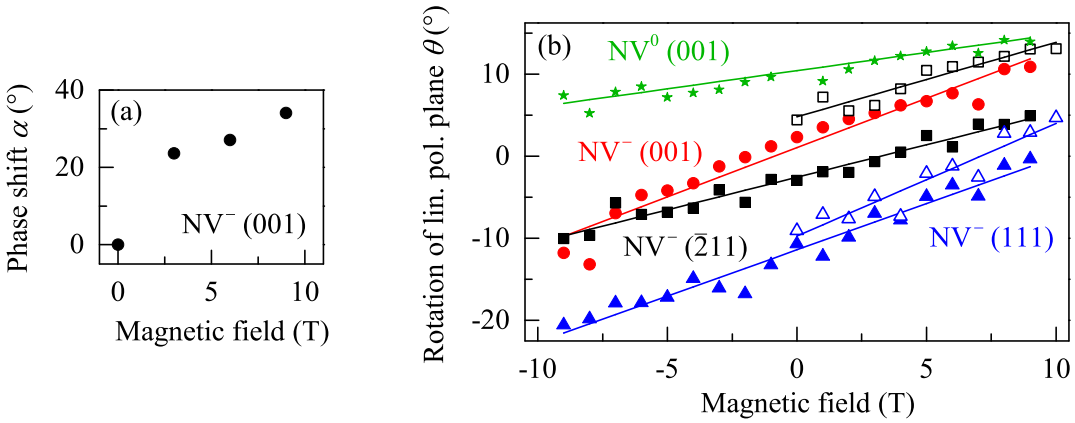

Figure 4-8: Magnetic field dependence of (a) phase shift α for NV^- ZPL polarization in (001) direction at $T = 6$ K, and (b) θ of the NV^- ZPL in (001) (red dots), ($\bar{2}11$) (black squares) and (111) direction (blue triangles) as well as of the NV^0 ZPL in (001) direction (green stars) at $T = 6$ K (filled symbols) and room temperature (open symbols). The solid lines are linear fits according to Eq.(4.10). $E_{ex} = 2.21$ eV, $p_{ex} = 10$ mW for (001) and ($\bar{2}11$) direction at room temperature, 3 mW for (111) and ($\bar{2}11$) direction at 6 K. If not shown, the experimental error does not exceed the symbol size.

error increases due to smaller ZPL intensity at high temperatures.[36] In Fig. 4-8 (b), the magnetic field dependence of θ is shown at room temperature for the (111) and ($\bar{2}11$) direction (open symbols). The total values for θ are a little larger but the slopes are within the margin of the error equal to the values determined at low temperatures. In the (111) direction one gets $e(B) = (1.4 \pm 0.2)°/\mathrm{T}$ and in the ($\bar{2}11$) direction $e(B) = (0.91 \pm 0.09)°/\mathrm{T}$ can be observed. Note that due to the low NV center concentration in BP, no room temperature measurements were performed in the (001) direction.

In addition to the increase of θ, a phase shift of θ can be identified at high magnetic fields, which is however only present in the (111) direction. As one can see in Fig. 4-7 (f) the angular shape of θ is rotated around about 60° when comparing the data obtained at $B = 0$ and 9 T. This phase shift is even bigger than the phase shift $\alpha(B)$ observed for the NV^- ZPL P_{lin} in the (001) direction, compare Fig. 4-8 (a).

The magnetic field dependences of P_{lin} and θ of the NV^- ZPL demonstrate that not only crystallographic properties are relevant for the polarization properties of the NV^- centers in diamond. The rotation of the linear polarization plane of the NV^- emission, with respect to the polarization of the exciting laser light, motivates the presence of magneto-optical rotation. Under the influence of an external magnetic field the NV center ensemble in diamond exhibits birefringence in its response to the linear polarized laser field. This is due to an asymmetry in the refractive indices for right- and left-circularly polarized light, caused by Zeeman splitting of the magnetic sublevels in the ground and excited states of the NV^- center.[95, 96]

The magneto-optical Faraday rotation θ_F, which indicates the rotation of the polarization plane of a light wave passing through an optically active medium

subjected to a magnetic field can be described by $\theta_F = V\eta B$, with the Verdet constant V and the thickness η of the medium. In a way, one can refer to the parameter e(B) as the Verdet constant. However, the results obtained in the (001), (111), and ($\bar{2}$11) direction do not depend on the thickness of the crystal, since it is quite likely that mostly the NV centers near the surface of the diamond crystal are excited and contribute to the ZPL emission. Therefore, the area of optically active NV^- centers can be assumed to be similar in both samples studied. Note that the magnetic field induced circular dichroism[97] is negligible, since the absorption of diamond is in the far ultra-violet spectral range due to the high band gab of about 5.48 eV.

An outlook on the influence of small magnetic fields in the order of 100 mT on the linear polarization of the NV^- ZPL can be found Chapter 7.

4.5 Conclusion

In summary, the zero phonon lines of the neutral and negatively charged nitrogen vacancy as well as the neutral single vacancy center are strongly linear polarized. Even at room temperature a linear polarization of 10 to 20 %, depending on the crystal orientation, is observed for the NV^- ZPL. This suggest that Jahn-Teller coupling is of minor relevance for ensembles of NV centers, resulting in an electron-phonon coupling between the NV centers and other defects modulated by long-wave acoustic phonons, which is just slightly depolarizing. The crystallographic properties of the NV centers cause distinct anisotropies in the linear polarization of the ZPL emission. These anisotropies not only characterize the NV center orientation and symmetry, but also offer the possibility of selectively addressing linearly polarized states by controlled change of the crystal orientation. In this context, the sign of the polarization plane rotation of the NV center ZPL emission is changed periodically, which indicates a switching between orthogonally linearly polarized transition dipoles. In addition, a magneto-optical rotation of the polarization plane of the NV center ZPL emission could be identified in the presence of high external magnetic fields. Remarkably, this magneto-optical rotation is isotropic, since it can be seen in all observed crystal directions, and of the same magnitude at low temperatures as well as at room temperature. Additionally, a phase shift of the angular dependence of the linear polarization degree of the NV^- ZPL can be seen when strong magnetic fields are applied. This could be a result of the magnetic torque of the applied field on the magnetic moments of the NV center electrons. Moreover, the temperature dependences of the NV^- ZPL characteristics indicate a direct phonon process between the excited states of the NV^- center. Furthermore, the rotation of the polarization plane of the NV^- ZPL emission is enhanced at high laser-excitation power in the absence of an external magnetic field. This might be due to an optically induced change in the refractive indices of the right- and left-circularly polarized components of the NV^- ZPL emission.

Chapter 5

Fano effect and effective recharging

In this chapter the interaction between the two charge states of the NV centers is investigated. PLE measurements were carried out in the energy range of the NV^0 and NV^- center ZPLs. By analyzing the distinct characteristics of the PL emitted by these centers, the origin of the interaction is determined. Firstly, the NV^- ZPL at resonant excitation of the NV^0 center is studied in Sec. 5.1. In this context, three samples with different concentrations of NV centers are taken into account in Sec. 5.1.1. In addition, the effects of excitation power and spot size (Sec. 5.1.2), as well as temperature (Sec. 5.1.3) and magnetic field (Sec. 5.1.4) on the coupling mechanism are investigated. After a short summary of the findings in Sec. 5.1.5, the focus is drawn on the NV^0 ZPL at resonant excitation of the NV^- center in Sec. 5.2. In this regard, the dynamics of the interaction between the two charge states are presented. Moreover, in Sec. 5.3, the V^0 ZPLs are observed under resonant excitation of the NV^0 center. In Sec. 5.4 two explanations for the observed interaction are discussed. Firstly, the role of NV center recharging in the emission process of the ZPL is considered in Sec. 5.4.1. It is followed by an introduction into the Fano effect, which can be identified in the ZPL of the NV centers, in Sec. 5.4.2. Finally, the findings of this chapter are concluded in Sec. 5.5. Note that this chapter covers content which is prepared to be published.[98]

5.1 NV^- ZPL under resonant excitation of NV^0 center

To probe the interaction between the differently charged states of the NV center, the NV^- ZPL is observed under variation of the excitation energy. This experimental principle can be seen in Fig. 5-1 (a). Here, the spectra of both, the NV^- and NV^0 ZPL in BP, are depicted. The detection range, which includes the NV^- ZPL, is shown in blue while energy of the exciting laser is marked in green. The aim is to investigate how the NV^- ZPL changes when the excitation energy is in resonance with the NV^0 ZPL energy. Therefore, the NV^- ZPL is fitted with a Gaussian function in order to determine the intensity, width, and peak energy. The dependence of these parameters on the excitation energy E_{ex} is subsequently analyzed. The setup of such a PLE experiment is presented in Sec. 2.1. In Fig. 5-2 (a) the normalized intensity I_{ZPL} of the NV^- ZPL is shown

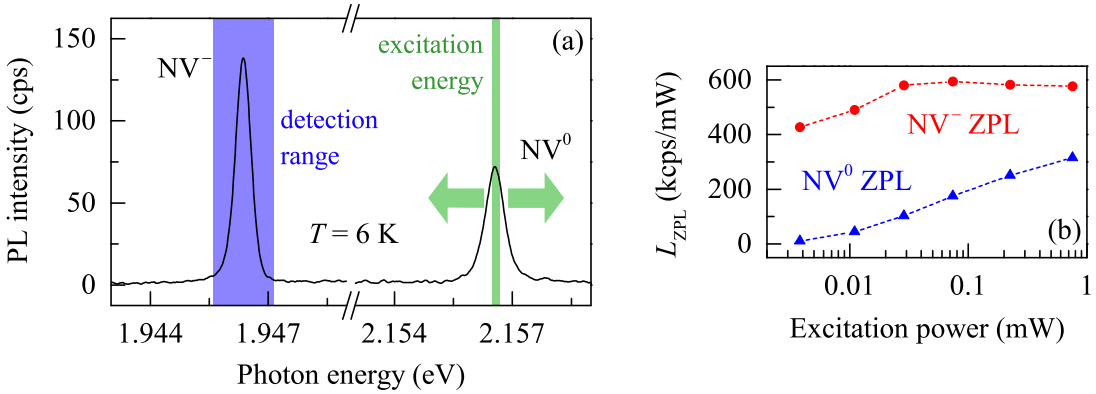

Figure 5-1: (a) PL spectrum of diamond sample BP containing NV^0 and NV^- centers. For probing the coupling between the differently charged states the NV^0 center is resonantly excited at about 2.156 eV (green shaded region), while the ZPL of the NV^- center is detected at about 1.946 eV (blue shaded region); $p_{ex} = 10$ mW, $E_{ex} = 2.33$ eV. (b) Luminescence efficiency L_{ZPL} of the NV^0 (blue triangles) and NV^- ZPL (red dots) in Ryab as a function of the excitation power; $T = 295$ K, $E_{ex} = 2.33$ eV. Dashed lines are guides to the eye.

as a function of the excitation energy. Note that the depicted intensity is normalized to the value of I_{ZPL} at non-resonant excitation; that means the intensity shows the amplification due to resonant excitation. When the excitation energy equals the NV^0 ZPL energy of about 2.156 eV, the NV^- ZPL drastically increases. This resonance can be fitted well with a Lorentzian function according to

$$I_{ZPL}(E_{ex}) = I_0 + \left(2 \cdot \frac{A_L}{\pi}\right) \cdot \frac{w_L}{4 \cdot (E_{ex} - E_{res})^2 + w_L^2}, \tag{5.1}$$

with $I_0 = 1.0 \pm 0.1$, amplitude $A_L = (12.2 \pm 0.4)$ meV, resonance width $w_L = (0.59 \pm 0.02)$ meV, and resonance energy $E_{res} = (2.15643 \pm 0.00001)$ eV. For characterizing the resonance, however, only two parameters are of significant importance: the resonance width w_L and the ZPL intensity amplification $H_L = 2 \cdot A_L/(\pi \cdot w_L) + I_0$. The fitting parameters result in an amplification $H_L = 14.1 \pm 0.4$ of the NV^- ZPL at resonant excitation of the NV^0. A descriptive interpretation of these two parameters can be seen in Fig. 5-2 (a) indicated by blue bars. It is worthwhile mentioning that this resonance can be observed at almost the exact same energy of the NV^0 ZPL. Moreover, the width of the resonance is comparable to the linewidth of the NV^0 ZPL, too. A Lorentzian fit according to Eq. (5.1) to the spectrum of the NV^0 ZPL shown in Fig. 5-1 (a) yields $E_{res} = (2.15656 \pm 0.00001)$ eV and $w_L = (0.504 \pm 0.005)$ meV. The energies only differ by about 0.13 meV, which is far less than the width of the resonance and the step width of the measurement, which was about 0.4 meV.

In addition to the distinct intensity increase at resonant excitation of the NV^0 center, a decrease of the NV^- ZPL width can be seen. In Fig. 5-2 (b) the FWHM of the NV^- ZPL is presented as a function of the excitation energy. At the resonance, the FWHM decreases by about 23 %.

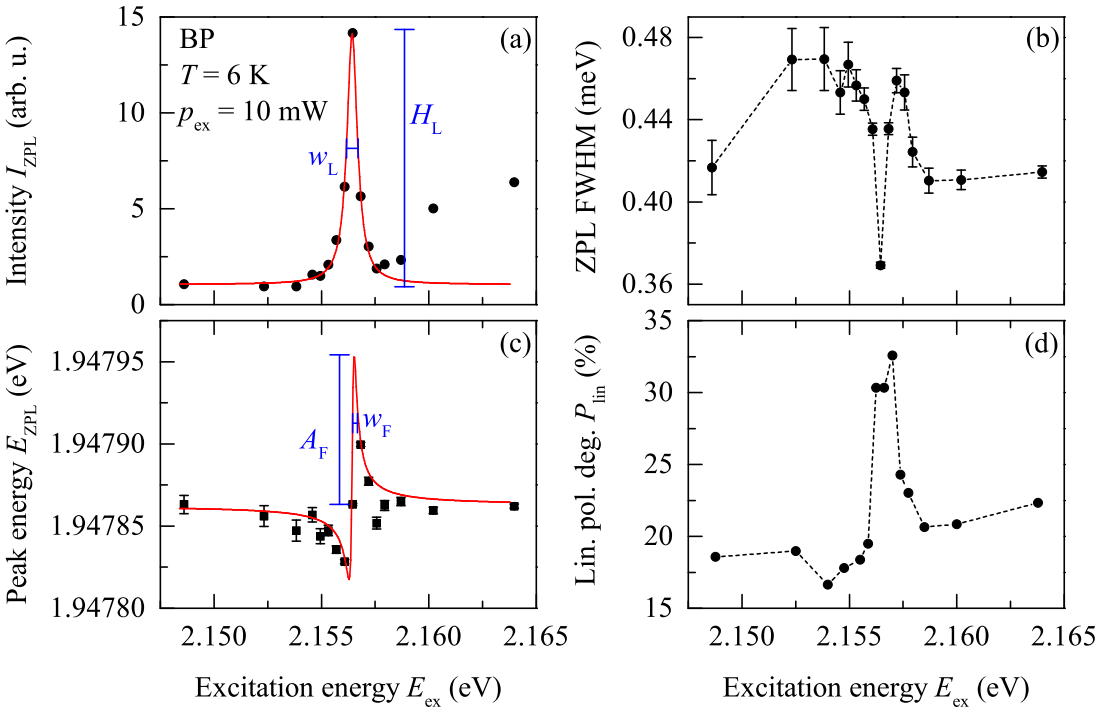

Figure 5-2: Characteristics of the NV^- ZPL determined by Gaussian fits (black dots) at resonant excitation of the NV^0 center as functions of the excitation energy E_{ex}. (a) ZPL intensity I_{ZPL} normalized, to show the relative increase of the ZPL, the red solid line is a Lorentzian fit function according to Eq. (5.1), the fitting parameters w_L and H_L are shown in blue; (b) ZPL FWHM; (c) ZPL peak energy E_{ZPL}, the red solid line is a Fano resonance fit function according to Eq. (5.2), the fitting parameters A_F and w_F are shown in blue. (d) Linear polarization degree P_{lin} of the NV^- ZPL (black dots), calculated by Eq. (4.1), at resonant excitation of the NV^0 center as functions of the excitation energy E_{ex}. Dashed lines are guides to the eye. Unless shown otherwise, the error does not exceed the symbol size.

Moreover, there is a resonance of the NV^- ZPL peak energy E_{ZPL}, as one can see in Fig. 5-2 (b). The energy shift at resonant excitation of the NV^0 center can be fitted by a Fano resonance[99] function

$$E_{ZPL}(E_{ex}) = A_F \cdot \frac{\left(q_F \cdot \frac{1}{2}w_F + E_{ex} - E_{res}\right)^2}{\left(\frac{1}{2}w_F\right)^2 + (E_{ex} - E_{res})^2} + E_0 \quad , \tag{5.2}$$

with amplitude $A_F = (92 \pm 3)$ μeV, Fano factor $q_F = 0.7 \pm 0.1$, resonance width $w_F = (230 \pm 30)$ μeV, resonance energy $E_{res} = (2.1564 \pm 0.0001)$ eV, and offset $E_0 = (1.947954 \pm 0.000001)$ eV. As a descriptive interpretation the parameters A_F and w_F are illustrated in Fig. 5-2 (c), indicated by blue bars. Note that in terms of accuracy the measured resonance energy for the ZPL peak energy is identical with the resonance energy observed for the ZPL intensity resonance, whereas the width w_F of the energy resonance is only half of the intensity resonance width w_L. However, when looking at

Fig. 5-2 (a) and (c) it becomes apparent that w_L and w_F cannot be compared directly. In contrast to the Lorentzian shape of the intensity resonance, the Fano resonance shows not one but two peaks, one pointing to higher and one to lower NV^- ZPL energies. Both peaks show a width associated with the parameter w_F. Hence, the total width of the resonance is better described by $2w_F$, and is therefore quite similar to the width w_L of the intensity resonance.

Furthermore, the polarization properties of the NV^- ZPL are analyzed. In Fig. 5-2 (d) the excitation energy dependence of P_{lin} according to Eq. (4.1) is depicted. At non resonant excitation P_{lin} is about (20 ± 2) %, but at resonant excitation of the NV^0 center, P_{lin} increases to a maximum of about 32 %. Taking the polarization of the exciting lasers into account, a high P_{lin} indicates that the ZPL is polarized along the same direction as the laser light.

5.1.1 Influence of high NV center concentration on the ZPL resonances

Before analyzing the power and temperature dependence of the resonances, it should be clarified if the resonances depend on the NV center concentration. The previous investigations were performed on BP, a sample with rather low concentration and a negligible amount of nitrogen impurities. The latter is important for probing an interaction between NV^0 and NV^- centers, since a high amount of nitrogen impurities results in a majority of NV centers with negative charge. Apparently, the fifth electron of the nitrogen atom adds to the amount of free electrons, which can be captured by the NV center, forming the negatively charged NV^- state. Therefore, a high amount of nitrogen leads to an n-doping of the diamond crystal. The small number of NV^0 centers in the n-doped samples limits the possibility of observing a resonance effect. Only at high power excitation the NV^0 ZPL becomes comparably intense to the NV^- ZPL. In Fig. 5-1 (b) the luminescence efficiency L of both NV^0 and NV^- ZPL is pictured as a function of the excitation power. Note that a microscope objective was used, and therefore the power density is much higher (about a factor of 10000) than in the previously discussed measurements. The luminescence efficiency of the ZPLs is defined by $L_{ZPL} = I_{ZPL}/p_{ex}$ and indicates how many NV centers are excited by a certain amount of photons and subsequently emit ZPLs. If the intensity of the ZPL rises linearly with the excitation power, L_{ZPL} would exhibit a horizontal line. This is more or less the case for the NV^- ZPL. However, for the NV^0 ZPL, L_{ZPL} shows a strong nonlinear power dependence. At low excitation powers of about 0.01 mW (300 $W\,cm^{-2}$), L_{ZPL} of the NV^0 ZPL is about one order of magnitude smaller than L_{ZPL} of the NV^- ZPL. At high excitation powers of about 0.75 mW (22.5 $kW\,cm^{-2}$), the difference between the luminescence efficiencies becomes smaller; L_{ZPL} of the NV^0 ZPL is about two times smaller, compared to the NV^- ZPL.

In the following section it will be shown that at excitation-power densities of about 1 $MW\,cm^{-2}$, which can be achieved by using a microscope objective (compare Sec. 2.2), the resonance can be observed in samples with high amounts of nitrogen impurities too. In Fig. 5-3 (a) the normalized intensity of the NV^- ZPL is illustrated as a function of

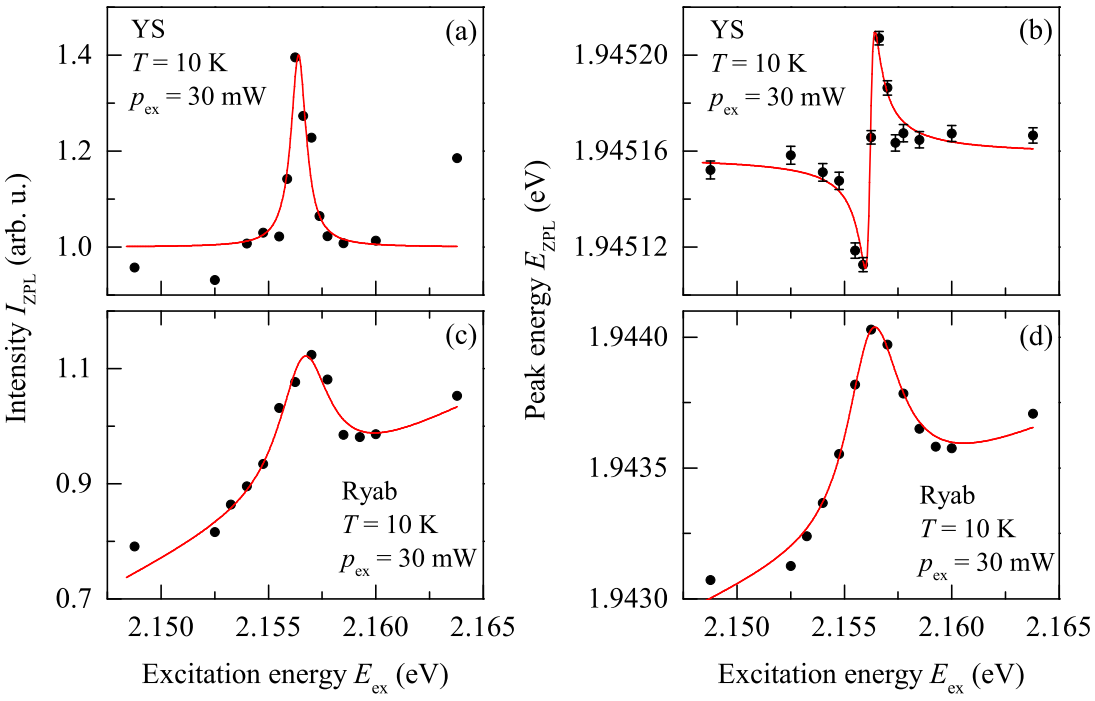

Figure 5-3: Characteristics of the NV^- ZPLs of two diamond samples with high NV center concentration determined by Gaussian fits (black dots) at resonant excitation of the NV^0 center as functions of the excitation energy E_{ex}. (a, c) ZPL intensity I_{ZPL} normalized, to show the relative increase of the ZPL. The red solid lines are Lorentzian fit functions according to Eq. (5.1). (b, d) ZPL peak energy E_{ZPL}, the red solid lines are Fano resonance fit functions according to Eq. (5.2). For Ryab, the fit function was modified by a linear term to compensate the background. Unless shown otherwise, the error does not exceed the symbol size.

the excitation energy for the sample YS with $\rho_{NV} = 2.9$ ppm. Similar to BP ($\rho_{NV} = 0.14$ ppm) an intensity increase at resonant excitation of the NV^0 center can be seen. In comparison to BP, the resonance is smaller, with $H_L = 1.4 \pm 0.1$ and wider, $w_L = (0.8 \pm 0.3)$ meV. The latter effect is due to the higher concentration of NV centers in YS, since ensemble effects lead to an inhomogeneous broadening of the ZPL lines. The former is most likely due to the reduced amount of NV^0 centers, caused by the n-doping due to the nitrogen impurities in this sample. Again, the observed width of the resonance is quite similar to the linewidth of the NV^0 ZPL, which can be determined to $w_L = (0.994 \pm 0.05)$ meV with a Lorentzian fit according to Eq. (5.1).

When looking at the peak energy of the NV^- ZPL, which is depicted in Fig. 5-3 (b), a Fano resonance at resonant excitation of the NV^0 center can be seen again. In comparison to the previous measurement on BP, the amplitude of the energy resonance $A_F = (52 \pm 3)$ μeV is just a little bit smaller, whereas the Fano factor $q_F = 0.95 \pm 0.05$ indicates a more pronounced resonance. The resonance width $w_F = (450 \pm 80)$ μeV is about twice as broad compared to BP, which again might simply be an ensemble effect.

In addition to that, Ryab, a sample with even higher NV center density of $\rho_{\mathrm{NV}} = 3.8$ ppm, is investigated. The normalized intensity of the NV^- ZPL as a function of the excitation energy is shown in Fig. 5-3 (c). One can clearly see that the resonance at 2.156 eV is way broader compared to the samples with lower concentration, while the amplification is significantly lower. Using a Lorentzian fit function according to Eq. (5.1) with a linearly rising background one gets $H_{\mathrm{L}} = 1.23 \pm 0.02$ and $w_{\mathrm{L}} = (2.9 \pm 0.6)$ meV. The latter is quite comparable to the linewidths one observes for the NV^0 and NV^- ZPL in this sample. Lorentzian fits according to Eq. (5.1) result in $w_{\mathrm{L}} = (1.44 \pm 0.01)$ meV for the NV^0 and $w_{\mathrm{L}} = (3.99 \pm 0.04)$ meV for the NV^- ZPL.

When looking at the NV^- ZPL energy resonance at resonant excitation of the NV^0 center, which is presented in Fig. 5-3 (d), a broadening can be seen and a strong increase of the resonance amplitude is also observable. A Fano resonance fit function according to Eq. (5.2) with a linearly increasing background gives $A_{\mathrm{F}} = (730 \pm 60)$ μeV, which is about one order of magnitude larger compared to the other two samples, and $q_{\mathrm{F}} = 0.1 \pm 0.05$. This indicates that the Fano effect is rather small, since the line shape is almost Lorentzian (limiting case of Fano resonance for $q_{\mathrm{F}} = 0$) and $w_{\mathrm{F}} = (3.0 \pm 0.4)$ meV.

Considering that the excitation power density for samples with high NV center concentration is several orders of magnitude higher compared to the low concentration sample BP, it makes sense to probe the power dependence of the resonances before comparing the results for the samples with different NV center concentration. Since a heating of the sample is inevitable when exciting with such high excitation power densities, a detailed analysis of the temperature dependence of the observed resonances follows later on in Sec. 5.1.3. It must be noted that the actual temperature of the sample in the focus of the excitation laser can only be estimated. Since, the sample was glued on a cold finger of a flow cryostat, compare Sec. 2.2, the temperature was most likely about 6 to 10 K. Due to the high thermal conductivity of the diamond crystal, heating due to the high power laser excitation can be expected to be effectively compensated by cooling the sample. Since, no thermal broadening of the ZPL linewidths was observed, the temperature increase induced by the laser can be estimated to be in the order of a few K.

5.1.2 Excitation power dependence of the ZPL resonances

In the following section, the focus will lie on the excitation power dependence of the observed resonances in the sample BP. In Fig. 5-4 (a) the parameters of the NV^- ZPL, defined by a Lorentzian fit according to Eq. (5.1), are depicted as a function of the excitation power. The intensity amplification H_{L} (black dots) rises with increasing excitation power. At small powers of about 0.1 to 1 mW, the amplification is constant at a value of about $H_{\mathrm{L}} = 8 \pm 1$, but when the power exceeds 3 mW, H_{L} rises until it reaches its maximum of 23 ± 1 at about 30 to 100 mW. The resonance width of the ZPL intensity w_{L} (red triangles) decreases with rising excitation power. The general trend is that w_{L} deceases when H_{L} increases. At low excitation power one gets $w_{\mathrm{L}} = (1.4 \pm 0.3)$ meV, while at higher powers the width is about half as wide. However, at maximal excitation power of 100 mW the width increases again to $w_{\mathrm{L}} = (1.1 \pm 0.1)$ meV. Together with

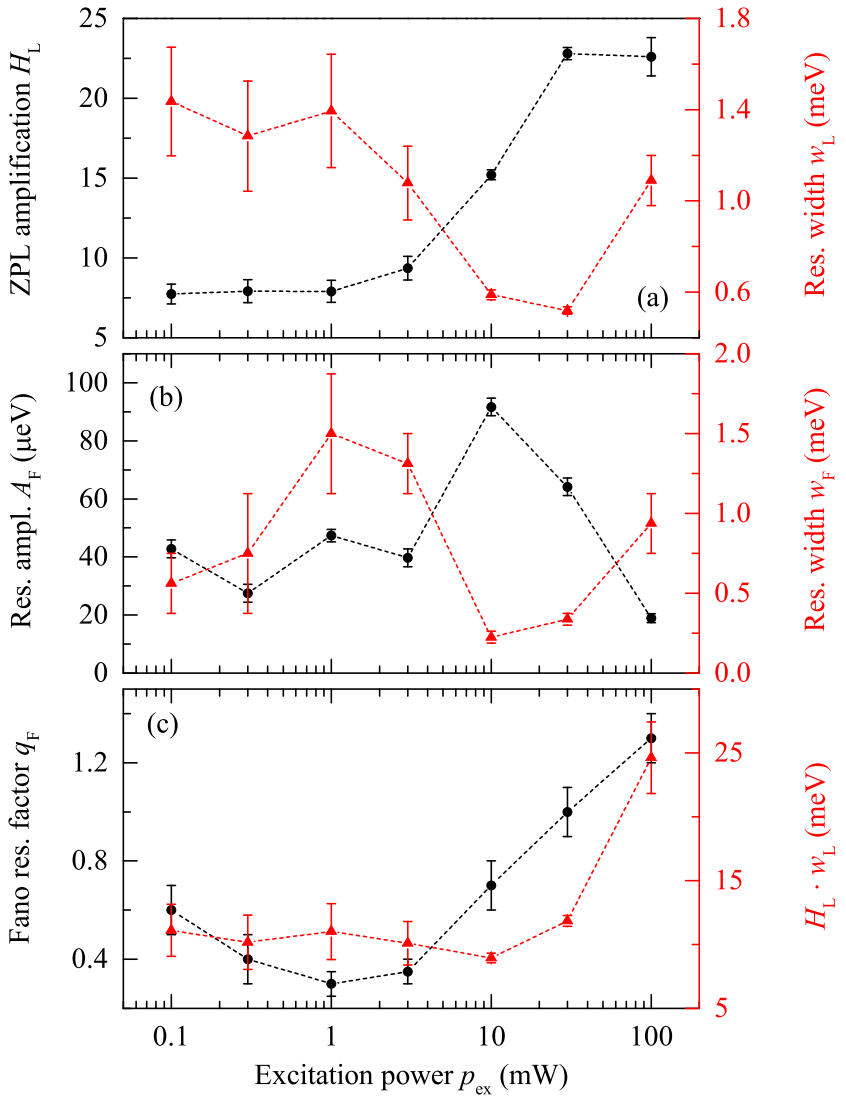

Figure 5-4: Characteristics of the NV^- ZPL resonance (compare Fig. 5-1) in BP as a functions of the excitation power p_{ex}: (a) ZPL intensity amplification H_L (black dots) and resonance width w_L (red triangles) estimated by Lorentzian fits according to Eq. (5.1); (b) amplitude A_F (black dots) and width w_F (red triangles) of the energy resonance of the ZPL estimated by Fano resonance fits according to Eq. (5.2); (c) Fano factor q_F (black dots) of the energy resonance and spectrally integrated ZPL amplification $H_L \cdot w_L$ (red triangles); $T = 6$ K. Dashed lines are guides to the eye.

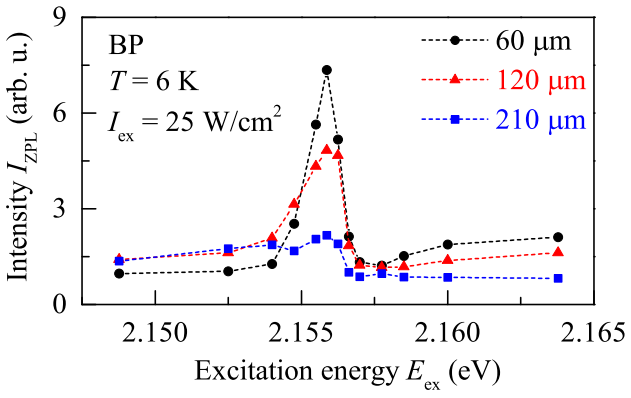

Figure 5-5: Intensity I_{ZPL} of the NV$^-$ ZPL as function of the excitation energy E_{ex} for different spot diameters of the exciting laser. The intensity is normalized, to show the relative increase of the ZPL. Note that only the PL emitted from the center of the sample was detected. The error does not exceed the symbol size. Dashed lines are guides to the eye.

the fact that H_{L} does not increase from 30 to 100 mW, this might be a sign for a saturation effect at high excitation powers. However, when one takes a look at the spectrally integrated NV$^-$ ZPL amplification $H_{\mathrm{L}} \cdot w_{\mathrm{L}}$ (red triangles), which is shown in Fig. 5-4 (c), no saturation effect is measured. The amplification is almost constant at (10 ± 1) meV over the whole power range, but at 100 mW excitation power a strong increase to about 25 meV can be observed.

Next, the power dependence of the NV$^-$ ZPL peak energy resonance will be analyzed. In Fig. 5-4 (b) the parameters of the Fano resonance according to Eq. (5.2) are illustrated. The resonance amplitude A_{F} (black dots) is about constant at excitation powers below 3 mW. The maximum $A_{\mathrm{F}} = (92 \pm 3)$ μeV can be observed at 10 mW, while the minimum $A_{\mathrm{F}} = (19 \pm 2)$ μeV is seen at 100 mW. Especially at low powers, the resonance width w_{L} (red triangles) has a rather high error rate; its maximum $w_{\mathrm{L}} = (1.5 \pm 0.4)$ eV can be found at excitation power of 1 mW, while the minimum $w_{\mathrm{L}} = (0.23 \pm 0.04)$ eV is located at 10 mW. In contrast to these two parameters, the Fano parameter q_{L} (black dots) shows a much more distinct power dependence, as one can see in Fig. 5-4 (c). At minimal excitation power of 0.1 mW one measures $q_{\mathrm{L}} = 0.6 \pm 0.1$. With rising power the Fano resonance gets less pronounced; q_{L} drops to about 0.30 ± 0.05 at 1 mW. With increasing power, however, the Fano parameter rises to $q_{\mathrm{L}} = 1.3 \pm 0.1$ at maximal excitation power of 100 mW.

When discussing the effect of the excitation power, also the spot size of the exciting laser should be considered. In Fig. 5-5, the NV$^-$ ZPL resonance is depicted for three spot sizes. Note that the power density $I_{\mathrm{ex}} = (25 \pm 5)$ W/cm^2 is equal in all measurements. With increasing spot size the resonance becomes weaker. When exciting with a spot 60 μm in diameter (black dots), the ZPL amplification is about $H_{\mathrm{L}} = 7.3$, with a spot 120 μm in diameter (red triangles), one gets $H_{\mathrm{L}} = 4.8$, and at 210 μm diameter (blue squares) the resonance almost vanishes: $H_{\mathrm{L}} = 2.2$. In addition, one can clearly see that

the NV^- ZPL intensity rises for big spot sizes, when exciting with energies below the NV^0 ZPL energy, whereas when exciting with energies above the NV^0 ZPL energy, the intensity decreases for big spot sizes compared to small ones.

5.1.3 Temperature dependence of the ZPL resonances

In order to understand the origin of the observed resonances, their temperature dependence will be discussed. Again, the NV^- ZPL intensity resonance will be considered at first and thereafter the energy resonance. In Fig. 5-6 (a) the temperature dependences of the parameters H_L (black dots) and w_L (red triangles) are depicted as functions of the sample temperature. For $T = 1.8$ K one gets an NV^- ZPL intensity amplification $H_L = 5.2 \pm 0.3$, but when the temperature rises, H_L rapidly increases to a maximal value of about 30 ± 2 at 15 K. However, when the temperature rises above 20 K the amplification H_L decreases again to a value of 10.0 ± 0.2 at 70 K. The linewidth of the resonance is more or less constant at $w_L = (0.9 \pm 0.2)$ meV at low temperatures. However, when the temperature exceeds 25 K, it increases to about $w_L = (3.8 \pm 0.2)$ meV at 70 K. A fit with a power function according to

$$w(T) = w_A \cdot T^x + w_0 \quad , \tag{5.3}$$

with amplitude w_A and offset w_0, shows a temperature dependence proportional to $T^{2.2\pm0.2}$. This is within the level of inaccuracy comparable to the temperature dependences of the NV^0 and NV^- ZPL linewidths, which are proportional to $T^{3.0\pm0.4}$ and $T^{1.9\pm0.1}$ respectively.[80] Again, the spectrally integrated amplification $H_L \cdot w_L$ (red triangles), which is depicted in Fig. 5-6 (c) will be taken into consideration too. It becomes apparent that the integrated amplification rises with the temperature. At 1.8 K one can observe the minimal amplification of (4.2 ± 0.6) meV. With rising temperature $H_L \cdot w_L$ increases strongly until about 15 K, then the curve flattens. At 70 K one gets the maximal amplification of (38 ± 2) meV.

The temperature dependence of the NV^- ZPL energy resonance is shown in Fig. 5-6 (b). The amplitude of the resonance A_F (black dots) is again rather small at low temperatures, but increases when the temperature is slightly increased. At 1.8 K one only gets $A_F = (28 \pm 3)$ μeV, but at 10 K the maximum of $A_F = (138 \pm 6)$ μeV can be observed. With the temperature rising further, the amplitude decreases to about $A_F = (11.0 \pm 0.6)$ μeV at 70 K. Similar to the width of the NV^- ZPL intensity resonance, the width of the energy resonance w_F (red triangles) increases with rising temperature. At low temperatures $w_F = (0.6 \pm 0.2)$ meV is observed, whereas the maximal value of $w_F = (3.0 \pm 0.4)$ meV is seen at 70 K. A fit with a power function according to Eq. (5.3) shows a $T^{2.3\pm0.1}$ dependence, which is in good agreement with the $T^{2.2\pm0.2}$ dependence observed for the NV^- ZPL intensity resonance width w_L.

However, the Fano resonance factor q_F does not exhibit a clear temperature dependence. As one can see in Fig. 5-6 (c), it is constant within the measured temperature range at a value of about $q_F = 0.8 \pm 0.2$, when discounting the value at 1.8 K.

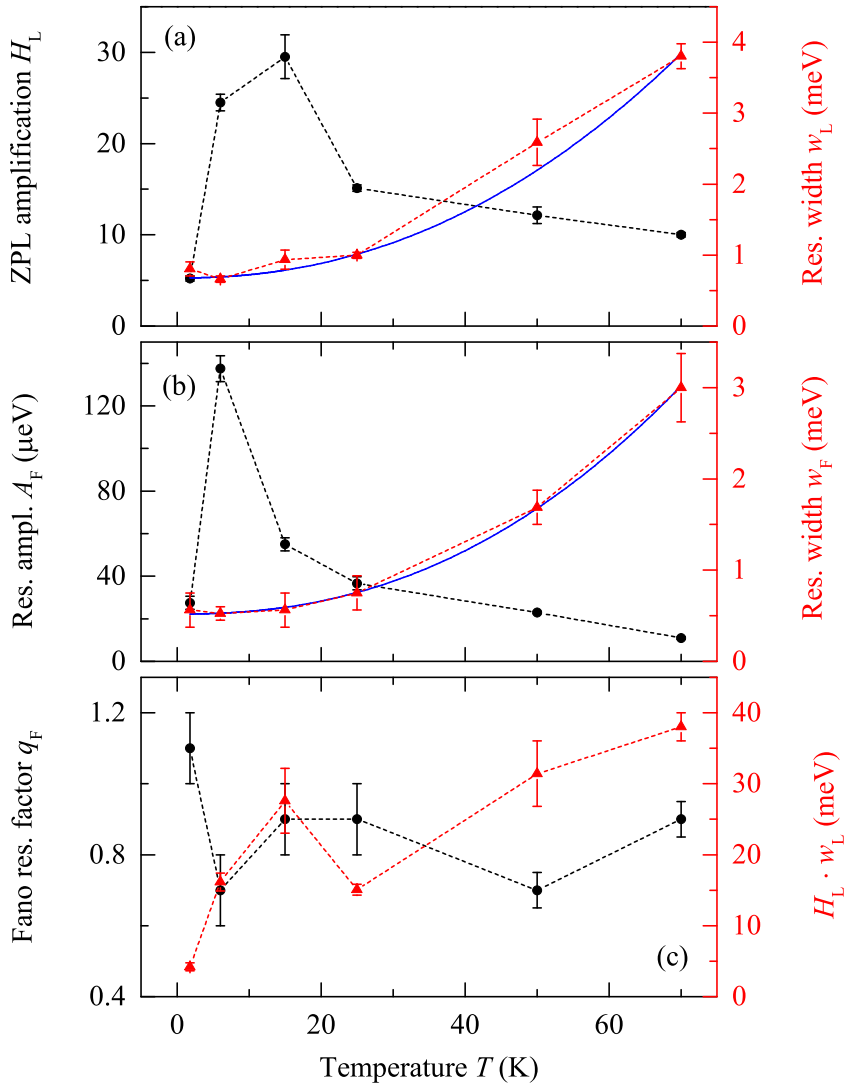

Figure 5-6: Characteristics of the NV^- ZPL resonance (compare Fig. 5-1) in BP as functions of the sample temperature T: (a) ZPL intensity amplification H_L (black dots) and resonance width w_L (red triangles) estimated by Lorentzian fits according to Eq. (5.1); (b) amplitude A_F (black dots) and width w_F (red triangles) of the energy resonance of the ZPL estimated by Fano resonance fits according to Eq. (5.2); (c) Fano factor q_F (black dots) of the energy resonance and spectrally integrated ZPL amplification $H_L \cdot w_L$ (red triangles); $p_{ex} = 10$ mW. The blue solid lines are power function fits according to Eq. (5.3). Dashed lines are guides to the eye.

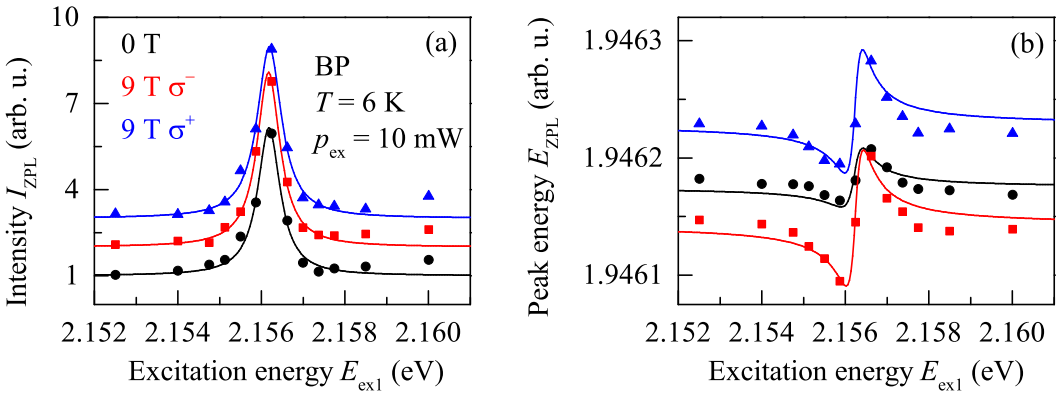

Figure 5-7: Characteristics of the NV^- ZPL estimated by Gaussian fits at resonant excitation of the NV^0 center as functions of the excitation energy E_{ex} at a magnetic field $B = 0$ T (black dots) and $B = 9$ T for right (blue triangles) and left circularly polarized light (red squares): (a) ZPL intensity I_{ZPL} normalized, to show the relative increase of the ZPL; the solid lines are Lorentzian fit functions according to Eq. (5.1); (b) ZPL peak energy E_{ZPL}, the solid lines are Fano resonance fit functions according to Eq. (5.2). The error does not exceed the symbol size.

5.1.4 Magnetic field dependence of the ZPL resonances

For further investigations, PLE experiments at magnetic fields were carried out. Since the ZPL is effected by Zeeman splitting, the PL was detected in both circular polarizations, σ^+ and σ^-. In Fig. 5-7 (a) the normalized intensity of the NV^- ZPL is depicted as a function of the excitation energy at an external magnetic field of $B = 0$ (black dots) and 9 T. Note that for reasons of clarity, the curves are staggered. There is not a significant difference between the intensity resonances for σ^+ (blue triangles) and σ^- (red squares) polarized ZPLs at 9 T. For σ^+ polarization, one can observe an amplification of $H_L = 7.0 \pm 0.3$ and for σ^- one gets $H_L = 7.1 \pm 0.3$. The values are a little bit higher, compared to the amplification of $H_L = 6.2 \pm 0.4$ one obtains at 0 T. However, in terms of accuracy a pronounced dependence of the ZPL intensity resonance on the magnetic field cannot be identified.

In contrast to that, the NV^- ZPL energy resonance, which is pictured in Fig. 5-7 (b), significantly depends on the external magnetic field. While the ZPL peak energy E_{ZPL} in σ^+ polarization (blue triangles) is shifted to higher energies, one observes a shift to lower energies in σ^- polarization (red squares). This energy shift is about $\Delta E_Z = (86 \pm 3)$ μeV and corresponds to a Zeeman splitting with a g-factor of $g_L = 0.16 \pm 0.01$. This result is well in line with previous magneto-PL measurements performed at this sample, compare Sec. 3.1.2. In addition to that, an increase of the resonance amplitude can be seen. At $B = 0$ T the resonance amplitude is about $A_F = 34 \pm 2$ μeV, whereas at 9 T one gets $A_F = 64 \pm 3$ μeV.

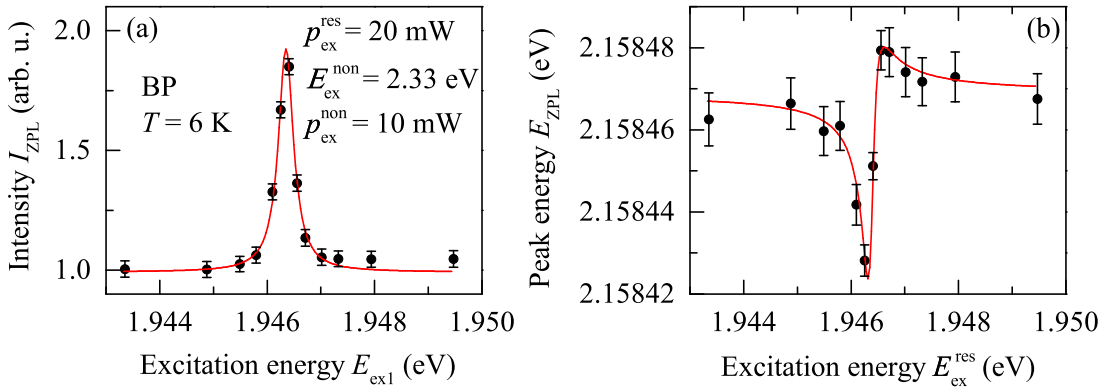

Figure 5-8: Characteristics of the NV^0 ZPL estimated by Gaussian fits (black dots) at resonant excitation of the NV^- center as functions of the excitation energy E_{ex}^{res}: (a) ZPL intensity I_{ZPL} normalized, to show the relative increase of the ZPL; the red solid line is a Lorentzian fit function according to Eq. (5.1); (b) ZPL peak energy E_{ZPL}; the red solid line is a Fano resonance fit function according to Eq. (5.2).

5.1.5 Intermediate summary

Taking the power and temperature dependences into account, it can be concluded that there are two resonances at resonant excitation of the NV^0 center at 2.156 eV; namely a resonance of the NV^- ZPL intensity and energy. The widths of these resonances are, within the limits of accuracy, equal to the linewidth of the NV^0 ZPL. The amplitude of the ZPL intensity resonance decreases with rising NV center concentration ρ_{NV}, while an increase of excitation power results in a stronger amplification of the ZPL intensity. In contrast to that, the amplitude of the ZPL energy resonance increases with rising ρ_{NV}. Moreover, the energy resonance shows a distinct Fano resonance like shape, which is, however, less pronounced (smaller Fano parameter q_F) in Ryab, the sample with the highest ρ_{NV}. A high power excitation leads to a Fano resonance with high q_F, although the amplitude of the energy resonance might be reduced. Highest intensity amplification and an energy resonance with maximal amplitude can be observed at temperatures between 6 and 15 K.

5.2 NV^0 ZPL under resonant excitation of NV^- center

Since the NV^- ZPL shows resonances at resonant excitation of the NV^0 center, the next logical step is to look for a resonance of the NV^0 ZPL under resonant excitation of the NV^- center. However, an NV^0 ZPL cannot be observed with excitation energies below the NV^0 ZPL energy. Therefore, it is necessary to perform a two-beam experiment. One laser with the excitation energy E_{ex}^{res} is resonantly exciting the NV^- centers, while a second laser with the excitation energy E_{ex}^{non} is non-resonantly exciting both, the NV^0 and NV^- centers. Again, the focus will be on the low concentration sample BP only.

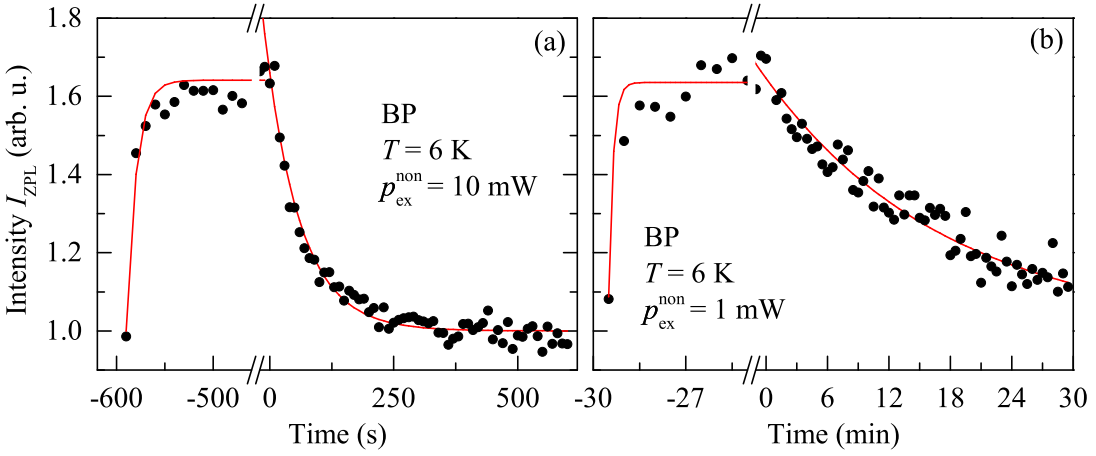

Figure 5-9: Temporal evolution of the NV^0 ZPL intensity, normalized to show its relative increase, when the NV^- center is resonantly excited. At $t = 0$ s, the resonant excitation of the NV^- center with $E_{ex}^{res} = 1.946$ eV, $p_{ex}^{res} = 20$ mW is blocked, only the non-resonant laser at $E_{ex}^{non} = 2.33$ eV is illuminating the sample. The power of the non-resonant laser is (a) $p_{ex}^{non} = 10$ mW and (b) $p_{ex}^{non} = 1$ mW. The red solid lines are exponential decay fit functions $\propto e^{-t/\tau}$. The error does not exceed the symbol size.

In Fig. 5-8 (a) the normalized intensity of the NV^0 ZPL is shown as a function of the excitation energy E_{ex}^{res} of the resonant laser. As expected, the intensity of the NV^0 ZPL rises about (93 ± 3) % at resonant excitation of the NV^- center. This increase is, however, smaller than that observed for the NV^- ZPL. This may be due to the additional excitation with the non-resonant laser, which causes a background. Therefore, the NV^0 ZPL intensity increase is not comparable to that observed for the NV^- ZPL. In contrast to that, the width of the NV^0 ZPL resonance $w_L = (340 \pm 20)$ μeV is again in good agreement with the linewidth of the NV^- ZPL $w_L = (393 \pm 5)$ μeV.

When looking at the peak energy of the NV^0 ZPL, which is illustrated in Fig. 5-8 (b) as a function of the excitation energy of the resonant laser, a Fano resonance is seen at resonant excitation of the NV^- ZPL. The width of this Fano resonance $w_F = (240 \pm 60)$ μeV is significantly smaller than the width of NV^0 ZPL intensity resonance and the NV^- line, but comparable with the width obtained for the NV^- ZPL peak energy resonance at medium excitation powers. The amplitude $A_F = (11 \pm 1)$ μeV, however, is a lot smaller compared to the values observed for the resonance of the NV^- ZPL. Nevertheless, the resonance is much more pronounced, indicated by a Fano resonance factor of $q_F = (2.0 \pm 0.1)$, compared to the Fano resonances which can be measured for the NV^- ZPL.

Moreover, the two-beam experiment offers the possibility to take a look at the temporal evolution of the NV^0 ZPL resonance. For this purpose the laser which resonantly excited the NV^-center was blocked. Subsequently, the NV^0 ZPL was detected, illuminated only by the non-resonant laser. In Fig. 5-9 (a) the normalized intensity of the NV^0 ZPL is depicted as a function of the time t passed since the first,

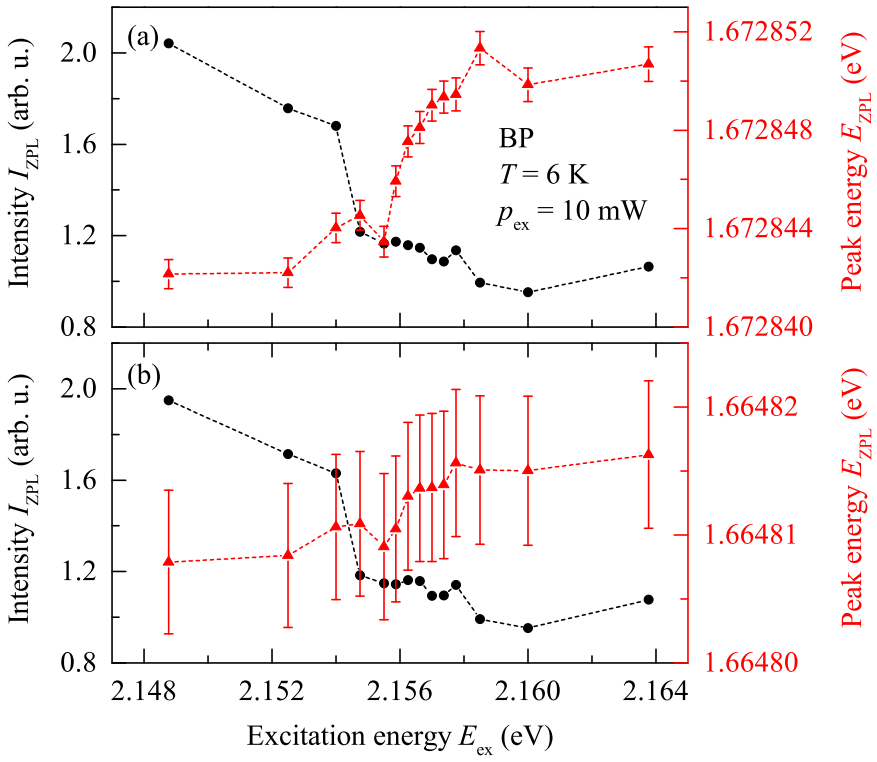

Figure 5-10: Intensity I_{ZPL} (black dots) and peak energy E_{ZPL} (red triangles) of (a) the high- and (b) the low-energetic V^0 ZPL determined by Gaussian fits at resonant excitation of the NV^0 center as function of the excitation energy E_{ex}. The ZPL intensity is normalized to show the relative increase of the ZPL. Dashed lines are guides to the eye. Unless shown otherwise, the error does not exceed the symbol size.

resonant laser was blocked. As one can see, the intensity decreases with time. After about $t = 200$ s, the effect of additional resonant excitation of the NV^- center vanishes. A fit with an exponential function $\propto e^{-t/\tau}$ results in a decay time of $\tau = (71 \pm 4)$ s. It must be noted that NV^0 ZPL intensity increases much faster when the resonant laser is unblocked again. An exponential fit gives a rise time of about $\tau = (10 \pm 1)$ s, which is in the region of experimental accuracy, since the step width is 10 s.

However, much longer decay times can be achieved when lowering the excitation power of the non-resonant laser. In Fig. 5-9 (b) the temporal evolution of the NV^0 ZPL intensity is shown with an excitation power of $p_{ex}^{non} = 1$ mW, which is ten times less than in the previously discussed measurement. At this low power the decay time is about $\tau = (18 \pm 5)$ min. In contrast to that, the rise time $\tau = (9 \pm 2)$ s does not change.

5.3 V^0 ZPL under resonant excitation of NV^- center

For the sake of completeness, not only the interaction between the two charge states of the NV center is investigated, but an interplay between the NV and the V^0 center is studied as well.

In Fig. 5-10 (a) the intensity (black dots) and energy (red triangles) of the V^0 ZPL are presented as functions of the excitation energy. In contrast to previous findings, neither an increase in the ZPL intensity at resonant excitation of the NV^0 center nor a Fano resonance of the V^0 ZPL energy can be seen. The intensity of the V^0 ZPL decreases with rising excitation energy, which might be due to a lower absorption efficiency at high energies. The peak energy of the V^0 ZPL line, however, increases about 7 μeV when the energy exceeds the NV^0 ZPL energy. This small increase is about one order of magnitude smaller, compared to the energy shifts one observes in the Fano resonances of the NV center ZPL energy. Moreover, it is in the region of the spectrometers accuracy. Hence, one can conclude, that there is no sign for a coupling between NV^0 and V^0 centers. It is worthwhile to notice that the low-energetic ZPL of the V^0 center exhibits a behavior similar to that of the high-energetic ZPL, as shown in Fig. 5-10 (b).

5.4 Discussion of the ZPL intensity and energy resonances

In the following section, the origin of the observed resonances will be identified. At first, the resonance of the NV center ZPL intensity is considered. It is most likely that this resonance is due to effective recharging of the NV centers via resonant excitation. Subsequently, the ZPL energy resonance is discussed. It is shown that the Fano effect sufficiently explains the observations.

5.4.1 Luminescence enhancement via effective recharging

Previous investigations have shown that recharging of NV centers plays a crucial role for the intensity of the observed ZPL. [100] In fact, NV centers can change their charge states when being excited. A detailed picture of this charge state transformation is illustrated in Fig. 5-11. Starting with the NV^0 in the ground state, an optical excitation lifts an electron (red solid arrow) from the a_1 orbital to the e_y orbital, leaving the defect center in the excited state NV^{0*}. By absorption of a second photon, an electron from the a_1' orbital is lifted to the a_1 orbital. Subsequently, a valence band electron (green solid arrow) occupies the vacant state (green dotted arrow) leaving the NV center in the negative NV^- state. Via optical excitation an electron from the a_1 orbital is lifted to the e_y orbital, and therefore the center is in its excited state NV^{-*}. Due to absorption of another photon accompanied by an Auger process (blue dotted arrow), the two electrons of the e_y orbital are lifted to the conduction band, while one electron from the conduction band occupies the a_1 orbital. Finally, the NV center is in the neutral ground state NV^0 again. A detailed discussion of this charge state transformation circle was done by P. Siyushev et al. in [58].

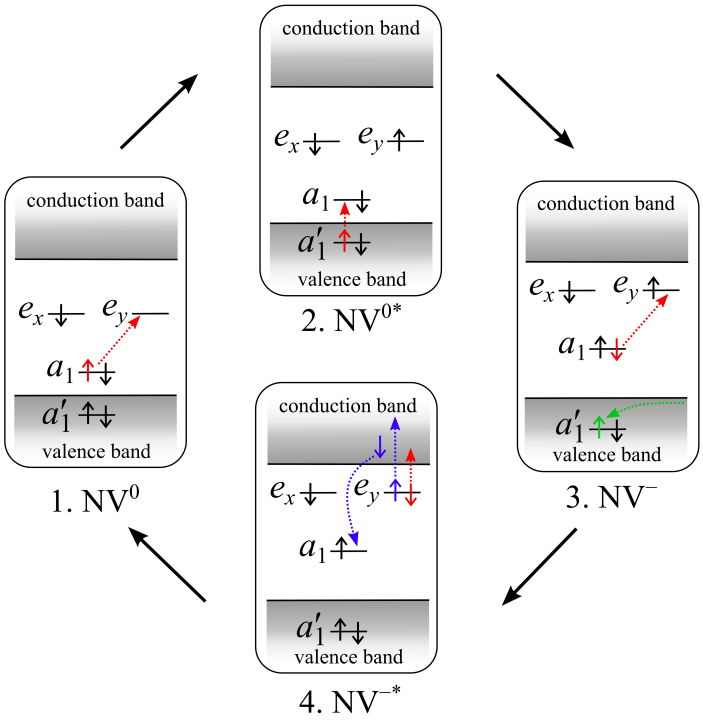

Figure 5-11: Charge state transformation circle of NV centers. Via optical excitation (red dotted arrows), as well as hole migration (green dotted arrow) and an Auger process (blue dotted arrow) the NV centers can change their charge states.[58] The solid arrows indicate electrons with spin $\pm\frac{1}{2}$, which occupy the molecule orbitals of the NV center a'_1, a_1, e_x and e_y.[46]

Essential for this charge state transformation circle is that the NV centers are in their excited states. PLE experiments on single NV centers have shown that at excitation energies below the ZPL energy of the NV^0 center an NV$^-$ ZPL cannot be observed.[28] This is due to the fact that excited NV$^-$ centers will at some point change their charge state, whereas the NV^0 centers keep their charge state if the energy of the exciting laser is too low for excitation. One can conclude that recharging is very important to gain high ZPL emission. For instance, a high NV$^-$ ZPL intensity does not only indicate effective excitation of the NV$^-$ centers, but also effective recharging, which in turn requires effective excitation of NV^0 centers, too. The NV^0 centers are most efficiently excited in a resonant manner. This is why the resonance of the NV$^-$ ZPL intensity can be observed at the exact energy of the NV^0 ZPL.

Apparently, most observed characteristics of the intensity resonance can be satisfyingly explained by effective recharging. It was observed that the resonance is smaller in samples with high NV center concentration. In these samples the density of pure nitrogen impurities, which act as electron donors, is high as well. Hence, charge impurities like the substitutional nitrogen are optically excited too and recharge the

NV^- centers.[100, 101] Due to the high amount of resident electrons, recharging of NV^- centers via excitation of NV^0 centers plays a minor role. That is why the resonances are smaller. A similar effect can be seen when exciting with big spot sizes.

For the charge transfer process two-photon absorption is involved. This nonlinear process is most likely to occur at high powers. Therefore, one observes the strongest resonances at high excitation powers, compare Fig. 5-4 (a) and (c). The temperature dependence of the resonances, see Fig. 5-6 (a), can be explained by the broadening of the NV^0 ZPL. Due to this broadening, the energy range for resonant excitation of the NV^0 center becomes broader too, which in turn leads to a broadening of the observed NV^- ZPL intensity resonance. In addition to the broadening of the resonance, a decrease of the NV^- ZPL amplification H_L with increasing temperature is observed. In contrast to that, the spectrally integrated amplification $H_\mathrm{L} \cdot w_\mathrm{L}$, see Fig. 5-6 (c), increases with rising temperature. However, most prominent is the small resonance at 1.8 K. At this temperature the by far smallest NV^- ZPL intensity resonance is observed in the low concentration sample BP. Apparently, the recharging circle is inhibited at low temperatures, since the kinetic energy of the conduction band electrons, which has to be sufficiently high for an Auger process to take place, scales with temperature.

The increase of the NV^- ZPL linear polarization degree at resonant excitation, see Fig. 5-2 (d), indicates that the recharging process is polarization selective. A high linear polarization degree indicates that the emission from the excited states with $m_L = \pm 1$ is stronger than the emission from the $m_L = 0$ states. Therefore, NV^- centers with excited states with non-zero orbital angular momentum seem to be more likely to change their charge state. Hence, at least one of the two processes which are involved in the transformation from the negative to the neutral charge state, namely the Auger process and two-photon absorption, must be polarization selective. Both processes lift an electron from the molecular orbitals e_x and e_y to the conduction band. Since the lowest conduction band of diamond is p-like, even the conduction band electrons which are lowest in energy have non-zero orbital angular momentum.[102] Due to angular momentum conservation, electron transitions from the circularly polarized states of the NV^- center, with $m_L = \pm 1$, to the conduction band are preferred. However, transitions from the linearly polarized states, with $m_L = 0$, which are actually superpositions of the $m_L = +1$ and the $m_L = -1$ states, would imply a symmetry reduction, yielding a lifting of the angular momentum conservation, and therefore, are less likely to take place.

Moreover, the circumstance that one not only observes a resonance of the NV^- ZPL at resonant excitation of the NV^0 center, but also a resonance of the NV^0 ZPL at resonant excitation of the NV^- center, see Fig. 5-8 (a), stresses that the recharging process is in fact a circle.

In order to analyze the dynamics of the recharging process, the results of the time resolved measurements, compare Fig. 5-9 (a) and (b), are taken into account. It becomes apparent that resonant excitation of the NV^- centers leads to a fast recharging of NV^0 centers, since the NV^0 ZPL intensity increases to its maximum within a relatively short rise time of about 10 s. Taking into account that the time resolution defined by the step width of the measurement is also 10 s, the actual rise time may be even shorter.

However, blocking the resonant excitation of the NV^- centers does not vice versa cause a rapid decrease of the NV^0 ZPL. On the contrary, the decay time is in the order of 20 minutes, if the excitation power is chosen adequately low. This is due to the fact that only excited NV centers undergo a charge transfer. At low power excitation less NV centers are excited, and hence less NV centers change their charge state. Therefore, it takes longer until a charge state equilibrium is reached. Furthermore, one can conclude that a single NV center can be optically excited and emit a ZPL photon several times before it changes its charge state. This conclusion is well in line with previous findings, which show that the NV centers maintain their charge state over weeks, when kept in the dark.[103]

5.4.2 Fano effect in the NV center ZPL

In the following section, the resonance in the NV centers ZPL energy will be discussed. As shown in Fig. 5-2 (b) and Fig. 5-8 (b), the resonance of the NV^- ZPL energy at resonant excitation of the NV^0 center as well as the NV^0 ZPL energy at resonant excitation of the NV^- center are of distinct asymmetric shapes, which can be very well fitted by Fano resonances according to Eq. (5.2).

A Fano resonance occurs when two scattering amplitudes or optical pathways interfere with each other. One of those pathways, the so called background process connects a ground state with a continuum of energy states, the other, the so called resonant process, connects the ground state with a discrete excited state. The Fano factor q_F gives the ratio between the resonant and the background process.[99] In the case of NV centers, the background process is the non resonant excitation of the NV center, which lifts an electron from the ground state to the phonon continuum, while the resonant process is the resonant excitation of the NV center, which lifts an electron directly from the ground to the first excited state. This Fano effect is depicted in Fig. 5-12 (a) for resonant excitation of the NV^0 center. In this case the Fano resonance of the NV^- ZPL energy is caused by an interference of the resonant excitation of the NV^0 center (red arrow) and the excitation into the NV^- phonon continuum (blue arrow), both at 2.156 eV.

In analogy to that, one might expect an interference between the resonant excitation of the NV^- center at 1.946 eV (red arrow) and the excitation into the NV^0 phonon continuum at 2.33 eV as well. Such an interference, which would explain the observation of a Fano like resonance at resonant excitation of the NV^- center, is shown in Fig. 5-12 (b). However, typically a Fano resonance only takes place if the energy of the resonant process is similar to the background process' energy, since such an energy degeneracy is necessary for interference. Therefore, there has to be some sort of quantum mechanical interaction between the two charge states of the NV center which creates the required degeneracy. The most obvious interaction between the NV^0 and the NV^- center is the charge state transformation circle, which, moreover, is most efficient at resonant excitation. This implies that the NV centers have no defined charge state, but actually exhibit a superposition state of the neutral NV^0 and the negatively charged NV^-. Hence, the Fano effect is caused by an interference between the envelope functions of

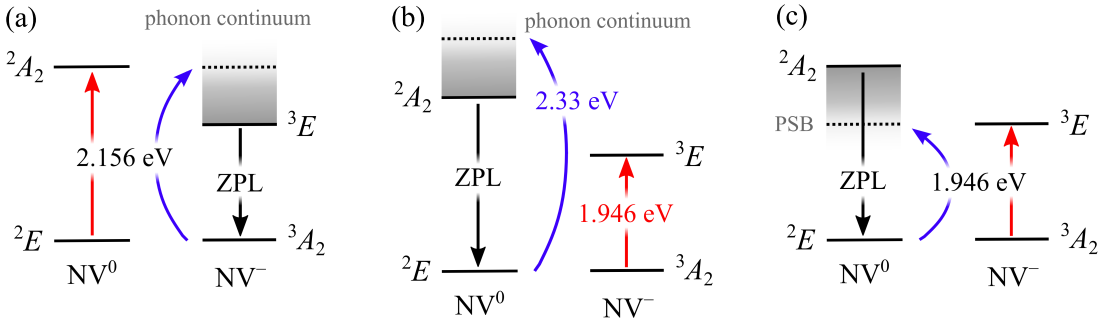

Figure 5-12: Fano effect for resonant excitation of the (a) NV^0 and (b), (c) NV^- centers. Interference between resonant absorption (red arrow) and absorption by a continuum (blue arrow) leads to a Fano resonance in the energy of the emitted ZPL (black arrow).

the electrons of a single NV center. Alternatively, there might be an interference of the envelope functions of differently charged, spatially separated NV centers. The excited states of color centers in NaCl, for instance, show widely diffuse wave functions which extend far beyond the dimensions of the defect center itself.[104, 105]

Another possible explanation for the Fano resonance at resonant excitation of the NV^- center is illustrated in Fig. 5-12 (c). Here, the resonant process is the resonant excitation of the NV^- center at 1.946 eV (red arrow) and the background process is an excitation (blue arrow) of a virtual state in the PSB of the NV^0 center with the same energy. The additional excitation at 2.33 eV (not shown) excites the NV^0 center, and therefore enables the detection of the NV^0 ZPL, which is affected by the Fano effect. Note that the emission of the NV^0 PSB is not very pronounced, especially at low temperatures and at an energy of 1.946 eV, compare Fig 2-7. Hence, it is highly unlikely that such a background process leads to a Fano resonance which is as pronounced as the one observed for resonant excitation of the NV^- center.

Since the Fano effect is a consequence of interference between two scattering amplitudes, the distinct resonance usually can be observed in the intensity of PL or absorption spectra, but not in the energy of an optical transition. However, an ensemble of NV centers exhibits inhomogeneous broadening of the energy states. Hence, a resonant excitation of a specific charge state of the NV centers actually only excites a subset of these NV centers resonantly. Only between the resonant process of this subset and the background process a Fano effect can occur. As a consequence, only the scattering efficiency of this subset of states is affected by the Fano effect. However, since the laser is tuned over a wide energy range, at one point every subset has been resonantly excited. In addition to that, the optical signal of the whole ensemble is detected. Hence, a superposition of the ZPLs emitted by the subsets is observed. In turn an intensity modulation of the ZPL emitted by a subset of NV centers leads to an energy shift of the detected ZPL. In other words, the selective resonant excitation of NV center subsets results in a Fano resonance in the ZPL intensity of these subsets only. The superposition of the ZPLs from all subsets leads to

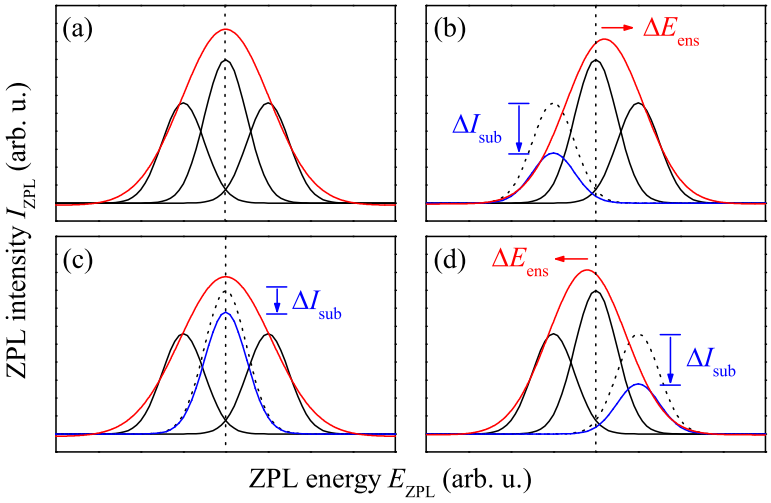

Figure 5-13: (a) The ZPL of NV center ensembles (red) is composed of the ZPLs emitted by subsets of NV centers (black). (b) - (d) ZPL intensity changes ΔI_{sub} (blue) of one subset of NV centers due to the Fano effect leads to an energy shift ΔE_{ens} (red) of the NV center ensemble's ZPL.

a shift of the ensemble ZPL energy, and therefore mirrors the Fano resonances of the subset ZPLs. A simplified picture of this ensemble effect is shown in Fig 5-13.

A strong argument for this explanation is that the energy shift of the ZPL due to the Fano effect is quite small compared to the linewidth w_{L} of the ZPL. In most measurements the amplitude of the Fano resonance A_{F} is about one order of magnitude smaller than w_{L}. Moreover, the largest energy shift is observed in Ryab, the sample with the highest NV center concentration. In this sample one can expect to observe the strongest ensemble effects. In addition, a reduction of the ZPL linewidth at the resonance energy can be seen, compare Fig 5-2 (b), which indicates that the number of NV centers contributing to the emission process of the ZPL is reduced.

Therefore, the width of the Fano resonance w_{F} is primarily determined by the ZPL linewidth of the resonantly excited NV centers, compare Fig. 5-4 (a) and (b), as well as Fig. 5-6 (a) and (b). Most likely, the amplitude of the Fano resonance A_{F} scales with the ZPL linewidth, too. Comparing the samples BP and Ryab, one can see that the linewidth of the NV^- ZPL increases from $w_{\mathrm{L}} = (0.504 \pm 0.005)$ meV to $w_{\mathrm{L}} = (3.99 \pm 0.04)$ meV due to inhomogeneous broadening; this is an enhancement by a factor of 7.9 ± 0.1. As one can see in Fig. 5-2 (b) and Fig. 5-3 (d), the amplitude A_{F} increases from $A_{\mathrm{F}} = (92 \pm 3)$ μeV to $A_{\mathrm{F}} = (730 \pm 60)$ μeV, which represents an enhancement by a factor of 7.9 ± 0.7. This supports the assumption that the Fano resonance amplitude increases due to inhomogeneous broadening. The divergent observation for YS, compare Fig. 5-3 (b), is most likely due to the high excitation power density, since high power excitation reduces the Fano resonance amplitude, compare Fig. 5-4 (b).

Previous investigations on quantum dots have shown that the Fano effect is

nonlinear, and therefore depends on the excitation power. This is due to a different response of the two optical pathways on high excitation powers. The resonant pathway saturates at high laser power, whereas the weaker background process typically does not show any saturation.[106] This is in line with the finding that the Fano factor q_F strongly increases with rising excitation power, compare Fig. 5-4 (c).

A significant temperature dependence of q_F is not observed, but the NV center concentration plays a crucial role. For the low-concentration sample BP one gets $q_F = 0.7 \pm 0.1$ at medium excitation powers, whereas the high-concentration sample Ryab shows a much less pronounced Fano resonance with $q_F = 0.1 \pm 0.05$. Note that the high q_F in YS is most likely due to the much higher excitation power density in comparison to BP. The small q_F indicates that the background process is much more prominent compared to the resonant excitation of the NV^0. Keeping in mind that the intensity resonance is rather small too, compare Fig. 5-3 (c), this stresses the claim that the recharging of NV^- centers via NV^0 excitation is not the main process, but rather the recharging by resident electrons provided by the nitrogen impurities. However, this implies that the efficiency of the charge transfer between the NV centers is mirrored by the quality factor q_F of the Fano resonance.

5.5 Conclusion

It was shown that the luminescence efficiency of the neutral and negatively charged NV centers can be optimized by resonantly addressing the respectively other charge states of the defect centers. The recharging process, which is essential to maintain ZPL emission, is most efficient at such a resonant excitation. Moreover, such resonant excitation of NV centers leads to Fano resonances in the energy of the ZPLs. This resonances are due to an interference between the discrete transition of the resonantly excited NV centers and a continuous transition of the nonresonantly excited NV centers. Due to ensemble effects, the Fano effect, which individually affects subsets of the NV center ensemble, is seen in the energy of the NV center ensemble ZPL. In addition, the observed Fano resonance points towards NV centers exhibiting a charge-state superposition between the neutral and the negative charge state.

Chapter 6

Resonant microwave excitation of NV^- centers' ground states

The basic optical properties of the NV centers have been studied well by using, in particular, electron spin resonance (ESR) techniques under application of external magnetic fields of a few tens or hundreds of mT.[70, 81, 107, 72] Using even higher magnetic fields together with additional microwave application enables the detection of optically detected magnetic resonances (ODMRs),[11] which are not influenced significantly by level mixing, as addressed in Chapter 7, and nuclear-electron interactions. Thus, the ODMRs are mainly dominated by the Zeeman effect.

In this chapter, the optical response of an ensemble of NV^- centers in diamond to high-frequency MW radiation of 60 GHz is presented. The experimental setup used for the measurements is described in Sec. 2.3. A brief introduction in the basic principle of ODMR can be found in Sec. 6.1. In Sec. 6.2 the ODMR spectra of the NV^- centers are analyzed. Special focus is drawn to the orientation of the magnetic field with respect to the symmetry axes of the NV^- centers and the diamond crystal. Moreover, the dependence of the ODMR on the power of both, the exciting MWs as well as the laser light, is investigated in Sec. 6.3. The findings of this chapter are summarized in Sec. 6.4. Note that this chapter covers results which are prepared to be published.[108]

6.1 The principle of ODMR

In order to investigate transitions with energies far below the energy range of visible light, such as transitions in the triplet states of the NV^- center, the method of optically detected magnetic resonance can be used. ODMR spectroscopy is based on the principle of electron spin resonance techniques.[48] The basic principle of ESR is illustrated in Fig. 6-1 (a) on the basis of the $^3A_2$ ground state of the NV^- center, but it works with an arbitrary two-level spin system too. Due to Zeeman splitting ΔE_Z at the presence of an external magnetic field B, the spin levels are separated in energy, compare Sec. 3.1. By applying an electromagnetic field, with frequency ν, transitions between the two spin states with spin projection $m_S = 0$ and $m_S = +1$ can be induced. However, crucial

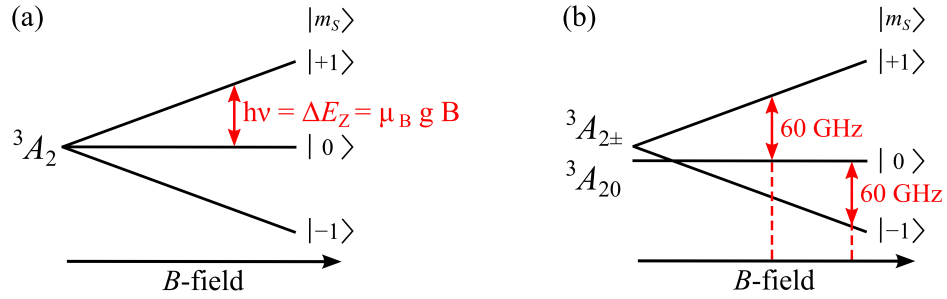

Figure 6-1: (a) Basic principle of ESR: Electromagnetic radiation induces transitions between the $m_S = 0$ and $m_S = +1$ spin levels of the NV^- ground state $^3A_2$ in an external magnetic field B. Note that zero field splitting is neglected. (b) Principle of ODMR: 60 GHz MW radiation induces ESR (red arrows) between the $m_S = 0$ and $m_S = \pm 1$ states of the NV^- ground state $^3A_2$. Due to zero-field splitting, there are resonant transitions at two distinct magnetic fields.

for this process is that the energy of the electromagnetic radiation E_{MW} is equal to the Zeeman splitting of the spin states:

$$\Delta E_{\mathrm{Z}} = \mu_{\mathrm{B}} g B = E_{\mathrm{MW}} = h\nu \quad . \tag{6.1}$$

Here, h is the Planck constant. Typically, such ESR experiments are performed at a magnetic field of about $B = 1$ T and with g-factors of about $g = 2$. Hence, the resonance frequency, which is about 10 GHz, lies in the range of MW radiation.

When the resonance condition Eq. (6.1) is fulfilled, transitions from a high-energetic level $|\mathrm{A}\rangle$ to a low-energetic level $|\mathrm{B}\rangle$ can be induced as well as transitions from $|\mathrm{B}\rangle$ to $|\mathrm{A}\rangle$. In the former case, energy is transfered to the radiation field, in the latter, the energy of the radiation field is reduced. However, both processes are equally likely to occur and proportional to the occupation $n_{\mathrm{A,B}}$ of the corresponding level.[109]

The MW power absorbed by the spin system is given by

$$P_{\mathrm{MW}} = \omega_{\mathrm{e}}(h\nu)(n_{\mathrm{A}} - n_{\mathrm{B}}) \quad . \tag{6.2}$$

Here, ω_{e} is the rate, with which transitions between the spin states are induced. The rate of transitions from $|\mathrm{A}\rangle$ to $|\mathrm{B}\rangle$ is given by $\omega_{\mathrm{e}} n_{\mathrm{A}}$, whereas the rate of transitions from $|\mathrm{B}\rangle$ to $|\mathrm{A}\rangle$ is given by $\omega_{\mathrm{e}} n_{\mathrm{B}}$. With sufficient P_{MW} an equilibrium will be achieved in which both states are equally populated.

ODMR is a method of detecting ESR via an electronic transition in the optical spectral range. In case of the NV^- centers, this transition is the well known ZPL at 1.946 eV. The ESR induces a state mixing between the $m_S = 0$ and $m_S = \pm 1$ spin states when the resonance condition is fulfilled. As a consequence, the NV^- ZPL intensity is reduced.[54, 107] A detailed discussion of comparable intensity drops can be found in Chapter 7. ODMR can be observed in various other spin systems too. Important is that the transition ratios for the two optical pathways coupled by the ESR differ, which is, however, mostly the case.

When measuring an ODMR spectrum, one can either change the MW frequency ν or the magnetic field B. When the resonance condition according to Eq. (6.1) is fulfilled, a distinct intensity decrease of the optical signal (for instance the NV$^-$ ZPL) can be observed, indicating an ESR. For the measurements presented in this work, the MW frequency is constant and the magnetic field is varied and hence, the resonance condition can be written as:

$$B = \frac{\Delta E_{\mathrm{Z}}}{\mu_{\mathrm{B}} g} = \frac{h\nu}{\mu_{\mathrm{B}} g} \quad . \tag{6.3}$$

Since the used MW frequency is about $\nu = 60$ GHz and the g-factor of the NV center is approximately in the order of the free electron g-factor $g_0 = 2$, the magnetic field must be $B \approx 2$ T to fulfill the resonance condition for ESR.

6.2 ODMR in the NV$^-$ ground state

In the following section, the ODMR of the NV$^-$ centers under 60 GHz MW excitation will be presented. Note that all measurements were performed at room temperature on YS, since this is the only sample with suitable dimensions to be placed inside the MW cavity. The PL of the NV$^-$ centers, measured at an external magnetic field of $B = 2.093$ T applied along the (111) crystal direction, is depicted in Fig. 6-2 (a). The PL spectrum shows the NV$^-$ ZPL at 1.9468 eV with a linewidth of 8.3 meV as well as the PSB with two broad peaks at a distance of 65.8 and 128.8 meV to the ZPL, which may stem from a nitrogen-related vibration mode (63.9 meV) that transforms as the irreducible representation e.[90] By additionally exciting the NV$^-$ centers with MWs with a frequency of 60 GHz at the respective magnetic field strength, the PL intensities of the ZPL and PSB decrease significantly. Correspondingly, the difference $\Delta I_{\mathrm{PL}} = I_{\mathrm{PL}}^{\mathrm{on}} - I_{\mathrm{PL}}^{\mathrm{off}}$ of the PL intensities for switched-on and switched-off MW excitation is negative throughout the measured spectral region, see Fig. 6-2 (b). To identify the spin transitions that are resonantly addressed via the MWs, ΔI_{PL} is integrated spectrally over the whole detection range from 1.79 to 1.97 eV and measured as function of the magnetic field strength ranging from 2.07 to 2.31 T.

When the magnetic field vector $\mathbf{B}$ is applied along the (111) crystal direction, see Fig. 6-2 (c), four resonances can be observed symmetrically centered around 2.19 T. The weak inner resonance lines seem to have a more Voigt-like shape, while the intense outer resonances can be fit best by Gaussian functions. The line shapes of the outer resonances hint towards at a saturation of spin-state population. It is assumed that the ODMR transition lies in the $^3A_2$ ground state of the NV$^-$ center.[36, 107] In Fig. 6-1 (b) the energy splitting due to the Zeeman effect is illustrated. Due to a zero field splitting of about 2.87 GHz (12 μeV) between the $^3A_{20}$ state with vanishing spin projection and the $^3A_{2\pm}$ states with spin projection $m_S = \pm 1$, MW excitation with 60 GHz leads to ODMR transitions (red arrows) at two distinct magnetic fields.

The energies of these ODMR transitions are simulated numerically by using the

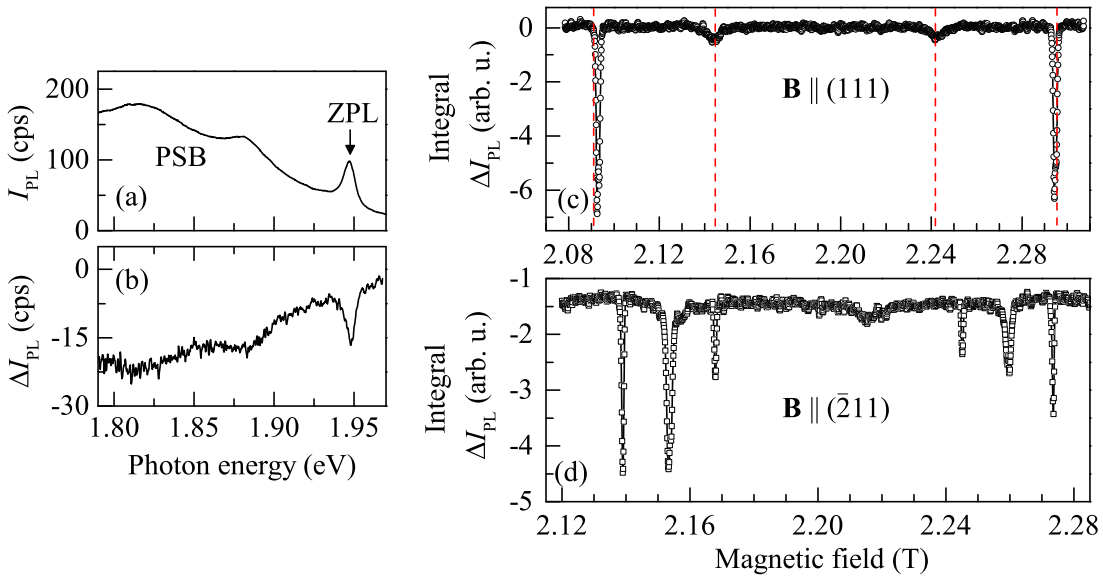

Figure 6-2: (a) Unpolarized photoluminescence spectrum shows the NV^- ZPL and partly its PSB; $T = 293$ K, $E_{ex} = 2.33$ eV. (b) Differential PL for a 60 GHz MW application with $P_{MW} = 125$ mW. (c) Integrated differential PL intensity dependent on the magnetic field for **B** applied along the (111) and (d) ($\bar{2}11$) crystal directions. Dashed red lines indicate the numerically calculated magnetic field for ESRs.

following Hamiltonian of C_{3v} symmetry for the ground state of the NV^- centers:

$$H = g_S \mu_B \mathbf{BS} + D_{gs} \left(S_z^2 - \frac{2}{3} \right). \tag{6.4}$$

Here, $D_{gs} = 2.87$ GHz is the ground state's zero field splitting due to the axial crystal field. Strain-induced effects are neglected, since the overall Zeeman splitting is much larger than the strain terms $E(S_x^2 - S_y^2)$ for the ground state. The spin g-factor is given by $g_S = 2.0$,[70] μ_B is the Bohr magneton, and **S** is the spin vector. Note that the contribution of the orbital angular momentum can be neglected, since the ground state has zero orbital angular momentum. Of main importance, however, is the orientation of the magnetic field with respect to the crystal axis.[110, 81]

According to the lattice symmetry of diamond, NV centers are oriented along the (111), ($1\bar{1}\bar{1}$), ($\bar{1}1\bar{1}$), and ($\bar{1}\bar{1}1$) directions.[81, 111] With the vector of the external magnetic field **B** applied along the (111) crystal direction, in total one gets four resonant magnetic fields B_{res} which exhibit ESR transitions at 60 GHz MW excitation. For NV^- centers oriented along (111) one gets $B_{res} = 2.09081$ T and 2.29587 T, whereas for centers oriented along ($1\bar{1}\bar{1}$), ($\bar{1}1\bar{1}$), or ($\bar{1}\bar{1}1$) direction one gets $B_{res} = 2.14443$ T and 2.24119 T. The strongest resonances are attributed to the NV centers oriented in the (111) direction, since their symmetry axis coincides with the orientation of the magnetic field. The resonant magnetic fields are indicated by red

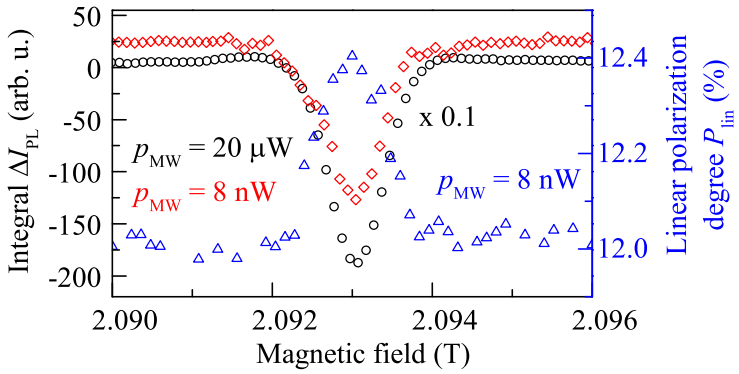

Figure 6-3: (a) Room temperature ODMR spectra, measured at moderate 20 μW (black dots, left scale) and ultra-low MW output power of 8 nW (red diamonds, left scale), as well as linear polarization degree P_{lin} of the NV$^-$ PL dependent on the applied magnetic field (blue triangles, right scale); $P_{\mathrm{laser}} = 5$ Wcm^{-2}, $\mathbf{B} \parallel (111)$.

dashed lines in Fig. 6-2 (c) and coincide well with the measured resonances. Therefore, one can conclude, in good agreement with previous findings, that only the ground states are affected by resonant MW excitation. There is no evidence for the involvement of the excited states. Note that even small deviations of the magnetic field orientation from the (111) symmetry axis of the crystal lift the degeneracy of B_{res} in the $(1\bar{1}\bar{1})$, $(\bar{1}1\bar{1})$, and $(\bar{1}\bar{1}1)$ directions. As a result, the width of the resonance increases. In fact, a small misalignment might be the reason for the different line shapes of the inner and outer resonances. Furthermore, the impact of a magnetic field alignment on the ODMR signal becomes apparent, when looking at other geometries. In Fig. 6-2 (d) the integral ΔI_{PL} of the NV$^-$ ZPL with $\mathbf{B} \parallel (\bar{2}11)$ is demonstrated. The ODMR signal looks very different compared to the signal detected with $\mathbf{B} \parallel (111)$; here, eight symmetric resonances are detected in total. This is because the geometry of the NV centers along the $(\bar{2}11)$ axis is less symmetric than along the (111) axis, compare Fig. 4-2.

6.3 ODMR at low MW power

In the following only the ODMR measured in the $\mathbf{B} \parallel (111)$ geometry for NV centers oriented along the (111) axis at about 2.093 T, which can be attributed to a transition between the states $^3A_{2-}$ and $^3A_{20}$, will be discussed. In Fig. 6-3 the ODMR signal is shown for moderate MW excitation with a power of $p_{\mathrm{MW}} = 20$ μW (black circles) as well as for ultra low MW power excitation with $p_{\mathrm{MW}} = 8$ nW (red diamonds), which is about five to seven orders of magnitude smaller than the power of the electromagnetic field of a customary mobile phone.[112] Even at such low MW power, the ODMR signal is quite prominent, the amplitude of the resonance is just about one order of magnitude smaller compared to excitation with 20 μW.

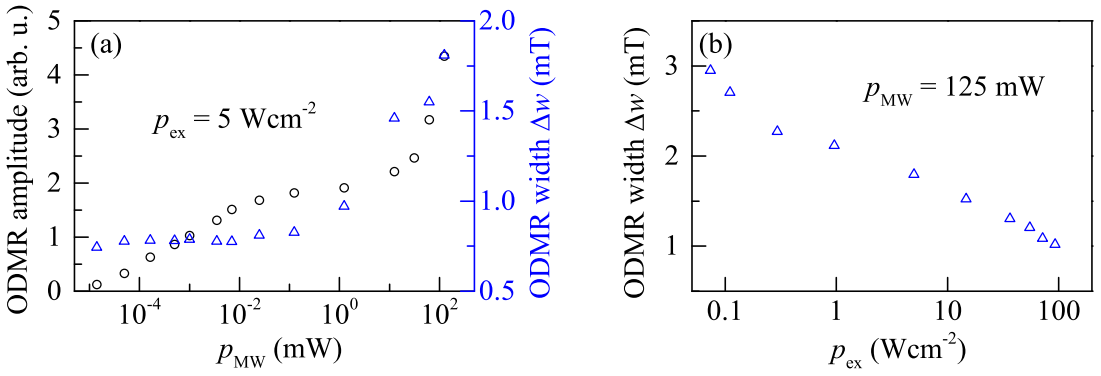

Figure 6-4: (a) Dependence of the resonance amplitude (black dots, left scale) and width Δw (blue triangles, right scale) on the MW output power p_{MW}. (b) Dependence the resonance width Δw (blue triangles) on the laser power density p_{ex}.

A detailed analysis of the MW power dependence of the resonance is depicted in Fig. 6-4 (a). As one can see, the ODMR amplitude (black circles) slowly increases to about $p_{\mathrm{MW}} = 10$ μW, then a saturation can be seen. However, at high MW powers exceeding 1 mW, the ODMR amplitude rises again. Simultaneously, an increase of the resonance width Δw of the ODMR (blue triangles) can be observed at powers of about 1 mW. It is worthwhile noticing that for excitation with smaller MW power, no changes in the resonance width can be seen. The nonlinearities observed for excitation with high MW power are most likely due to a reduction of the spin coherence time due to nonlinear spin effects.

Surprisingly, the ODMR width of the resonance at 2.093 T shows an opposite behavior under variation of the exciting laser power. In fact, Δw is reduced at high excitation powers, as one can see in Fig. 6-4 (b). This is most likely due to photo-ionization of the NV^- center at high laser power, accompanied by a trapping of the ionized electrons at nitrogen impurities. The ionization happens for centers with lower symmetry first. Thus, high-symmetry centers remain and the resonance line width becomes narrower because the excited ensemble is more homogeneous. In addition, the electron lifetime becomes shorter for high-power excitation.[113] Note that the resonance linewidth is not influenced by the fact that an ensemble of NV^- centers is excited; hence, ODMR is sensitive to a very small number of NV^- spins.

In addition to that, as one can see in Fig. 6-3, the linear polarization degree P_{lin} of the NV^- PL (blue triangles) shows an increase from 12.0 to 12.4 % at the resonant magnetic field. Here, P_{lin} is defined as $(I^{0°}_{\mathrm{ZPL}} - I^{90°}_{\mathrm{ZPL}})/(I^{0°}_{\mathrm{ZPL}} + I^{90°}_{\mathrm{ZPL}})$; the high index shows the polarization angle of the detected NV^- ZPL intensity I_{ZPL}. At the resonance field of 2.093 T, the MW excitation induces transitions between the $m_S = 0$ and $m_S = -1$ ground states. This in turn changes the transition efficiencies of the excited states with zero and non-zero orbital angular momentum.[54, 107] The increase in the linear polarization indicates that the linearly polarized transitions become more likely to occur than the circularly polarized transitions. A more detailed discussion of the increase in

the linear polarization at magnetic resonances is provided in Chapter 7.

6.4 Conclusion

In conclusion, optically detected magnetic resonance induced by 60 GHz MW excitation in an ensemble of NV^- centers is demonstrated at room temperature, even for ultra low MW excitation power. The ODMR amplitude of the 2.093 T resonance, which is attributed to the NV^- centers oriented along the (111) direction, is saturated at an MW power of a few tens of μW already, while a nonlinear behavior appears at very high MW excitation powers. The amplitude as well as the energy of the resonances strongly depend on the orientation of the magnetic field with respect to the symmetry axes of the NV^- centers and the crystal. This allows for the identification as well as selective addressing of equally oriented NV^- centers in an ensemble. Theoretical considerations of the spacial resolved Zeeman splitting show that only the ground states of the NV^- centers are influenced by the MW excitation. Moreover, an enhancement of the linear polarization degree at magnetic resonance conditions is observed, while the circular polarization degree remains unchanged. Note that high-frequency ODMR can be used to exclude strain induced state mixing, since only Zeeman splittings are relevant.

Chapter 7

Outlook: State mixing at low magnetic fields

In Chapter 4 the magnetic field dependence of the linear polarization degree P_{lin} was discussed for magnetic fields ranging from -9 T to 10 T. The minimal step width used in the corresponding PL measurements was about 1 T. In the experiments discussed in this chapter, however, the applied fields are in the range of a few 100 mT only. Note that the experimental setup had to be modified in order to enable precise control of the magnetic field, compare Sec. 2.3. At such small magnetic fields, the Zeeman splitting, compare Sec. 3.1, is in the range of the zero field splittings between the states in the NV^- center triplets $^3A_2$ and ^3E.

It was shown that the intensity of the NV^- ZPL is reduced due to the mixing of spin states, when the Zeeman splitting equals the zero field splitting. For instance, the zero field splitting between the $^3A_{20}$ and the $^3A_{2\pm}$ state is about 12 μeV, compare Fig. 1-3. Assuming the electronic g-factor is about the value of a free electron ($g_S = 2$), one can calculate that a magnetic field of 104 mT creates a Zeeman splitting of the same magnitude as this zero field splitting. At such magnetic field strengths the $^3A_{20}$ and $^3A_{2-}$ become degenerated. These mixing of spin states results in a decrease of ZPL emission. This is mostly due to the fact that there are two transition channels from the states with spin projection $m_S = \pm 1$ of the excited ^3E state (namely the direct ZPL transition to the ground states $^3A_{2\pm}$ and the transition via the ^1E and $^1A_1$ singlet states to the $^3A_{20}$ ground state), but only one transition from the exited states with $m_S = 0$ (namely the ZPL transition to the $^3A_{20}$ ground state). This results in a spin polarization into the $m_S = 0$ state. A high population in the $m_S = 0$ state, in turn, leads to an increase of the NV^- ZPL intensity.[54, 107] Spectral hole burning experiments have shown that there is in fact a level anti crossing at a magnetic field of about 103 mT.[114]

However, essential for the observation of the level anti crossing is that the magnetic field is aligned parallel to one of the NV center symmetry axes. A deviation of a few degrees leads to a remarkable broadening of the resonances; at angles of about 6° they are barely visible.[70, 72] This broadening is due to transversal magnetic fields, which

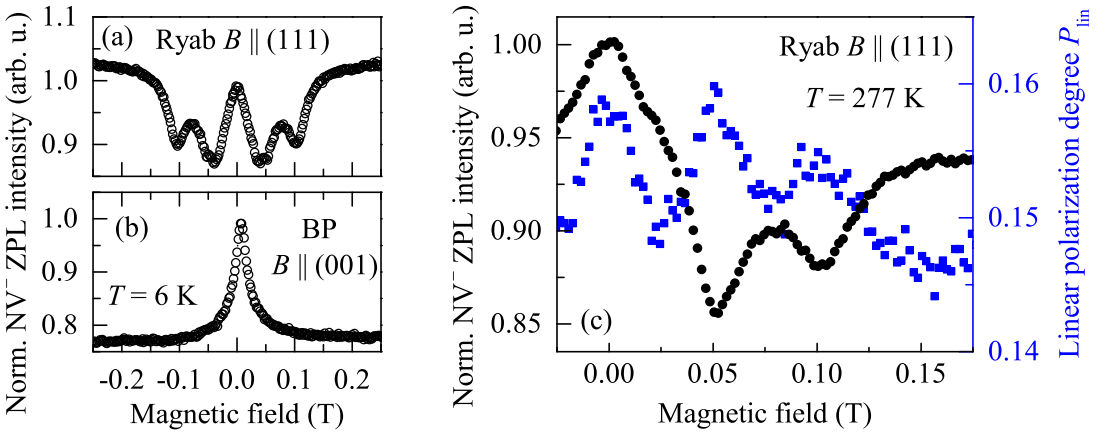

Figure 7-1: Magnetic field dependence of the NV^- ZPL intensity of (a) Ryab in the (111) and (b) BP in the (001) direction at $T = 6$ K. (c) Intensity (black dots) and P_{lin} of NV^- ZPL of Ryab in the (111) direction at $T = 277$ K. $E_{ex} = 2.33$ eV, $p_{ex} = 2$ mW for Ryab and 10 mW for BP. The ZPL intensity is normalized to the value at $B = 0$ T. For reasons of clarity, the experimental error of P_{lin}, which is about ± 0.003, is not depicted. The experimental error of the ZPL intensity is smaller than the symbol size.

lift the degeneracy of the spin states. In Fig. 7-1 (a) the NV^- ZPL intensity in Ryab is shown as a function of the magnetic field applied parallel to the (111) direction. One can clearly see that the intensity drops to 87 % at about ± 52 mT and to 90 % at ± 103 mT. The latter intensity drop can be explained with spin-level mixing in the NV^- ground state, whereas the former is due to additional mixing of the excited states. Note that the direction of the magnetic field can only be adjusted with an accuracy of a few degrees. Hence, the observed resonances might be broadened not only due to inhomogeneous broadening, but due to misalignment as well. In contrast to that, no NV^- ZPL drops are seen when the magnetic field is parallel to the (001) direction, as it is shown in Fig 7-1 (b) for BP. However, when an external magnetic field is applied, the ZPL intensity decreases to about 76 % at 150 mT; no further decrease is seen up to 500 mT. This is in line with theoretical calculations and experimental findings for large derivations of the magnetic field from the symmetry axes of the NV center.[72] Due to the mixing of $m_S = 0$ and $m_S = \pm 1$ states, the average lifetime of the NV^- center is decreased, which in turn leads to a reduction of the NV^- PL intensity.[81]

In Fig 7-1 (c) the intensity as well as the linear polarization degree P_{lin} of the NV^- ZPL in Ryab are shown dependent on the magnetic field in the range from -25 to 175 mT. In addition to the ZPL intensity drops at 52 and 103 mT, one can see that P_{lin} shows three distinct maxima at approximately 0, 50, and 100 mT. Apparently, the linear polarization is maximized when the spin-level mixing occurs.

An increase in the linear polarization degree indicates that linearly polarized transitions from the excited states with $m_S = 0$ to the $m_S = 0$ ground state become more likely than circularly polarized transitions from the exited states with $m_S = \pm 1$

to the $m_S = \pm 1$ ground states. However, with the energetic ordering of the NV^- singlet states according to [50, 72] (compare Fig. 1-3 and Fig. 3-5), which leads to a spin polarization into $m_S = 0$,[54, 70, 107] state mixing would rather lower than increase the efficiency of the linear polarized transitions. Hence, one would expect a decrease of the linear polarization at resonant magnetic fields, which triggers the state mixing. However, with an inverted energetic ordering, with ^1E being the ground state and $^1A_1$ being the excited state of the metastable singlet of the NV^- center, which was proposed by Delaney, Greer, and Larsson,[55] the increase in P_{lin} could be explained. They predicted spin polarization into $m_S = \pm 1$. Therefore, state mixing, in fact, would result in a decrease of the efficiency of circularly polarized transitions, which would lead to a drop of the NV^- ZPL intensity as well as to an increase in the linear polarization degree. Nevertheless, one should keep in mind that the observed change of the linear polarization is in the order of 1 %, which is rather small compared to the changes induced by applying a large magnetic field or due to crystallographic properties, compare Chapter 4. Hence, these results are of minor significance.

In addition, with the energy ordering presented in the frame of this thesis (compare Fig. 3-5), the polarization increase could also be explained by a direct transition from the excited state ^1E of the NV^- singlet to the ground state $^3A_{20}$ of the NV^- triplet. Such a transition would be spin conserving with a change in the orbital angular momentum of ± 1, and hence could be optically detectable. Therefore, further PLE experiments on the NV^- SST in the energy range between the ZPL and the SST of the NV^- center could enable a direct measurement of the energy gap between the NV^- singlet and triplet states, which is still undetermined.

Chapter 8

Outlook: A masing diamond

In this chapter the suitability of defect centers in diamond as a source of stimulated microwave emission will be discussed. In this context, special focus will be drawn to the realization of an experimental method to verify microwave amplification by stimulated emission of radiation (maser) in diamond. Although, the maser was realized seven years earlier, in 1953 by C. H. Townes and J. P. Gordon[115], it was the laser (light amplification by stimulated emission of radiation) which became essential in various modern technologies. The maser has only a few applications so far. For instance, in atomic clocks or as a low-noise MW amplifier in radio telescopes, and deep space communication stations.[116] In contrast to the laser, the operation of the well established masers requires high vacuum[117] or cryogenic temperatures.[118] However, in recent years the search for room temperature solid-state masers made remarkable progress. As a gain medium organic molecular crystals based on polyacenes are promising candidates[119, 120] as well as defect centers in silicon carbide,[121] but also NV centers in diamond have been suggested due to their long spin lifetime at room temperature.[122]

The ODMR setup, compare Sec. 2.3, was used in order to probe stimulated MW amplification in the diamond crystal YS. The power p_{MW} of the MWs emitted by the generator as well as the power p_{ref} of the MWs reflected from the cavity were monitored by the reflectometer and read out as voltages U_{MW} and U_{ref} proportional to the corresponding MW powers. In Fig. 8-1 the differential voltage $\Delta U = U_{\mathrm{ref}} - U_{\mathrm{MW}}$ is depicted dependent on the external magnetic field strength when the sample is excited with 60 GHz MWs and 2.33 eV laser light simultaneously. A negative ΔU indicates that MWs are absorbed by the diamond sample inside the cavity, whereas a positive ΔU is a sign for MW amplification. As one can see, the MWs are absorbed inside the cavity for small magnetic fields. However, at $B = 2.21$ T a sharp increase in ΔU can be seen. The power of the MWs reflected by the cavity is higher than the power of the MWs emitted by the generator. With rising magnetic field this MW amplification becomes weaker and ΔU decreases again.

On the basis of electron paramagnetic resonance (EPR) measurements, the resonance at $B = 2.21$ T can be associated with single substitutional nitrogen atoms in the carbon lattice of diamond. This paramagnetic defect center, mostly referred to

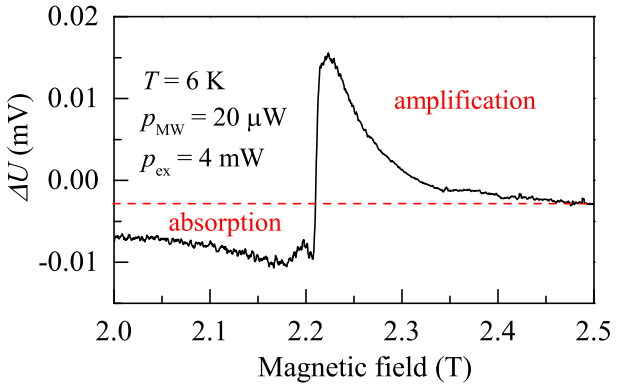

Figure 8-1: Voltage ΔU indicating the difference between emitted and reflected MW power dependent on the magnetic field. The resonance at $B = 2.21$ T indicates MW amplification.

as P1 center, is well known by EPR.[123] An MW amplification can be observed up to about 2.4 T. The great width of this resonance can be explained by the inhomogeneity of the P1 center ensemble, since the density of nitrogen impurities (30 ppm) is quite high. Note that the energy of the laser is suitable for exciting not only the P1 center but also NV^0, NV^-, and V^0 centers. It can, however, be assumed that the amount of NV^0 and V^0 centers in the sample is negligible, because of the high nitrogen concentration (compare Sec. 5.1.1) and the fact that the sample was annealed.[43] Apparently, the P1 centers in diamond cause the amplification of applied MW radiation when excited with 2.33 eV laser light. The frequency of the amplified MW is determined by the magnetic field. In the following section, two experimental techniques will be presented to probe if the diamond sample is capable of emitting MWs without external seeding with an MW generator.

The basic principle is to excite the diamond sample with laser light at the presence of a magnetic field, to induce MW emission. In order to detect the MWs emitted by the diamond crystal, a second sample, which is sensitive to MW radiation, is used. A possible MW detector probe is a ZnMnSe quantum well (CB1541).[124] The exciton[125] PL of the quantum well consists of a bright, narrow line at about 2.8 eV. For excitation a HeCd laser (IK Series, Kimmon Electric Co. Ltd.) emitting at 3.33 eV was used. To avoid heating of the Mn spin system a low excitation power of $p_{ex} = 3.7$ μW was chosen, resulting in a PL intensity of about 5000 cps. Heating of the Mn spin system would result in a shift of the PL line to higher energies. Such heating can be caused by additional excitation with a second laser, which should be lower in energy than the quantum well PL, or by MW excitation.

In order to distinguish laser and MW heating of the Mn spin system, a special sample holder was used. A scheme of the experiment is shown in Fig. 8-2 (a). While the ZnMnSe sample (green) is excited with a 3.33 eV laser (1^{st} laser, pink), the diamond sample YS (yellow) is excited by a laser with an energy of 2.18 or 2.03 eV (2^{nd} laser,

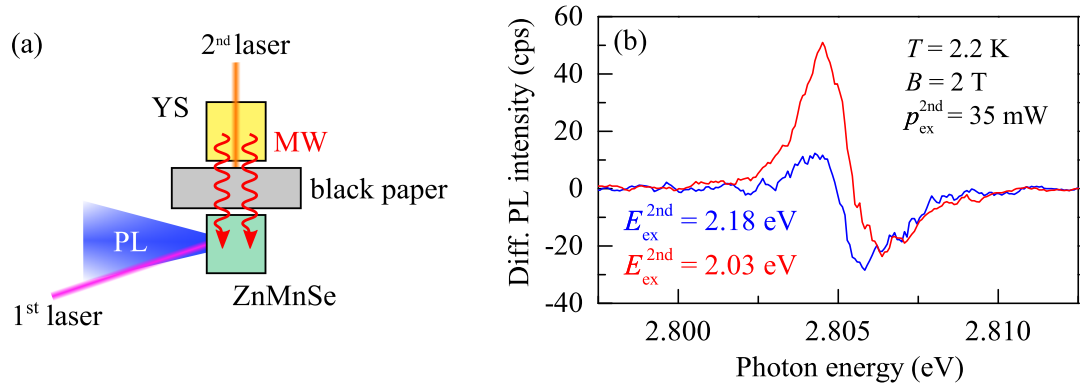

Figure 8-2: (a) Excitation scheme of the MW source YS (yellow) and probe, a ZnMnSe quantum well. The 1st laser is blocked by a black paper barrier (gray). Only the microwaves (red waved arrow) pass through and excite the ZnMnSe crystal (green). (b) Differential spectrum of the ZnMnSe quantum well exciton PL. Heating of the Mn spin system by MWs shifts the PL line to higher energies.

orange). The samples are separated by a thick barrier made of black paper (gray) to prevent any light of the 1st laser from hitting the ZnMnSe crystal. However, the MWs (red waved arrows) emitted by YS can travel through the paper and heat up the Mn spin system. In turn, the PL (blue) should show a remarkable energy shift. Apparently, this energy shift is rather small, and therefore two spectra of the ZnMnSe quantum well exciton PL were detected: firstly, a spectrum with excitation only by 1st laser and secondly a spectrum with excitation by both lasers. The differential intensity is depicted in Fig. 8-2 (b). A small shift to higher energies can be seen when the 2nd laser excites the diamond system. Hence, a heating of the Mn spin system is evident. This heating occurs most likely due to MWs emitted by the diamond crystal. Additional illumination with 2.03 eV laser light (red line) leads to a strong MW emission compared to exciting at the maximum of the NV^- center absorption band at 2.18 eV, because the excitation of P1 centers is more efficient. Therefore, the energy shift of the quantum well PL is smaller for excitation with 2.18 eV (blue line). However, the PL energy shifts are rather small and can also be explained by stray light of the 2nd laser which passes the paper shielding. In addition, the small difference of the g-factors of both systems, the P1 center ($g = 2.0024$)[123] on one side and the Mn spin system ($g = 2$)[124] on the other side, may result in the emission of MWs which are slightly detuned from the magnetic resonance of the Mn spin system. To overcome this obstacle, an advanced experimental setup has to be designed allowing independent control of the magnetic fields applied to both samples.

Alternatively, a system, which shows suitable magnetic resonance, can be used as MW probe. For instance, NV^- centers in diamond show distinct ESRs, and thus are sensitive to MW radiation even with very low power, compare Chapter 6. Therefore, Ryab, which has a high concentration of NV^-, was used to detect the MW emitted by

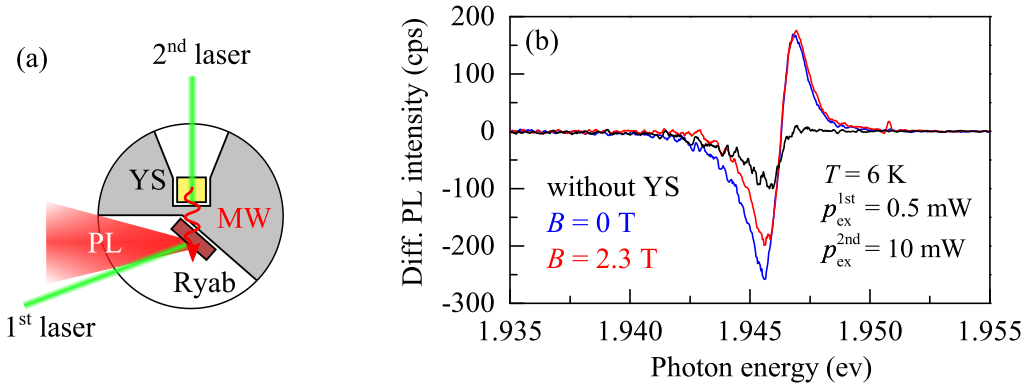

Figure 8-3: (a) Excitation scheme of MW source YS and probe Ryab. The 1st laser is blocked by the Torlon barrier. Only the microwaves (red waved arrow) pass through and induce ESR in Ryab. (b) Differential spectra of the NV^- PL in Ryab. Additional illumination of the Torlon barrier (black) or YS (blue and red) leads to a shift of the ZPL to higher energies.

YS.

A sketch of the sample holder made from black Torlon, a high performance thermoplastic (Polyamide-imide) which is fairly transparent for MW radiation[126], is shown in Fig. 8-3 (a). The MW source YS (yellow) is separated from the MW probe Ryab (dark red) by an 1 mm thick barrier (gray). For excitation a laser (green) operating at 2.33 eV is used. With a beam splitter the laser emission is divided in two parts, henceforth referred to as the 1st and the 2nd laser. While the 1st excites Ryab, the 2nd laser is used to induce MW emission in YS. Note that YS is placed in a hollow in order to shield Ryab from any stray light of the 2nd laser.

The PL (red) of Ryab, dominated by the NV^- ZPL with an intensity of about 10 kcps, is measured with and without additional excitation of YS; the differential spectrum is shown in Fig. 8-3 (b) for two magnetic field strengths. Note that at a magnetic field of $B = 0$ T a small residual magnetic field of a few mT remains. However, at such a small magnetic field (blue line), one would expect no MW emission from YS. The observed shift of the NV^- ZPL to higher energies is a result of the temperature increase in the VTI due to additional illumination of YS with the 2nd laser, which is about 20 times more intense than the 1st laser. Despite the fact that both samples are separated by the Torlon barrier and emerged in a flow of cold helium gas, the heating effect of the 2nd laser seems to be significant. Even when the second laser is not focused on YS, but only on the thick Torlon barrier, a shift of the NV^- ZPL energy is seen, compare black line in Fig. 8-3 (b). At a magnetic field of $B = 2.3$ T the differential spectrum (red line) looks very similar to the 0 T spectrum. Therefore, evidence for an ESR in Ryab is absent. Additional measurements at magnetic fields ranging from 1.9 to 2.35 T (data not shown) provide no indication of ODMR either. Hence, the observed energy shifts are most likely just heating effects. Thus, there is no evidence for MW emission from YS. However, this might be due to the fact that the power of the emitted

MWs is too small, or that the MWs are mainly emitted in a direction distinct from the laser excitation axis. Moreover, the frequency range of the emitted MWs could be very narrow. So, there is no magnetic field at which the energy of the MWs emitted by YS equals the energy of a transition between the spin states of the NV^- centers in Ryab, and hence the resonance condition for ODMR is not fulfilled. This is, however, rather unlikely, since the MW amplification observed in YS is quite wide, compare Fig. 8-1.

Concluding, one can say that there is no evidence for optical induced microwave emission from defect centers in diamond. However, when seeded with 60 GHz MW, a strong amplification can be observed at 2.21 T, which can be attributed to nitrogen impurities. Therefore, defect centers in diamond are still promising candidates for a solid-state maser operating at room temperature.

List of Figures

Symbols and abbreviations

Symbol	Meaning
α	phase shift of sample rotation angle
A_{F}	amplitude of Fano resonance
arb. u.	arbitrary units
B	magnetic field strength
$\mathbf{B}$	magnetic field
BP	diamond crystal „Black Pyramid“
°C	degree Celsius
$\mathrm{C}_{3(\mathrm{v})}$	point group with trigonal symmetry
C	carbon (atom)
CB	conduction band
CCD	charge-coupled device
cps	counts per second
CVD	chemical vapor deposition
CW	continuous wave
δ_0	zero field splitting
D01	diamond crystal
$\mathrm{D}_{2\mathrm{d}}$	point group with tetragonal symmetry
DC7	diamond crystal
ΔE_σ	energy difference of ZPLs excited by σ^+ and σ^- polarized light

ΔE_{ens}	energy shift of the NV center ensemble's ZPL
ΔE_{Z}	zeeman shift
ΔE_{ZPL}	difference of the opposingly circularly polarized ZPL energies
$\Delta\phi_0$	phase shift of sample rotation angle
ΔI_{sub}	ZPL intensity change of an NV center subset
e	Euler's number
E_{ex}	energy of excitation laser
E_{MW}	microwave energy
EPR	electron spin resonance
ESR	electron paramagnetic resonance
E_{ZPL}	energy of the zero phonon line
eV	electron volt
ϕ	sample rotation angle
ϕ_0	phase shift
fcc	face centered cubic
FWHM	full width at half maximum
g	g-factor
$g_{L(S)}$	effective orbital (spin) g-factor
h	Planck constant ($4.1357 \cdot 10^{-15}$ eVs)
H_{L}	ZPL amplification determined by Lorentzian fit
HPHT	high pressure high temperature synthesis
Hz	Hertz
i	imaginary unit
$I_{(\mathrm{ZPL})}$	(zero phonon line) intensity
I_{ex}	power density of exciting laser
K	Kelvin

L	orbital angular momentum quantum number
L_{ZPL}	luminescence efficiency
λ	wavelength
m	meter
m_{L}	orbital angular momentum projection
min	minute
m_{S}	spin projection
μ_{B}	Bohr magneton ($5.7884 \cdot 10^{-5}$ eVT^{-1})
N	nitrogen (atom)
ν	thickness
Nd:YVO_4	Neodymium-doped yttrium orthovanadate
NV	nitrogen vacancy
$NV^{-(0)}$	negatively charged (neutral) nitrogen vacancy
NVRef	diamond crystal „NV reference“
ODMR	optically detected magnetic resonance
π	linearly (polarized) or mathematical constant
P1	single nitrogen defect (center)
P_{c}^{σ}	magnetic field induced circular polarization
P_{c}^{π}	degree of circular polarization
p_{ex}	power of excitation laser
PL	photoluminescence
PLE	photoluminescence excitation
P_{lin}	linear polarization degree
p_{MW}	microwave power
P_{oo}	optical orientation
ppm	parts per million
PSB	phonon side band
q_{F}	Fano factor

ρ_{NV}	concentration of NV centers
Ryab	diamond crystal „Ryabzev2“
S	spin quantum number
s	second
$S_{0,1,2,3}$	Stokes parameter
$\sigma^{+(-)}$	rigth (left) circularly (polarized)
SST	singlet state transition
T	Tesla
T	temperature
t	time
τ	lifetime
θ	rotation of the polarization plane
θ_{F}	Faraday rotation angle
$\mathrm{T_d}$	point group with tetrahedral symmetry
V	Volt
V	Verdet constant
V^0	neutral single vacancy
VB	valance band
VTI	variable temperature inset
W	Watt
w_{F}	width of Fano resonance
w_{L}	width of resonance fitted by Lorentzian function
x,y,z	Cartesian coordinate system axes
YS	diamond crystal „Yellow Submarine“
ZPL	zero-phonon line

Bibliography

[1] J. M. Cork, *Induced color in crystals by deuteron bombardement*, Phys. Rev. **62**, 80 (1942).

[2] F. P. Bundy, H. T. Hall, H. M. Strong, and R. H. Wentorf, *Man-made diamonds*, Nature **176**, 51 (1955).

[3] C. D. Clark, R. W. Ditchburn, and H. B. Dyer, *The absorption spectra of irradiated diamonds after heat treatment*, Proc. R. Soc. A **237**, 75 (1956).

[4] H. B. Dyer, F. A. Raal, L. du Preez, and J. H. N. Loubser, *Optical absorption features associated with paramagnetic nitrogen in diamond*, Philos. Mag. **11**, 763 (1964).

[5] L. du Preez, *Electron paramagnetic resonance and optical investigations of defect centres in diamond*, PhD thesis, University of the Witwatersrand (1965).

[6] G. Davies and M. F. Hamer, *Optical studies of the 1.945 eV vibronic band in diamond*, Proc. R. Soc. Lond. A **348**, 285 (1976).

[7] J. H. N. Loubser and van Wyk J. A., *Electron spin resonance in the study of diamond*, Rep. Prog. Phys. **41**, 1203 (1978).

[8] E. van Oort, N. B. Manson, and M. Glasbeek, *Optically detected spin coherence of the diamond N-V centre in its triplet ground state*, J. Phys. C **21**, 4385 (1988).

[9] E. van Oort, P. Stroomer, and M. Glasbeek, *Low-field optically detected magnetic resonance of a coupled triplet-doublet defect pair in diamond*, Phys. Rev. B **42**, 8605 (1990).

[10] J. A. Wyk, O. D. Tucker, M. E. Newton, J. M. Baker, W. G. S., and P. Spear, *Magnetic-resonance measurements on the $^5A_2$ excited state of the neutral vacancy in diamond*, Phys. Rev. B **52**, 12657 (1995).

[11] F. T. Charnock and T. A. Kennedy, *Combined optical and microwave approach for performing quantum spin operations on the nitrogen-vacancy center in diamond*, Phys. Rev. B **64**, 041201 (2001).

[12] L. Childress, M. V. Gurudev Dutt, J. M. Taylor, A. S. Zibrov, F. Jelezko, J. Wrachtrup, P. P. Hemmer, and M. D. Lukin, *Coherent dynamics of coupled electron and nuclear spin qubits in diamond*, Science **314**, 281 (2006).

[13] P. C. Maurer, G. Kucsko, C. Latta, L. Jiang, N. Y. Yao, S. D. Bennett, F. Pastawski, D. Hunger, N. Chisholm, M. Markham, D. J. Twitchen, J. I. Cirac, and M. D. Lukin, *Room-temperature quantum bit memory exceeding one second*, Science **336**, 1283 (2012).

[14] N. Bar-Gill, L. M. Pham, A. Jarmola, D. Budker, and R. L. Walsworth, *Solid-state electronic spin coherence time approaching one second*, Nat. Commum. **4**, 1743 (2013).

[15] P. G. Brooke, *Decoherence-free quantum-information processing using dipole-coupled qubits*, Phys. Rev. A **75**, 022320 (2007).

[16] M. V. G. Dutt, L. Childress, L. Jiang, E. Togan, J. Maze, F. Jelezko, A. S. Zibrov, P. R. Hemmer, and M. D. Lukin, *Quantum register based on individual electronic and nuclear spin qubits in diamond*, Science **316**, 1312 (2007).

[17] E. Togan, Y. Chu, A. S. Trifonov, L. Jiang, J. Maze, L. Childress, M. V. G. Dutt, A. S. Sorensen, P. R. Hemmer, A. S. Zibrov, and M. D. Lukin, *Quantum entanglement between an optical photon and a solid-state spin qubit*, Nature **466**, 730 (2010).

[18] J. Meijer, B. Burchard, M. Domhan, C. Wittmann, T. Gaebel, I. Popa, F. Jelezko, and J. Wrachtrup, *Generation of single color centers by focused nitrogen implantation*, Appl. Phys. Lett. **87**, 261909 (2005).

[19] D. Scarabelli, M. Trusheim, O. Gaathon, D. Englund, and S. J. Wind, *Nanoscale engineering of closely-spaced electronic spins in diamond*, Nano Lett. **16**, 037601 (2017).

[20] M. Hirose and C. P., *Coherent feedback control of a single qubit in diamond*, Nature **532**, 77 (2016).

[21] F. Dolde, H. Fedder, M. W. Doherty, T. Nöbauer, F. Rempp, G. Balasubramanian, T. Wolf, F. Reinhard, L. C. L. Hollenberg, F. Jelezko, and J. Wrachtrup, *Electric-field sensing using single diamond spins*, Nat. Phys. **7**, 459 (2011).

[22] F. Shi, Q. Zhang, P. Wang, H. Sun, J. Wang, X. Rong, M. Chen, C. Ju, F. Reinhard, H. Chen, J. Wrachtrup, J. Wang, and J. Du, *Single-protein spin resonance spectroscopy under ambient conditions*, Science **347**, 1135 (2015).

[23] P. Ovartchaiyapong, K. W. Lee, B. A. Myers, and A. C. Bleszynski Jayich, *Dynamic strain-mediated coupling of a single diamond spin to a mechanical resonator*, Nat. Commun. **5**, 4429 (2014).

[24] D. Le Sage, K. Arai, D. R. Glenn, S. J. DeVience, L. M. Pham, L. Rahn-Lee, M. D. Lukin, A. Yacoby, A. Komeili, and R. L. Walsworth, *Optical magnetic imaging of living cells*, Nature **496**, 486 (2013).

[25] J. R. Maze, P. L. Stanwix, J. S. Hodges, S. Hong, J. M. Taylor, P. Cappellaro, L. Jiang, M. V. G. Dutt, E. Togan, A. S. Zibrov, A. Yacoby, R. L. Walsworth, and M. D. Lukin, *Nanoscale magnetic sensing with an individual electronic spin in diamond*, Nature **455**, 644 (2008).

[26] L. P. McGuinness, Y. Yan, A. Stacey, D. A. Simpson, L. T. Hall, D. Maclaurin, S. Prawer, P. Mulvaney, J. Wrachtrup, F. Caruso, R. E. Scholten, and L. C. L. Hollenberg, *Quantum measurement and orientation tracking of fluorescent nanodiamonds inside living cells*, Nat. Nanotechnol. **6**, 358 (2011).

[27] G. Kucsko, P. C. Maurer, N. Y. Yao, M. Kubo, H. J. Noh, P. K. Lo, H. Park, and M. D. Lukin, *Nanometre-scale thermometry in a living cell*, Nature **500**, 54 (2013).

[28] K. Beha, A. Batalov, N. B. Manson, R. Bratschitsch, and A. Leitenstorfer, *Optimum photoluminescence excitation and recharging cycle of single nitrogen-vacancy centers in ultrapure diamond*, Phys. Rev. Lett. **109**, 097404 (2012).

[29] R. Gross and A. Marx, *Festkörperphysik*, Wissenschaftsverlag, Oldenbourg (2012).

[30] J. Walker, *Optical absorption and luminescence in diamond*, Rep. Prog. Phys. **42**, 1605 (1979).

[31] E. Gaillou, J. E. Post, D. Rost, and J. E. Butler, *Boron in natural type IIb blue diamonds: Chemical and spectroscopic measurements*, Am. Mineral. **97**, 1 (2012).

[32] E. I. Erlich and W. D. Hausel, *Diamond deposits*, Society for Mining, Metallurgy, and Exploration, Littleton (2002).

[33] H. Kanda, M. Akaishi, and S. Yamaoka, *Synthesis of diamond with the highest nitrogen concentration*, Diam. Relat. Mater. **8**, 1441 (1999).

[34] J. Isberg, J. Hammersberg, E. Johansson, T. Wikström, D. J. Twitchen, A. J. Whitehead, S. E. Coe, and G. A. Scarsbrook, *High carrier mobility in single-crystal plasma-deposited diamond*, Science **297**, 1670 (2002).

[35] N. Mizuochi, J. Isoya, J. Niitsuma, T. Sekiguchi, H. Watanabe, H. Kato, T. Makino, H. Okushi, and S. Yamasaki, *Isotope effects between hydrogen and deuterium microwave plasmas on chemical vapor deposition homoepitaxial diamond growth*, J. Appl. Phys. **101**, 103501 (2007).

[36] F. Jelezko and J. Wrachtrup, *Single defect centres in diamond: A review*, Phys. Stat. Sol. **13**, 3207 (2006).

[37] A. T. Collins, *The detection of colour-enhanced and synthetic gem diamonds by optical spectroscopy*, Diam. Relat. Mater. **12**, 1976 (2002).

[38] A. Zaitsev, *Optical properties of diamond*, Springer-Verlag, Berlin Heidelberg (2001).

[39] G. F. Koster, J. O. Dimmock, R. C. Wheeler, and H. Statz, *Properties of the thirty-two point groups*, M.I.T. Press, Cambridge, Massachusetts (1963).

[40] M. Tinkham, *Group theory and quantum mechanics*, McGraw-Hill, New York (1964).

[41] R. Robertson, J. J. Fox, and A. E. Martin, *Further work on two types of diamond*, Proc. R. Soc. A **157**, 579 (1936).

[42] Y. Mita, *Change of absorption spectra in type-I b diamond with heavy neutron irradiation*, Phys. Rev. B **53**, 11360 (1996).

[43] K. Iakoubovskiia, G. J. Adriaenssensa, N. N. Dogadkinb, and A. A. Shiryaev, *Optical characterization of some irradiation-induced centers in diamond*, Diam. Relat. Mater. **10**, 18 (2001).

[44] M. Lannoo and A. M. Stoneham, *The optical absorption of the neutral vacancy in diamond*, J. Phys. Chem. Solids **29**, 1987 (1968).

[45] A. Zelferino, S. Salustro, J. Baima, V. Lacivita, R. Orlando, and R. Dovesi, *The electronic states of the neutral vacancy in diamond: A quantum mechanical approach*, Theor. Chem. Acc. **135**, 74 (2016).

[46] M. W. Doherty, N. B. Manson, P. Delaney, and L. C. L. Hollenberg, *The negatively charged nitrogen-vacancy centre in diamond: the electronic solution*, New J. Phys. **13**, 025019 (2010).

[47] A. Lenef and S. C. Rand, *Electronic structure of the NV center in diamond: Theory*, Phys. Rev. B **53**, 13441 (1996).

[48] H. Haken and H. C. Wolf, *Molekülphysik und Quantenchemie*, Springer-Verlag, Berlin Heidelberg (1992).

[49] M. S. Dresselhaus, G. Dresselhaus, and A. Jorio, *Group theory: Application to the physics of condensed matter*, Springer-Verlag, Berlin Heidelberg (2008).

[50] L. J. Rogers, S. Armstrong, M. J. Sellars, and N. B. Manson, *Infrared emission of the NV center in diamond: Zeeman and uniaxial stress studies*, New J. Phys. **10**, 103024 (2008).

[51] G. D. Fuchs, V. V. Dobrovitski, R. Hanson, A. Batra, C. D. Weis, T. Schenkel, and D. D. Awschalom, *Excited-state spectroscopy using single spin manipulation in diamond*, Phys. Rev. Lett. **101**, 117601 (2008).

[52] M. W. Doherty, F. Dolde, H. Fedder, F. Jelezko, J. Wrachtrup, N. B. Manson, and L. C. L. Hollenberg, *Theory of the ground-state spin of the NV^- center in diamond*, Phys. Rev. B **85**, 205203 (2012).

[53] N. R. S. Reddy, N. B. Manson, and E. R. Krausz, *Two-laser spectral hole burning in a colour centre in diamond*, J. Lum. **38**, 46 (1987).

[54] F. Jelezko, I. Popa, A. Gruber, C. Tietz, J. Wrachtrup, A. Nizovtsev, and S. Kilin, *Single spin states in a defect center resolved by optical spectroscopy*, Appl. Phys. Lett. **81**, 2160 (2002).

[55] P. Delaney, J. C. Greer, and J. A. Larsson, *Spin-Polarization mechanisms of the nitrogen-vacancy center in diamond*, Nano Lett. **10**, 610 (2010).

[56] A. Gali, *Theory of the neutral nitrogen-vacancy center in diamond and its application to the realization of a qubit*, Phys. Rev. B **79**, 235210 (2009).

[57] S. Felton, A. M. Edmonds, M. E. Newton, P. M. Martineau, D. Fisher, and D. J. Twitchen, *Electron paramagnetic resonance studies of the neutral nitrogen vacancy in diamond*, Phys. Rev. B **77**, 081201 (2008).

[58] P. Siyushev, H. Pinto, M. Vörös, A. Gali, F. Jelezko, and J. Wrachtrup, *Optically controlled switching of the charge state of a single nitrogen-vacancy center in diamond at cryogenic temperatures*, Phys. Rev. Lett. **110**, 167402 (2013).

[59] N. B. Manson, K. Beha, A. Batalov, L. J. Rogers, M. W. Doherty, R. Bratschitsch, and A. Leitenstorfer, *Assignment of the NV^0 575-nm zero-phonon line in diamond to a ^2E-$^2A_2$ transition*, Phys. Rev. B **87**, 155209 (2013).

[60] C. A. Coulson and M. J. Kearsley, *Colour centers in irradiated diamonds. I*, Proc. R. Soc. A **241**, 433 (1957).

[61] T. A. Kennedy, F. T. Charnock, J. S. Colton, J. E. Butler, R. C. Linares, and D. P. J., *Single-qubit operations with the nitrogen-vacancy center in diamond*, Phys. Status Solidi B **233**, 416 (2002).

[62] W. Friedrich, P. Knipping, and M. von Laue, *Interferenz-Erscheinungen bei Röntgenstrahlen*, Bayerische Akademie der Wissenschaften, Sitzungsberichte p. 303 (1912).

[63] R. S. Krishnan, *Raman spectrum of diamond*, Nature **155**, 171 (1945).

[64] S. A. Solin and A. K. Ramdas, *Raman spectrum of diamond*, Phys. Rev. B **1**, 1687 (1970).

[65] D. Braukmann, E. R. Glaser, T. A. Kennedy, M. Bayer, and J. Debus, *Circularly polarized zero-phonon transitions of vacancies in diamond at high magnetic fields* (submitted).

[66] P. Tamarat, N. B. Manson, J. P. Harrison, R. L. McMurtrie, A. Nizovtsev, C. Santori, R. G. Beausoleil, P. Neumann, T. Gaebel, F. Jelezko, P. Hemmer, and J. Wrachtrup, *Spin-flip and spin-conserving optical transitions of the nitrogen-vacancy centre in diamond*, New J. Phys. **10**, 045004 (2008).

[67] M. W. Doherty, N. B. Manson, P. Delaney, F. Jelezko, J. Wrachtrup, and L. C. L. Hollenberg, *The nitrogen-vacancy colour centre in diamond*, Phys. Rep. **528**, 1 (2013).

[68] J. R. Maze, A. Gali, E. Togan, Y. Chu, E. Kaxiras, and M. D. Lukin, *Properties of nitrogen-vacancy centers in diamond: the group theoretic approach*, New J. Phys. **13**, 025025 (2011).

[69] A. Batalov, V. Jacques, F. Kaiser, P. Siyushev, P. Neumann, L. J. Rogers, R. L. McMurtrie, N. B. Manson, F. Jelezko, and J. Wrachtrup, *Low temperature studies of the excited-state structure of negatively charged nitrogen-vacancy color centers in diamond*, Phys. Rev. Lett. **102**, 195506 (2009).

[70] R. J. Epstein, K. Y. K. Mendoza, F. M. and, and D. D. Awschalom, *Anisotropic interactions of a single spin and dark-spin spectroscopy in diamond*, Nat. Phys. **1**, 94 (2005).

[71] J. P. D. Martin, *Fine structure of excited* ^3E *state in nitrogen-vacancy centre of diamond*, J. Lum. **81**, 237 (1999).

[72] L. J. Rogers, R. L. McMurtrie, M. J. Sellars, and N. B. Manson, *Time-averaging within the excited state of the nitrogen-vacancy centre in diamond*, New J. Phys. **11**, 063007 (2009).

[73] H. Hanzawa, H. Nishikori, Y. Nisida, S. Sato, T. Nakashima, S. Sasaki, and N. Miura, *Zeeman effect on the zero-phonon line of the NV center in synthetic diamond*, Physica B **184**, 137 (1993).

[74] M. Thuau and J. Margerie, *A theoretical calculation of the orbital g-factor of the excited state of F-centres in alkali halides*, Phys. Stat. Sol. **47**, 271 (1971).

[75] I. N. Douglas and W. A. Runciman, *The magnetic circular dichroism spectrum of the GR1 line in irradiated diamonds*, J. Phys. C **10**, 2253 (1977).

[76] J. E. Lowther and A. M. Stoneham, *Theoretical implications of the stress and magnetic field splitting of the GR1 line in diamond*, J. Phys. C **11**, 2165 (1978).

[77] J. C. A. Prentice, B. Monserrat, and R. J. Needs, *First-principles study of the dynamic Jahn-Teller distortion of the neutral vacancy in diamond*, Phys. Rev. B **95**, 014108 (2017).

[78] D. H. Goldstein, *Polarized light*, CRC Press, Boca Raton (2012).

[79] W. J. Ossau and R. Suris, *Optical properties of 2D systems with interacting electrons*, Springer Science+Business Media, Dordrecht (2003).

[80] D. Braukmann, V. P. Popov, E. R. Glaser, T. A. Kennedy, M. Bayer, and J. Debus, *Anisotropies in the linear polarization of vacancy photoluminescence in diamond induced by crystal rotation and strong magnetic fields* (submitted).

[81] N. Diep Lai, D. Zheng, F. Jelezko, F. Treussart, and J.-F. Roch, *Influence of a static magnetic field on the photoluminescence of an ensemble of nitrogen-vacancy color centers in a diamond single-crystal*, Appl. Phys. Lett. **95**, 133101 (2009).

[82] V. Kolotovska, M. Friedrich, D. R. T. Zahn, and G. Salvan, *Magnetic field influence on the molecular alignment of vanadyl phthalocyanine thin films*, J. Cryst. Growth **291**, 166 (2006).

[83] K. K. Hansen, D. V. Fedorov, A. S. Jensen, and N. T. Zinner, *Classical crystal formation of dipoles in two dimensions*, Phys. Scr. **90**, 125002 (2015).

[84] S. C. Rand, *Lectures on light - Nonlinear and quantum optics using the density matrix*, Oxford University Press (2016).

[85] L. D. Landau and E. M. Lifshitz, *The classical theory of fields*, Pergamon Press, Oxford (1975).

[86] M. A. Alekseev, I. Y. Karlik, I. A. Merkulov, D. N. Mirlin, Y. T. Rebane, and V. F. Sapega, *Anisotropy of the linear polarization of hot photoluminescence emitted by p-type GaAs*, Sov. Phys. Solid State **27**, 1589 (1985).

[87] J. Mossbrucker and T. A. Grotjohn, *Determination of local crystal orientation of diamond using polarized Raman spectra*, Diam. Relat. Mater. **5**, 1333 (1996).

[88] K. C. Fu, C. Santori, P. E. Barclay, L. J. Rogers, N. B. Manson, and R. G. Beausoleil, *Observation of the dynamic Jahn-Teller effect in the excited states of nitrogen-vacancy centers in diamond*, Phys. Rev. Lett. **103**, 256404 (2009).

[89] T. Plakhotnik, M. W. Doherty, and N. B. Manson, *Electron-phonon processes of the nitrogen-vacancy center in diamond*, Phys. Rev. B **92**, 081203(R) (2015).

[90] A. Gali, T. Simon, and J. E. Lowther, *An ab initio study of local vibration modes of the nitrogen-vacancy center in diamond*, New. J. Phys. **13**, 025016 (2011).

[91] T. A. Abtew, Y. Y. Sun, B. Shih, P. Dev, S. B. Zhang, and P. Zhang, *Dynamic Jahn-Teller effect in the NV^- center in diamond*, Phys. Rev. Lett. **107**, 146403 (2011).

[92] V. Hizhnyakov and P. Reineker, *Optical dephasing in defect-rich crystals*, J. Chem. Phys. **111**, 8131 (1999).

[93] V. Hizhnyakov, H. Kaasik, and I. Sildos, *Zero-phonon lines: the effect of a strong softening of elastic springs in the excited state*, Phys. Stat. Sol. (B) **234**, 644 (2002).

[94] B. Di Bartolo, *Optical interactions in solids*, John Wiley& Sons, New York (1968).

[95] A. K. Patnaik and G. S. Agarwal, *Laser field induced birefringence and enhancement of magneto-optical rotation*, Optics Communications **179**, 97 (2000).

[96] A. I. Savchuk, I. D. Stolyarchuk, V. V. Makoviy, and O. A. Savchuk, *Magneto-optical Faraday rotation of semiconductor nanoparticles embedded in dielectric matrices*, Appl. Optics **53**, B22 (2014).

[97] I. Prigogine and S. A. Rice, *Advances in chemical physics*, John Wiley& Sons, New York (1976).

[98] D. Braukmann, I. N. Kupriyanov, Y. N. Palyanov, B. H. Bairamov, V. P. Popov, E. R. Glaser, T. A. Kennedy, M. Bayer, and J. Debus, *Fano effect in ensembles of NV centers in diamond under resonant excitation conditions* (in preparation).

[99] U. Fano, *Effects of configuration interaction on intensities and phase shifts*, Phys. Rev. **124**, 1866 (1961).

[100] L. Robledo, H. Bernien, I. van Weperen, and R. Hanson, *Control and coherence of the optical transition of single nitrogen vacancy centers in diamond*, Phys. Rev. Lett. **105**, 177403 (2010).

[101] F. J. Heremans, G. D. Fuchs, C. F. Wang, R. Hanson, and D. D. Awschalom, *Generation and transport of photoexcited electrons in single-crystal diamond*, Appl. Phys. Lett. **94**, 152102 (2009).

[102] L. A. Hemstreet, C. Y. Fong, and M. L. Cohen, *Calculation of the band structure and optical constants of diamond using the nonlocal-pseudopotential method*, Phys. Rev. B **2**, 2054 (1970).

[103] S. Dhomkar, J. Henshaw, H. Jayakumar, and C. A. Meriles, *Long-term data storage in diamond*, Science Advances **2** (2016).

[104] W. B. Fowler, *Physics of color centers*, Academic Press Inc., New York (1968).

[105] W. B. Fowler, *Relaxation of the excited F center*, Phys. Rev. **135**, A1725 (1964).

[106] M. Kroner, A. O. Govorov, S. Remi, B. Biedermann, S. Seidl, A. Badolato, P. m. Petroff, W. Zhang, R. Barbour, B. D. Gerardot, R. J. Warburton, and K. Karrai, *The nonlinear Fano effect*, Nature **451**, 311 (2008).

[107] P. Neumann, R. Kolesov, V. Jacques, J. Beck, J. Tisler, A. Batalov, L. Rogers, N. B. Manson, G. Balasubramanian, F. Jelezko, and J. Wrachtrup, *Excited-state spectroscopy of single NV defects in diamond using optically detected magnetic resonance*, New J. Phys. **11**, 013017 (2009).

[108] D. Braukmann, Y. V. Ivanov, E. R. Azamat, E. R. Glaser, T. A. Kennedy, D. R. Yakovlev, M. Godlewski, M. Bayer, and J. Debus, *Photoluminescence response of the NV^- ensemble in diamond on ultra low power 60-GHz microwave excitation in a diamond crystal* (in preparation).

[109] A. Abragam, *Principles of nuclear magnetism*, Oxford University Press (1961).

[110] T. P. M. Alegre, C. Santori, G. Medeiros-Ribeiro, and R. G. Beausoleil, *Polarization-selective excitation of nitrogen vacancy centers in diamond*, Phys. Rev. B **76**, 165205 (2007).

[111] L. M. Pham, N. Bar-Gill, D. Le Sage, C. Belthangady, A. Stacey, M. Markham, D. J. Twitchen, M. D. Lukin, and R. L. Walsworth, *Enhanced metrology using preferential orientation of nitrogen-vacancy centers in diamond*, Phys. Rev. B **86**, 121202 (2012).

[112] W. Stewart, L. J. Challis, L. W. Barclay, M. N. Barton, C. Blakemore, D. N. M. Coggon, D. Cox, J. Fellows, M. Repacholi, M. Rugg, A. J. Swerdlow, and T. R. K. Varma, *Mobile phones and health*, Independent expert group on mobile phones (2000).

[113] K. Jensen, V. M. Acosta, A. Jarmola, and D. Budker, *Light narrowing of magnetic resonances in ensembles of nitrogen-vacancy centers in diamond*, Phys. Rev. B **87**, 014115 (2013).

[114] J. P. D. Martin, N. B. Manson, D. C. Doetschman, M. J. Sellars, R. Neuhaus, and E. Wilson, *Spectral hole burning and Raman heterodyne signals associated with an avoided crossing in the NV centre in diamond*, J. Lumin. **86**, 355 (2000).

[115] J. P. Gordon, H. J. Zeiger, and C. H. Townes, *The maser - New type of microwave amplifier, frequency standard, and spectrometer*, Phys. Rev. **99**, 1264 (1955).

[116] M. S. Reid, *Low-noise systems in the deep space network*, Wiley (2008).

[117] S. B. Crampton, H. E. Peters, H. Berg, N. Ramsey, R. F. C. Vessot, J. Vanier, and D. Kleppner, *Hydrogen-maser principles and techniques*, Phys. Rev. **138**, A972 (1965).

[118] A. E. Siegman, *Microwave solid-state masers*, McGraw-Hill (1964).

[119] M. Oxborrow, J. D. Breeze, and N. M. Alford, *Room-temperature solid-state maser*, Nature **488**, 353 (2012).

[120] S. Bogatko, P. D. Haynes, J. Sathian, J. Wade, J.-S. Kim, K.-J. Tan, J. Breeze, E. Salvadori, A. Horsfield, and M. Oxborrow, *Molecular design of a room-temperature maser*, J. Phys. Chem. C **120**, 8251 (2016).

[121] H. Kraus, V. A. Soltamov, D. Riedel, S. Väth, F. Fuchs, A. Sperlich, P. G. Baranov, V. Dyakonov, and G. V. Astakhov, *Room-temperature quantum microwave emitters based on spin defects in silicon carbide*, Nat. Phys. **10**, 157 (2014).

[122] L. Jin, M. Pfender, N. Aslam, P. Neumann, S. Yang, J. Wrachtrup, and R.-B. Liu, *Proposal for a room-temperature diamond maser*, Nat. Commum. **6**, 8251 (2015).

[123] V. A. Nadolinny, A. P. Yelisseyev, J. M. Baker, D. J. Twitchen, M. E. Newton, A. Hofstaetter, and B. Feigelson, *EPR spectra of separated pairs of substitutional nitrogen atoms in diamond with a high concentration of nitrogen*, Phys. Rev. B **60**, 5392 (1999).

[124] M. K. Kneip, D. R. Yakovlev, M. Bayer, A. A. Maksimov, I. I. Tartakovskii, D. Keller, W. Ossau, L. W. Molenkamp, and A. Waag, *Spin-lattice relaxation of Mn-ions in ZnMnSe/ZnBeSe quantum wells measured under pulsed photoexcitation.*, Phys. Rev. B **73**, 045305 (2006).

[125] H. Ibach and H. Lüth, *Festkörperphysik*, Springer-Verlag, Berlin Heidelberg (2009).

[126] *The New Materials Society: Challenges and opportunities. New materials science and technology*, Bd. 2, U.S. Department of the Interior (1990).

Acknowledgments

First of all, I would like to thank Prof. Manfred Bayer for giving me the opportunity to execute my PhD at his chair and for his multifarious support. My greatest appreciation goes to my supervisor and mentor Dr. Jörg Debus, who inspired and guided me since my early years at the university. During my bachelor studies he and Dr. Daniel Dunker introduced me to the world of optical spectroscopy and taught me everything I had to know about the work in a laser laboratory. During my master and PhD thesis, his ongoing support as my supervisor was invaluable for my daily work, be it performing measurements or writing scientific papers. Thanks for your sedulous effort and the fun times we had. In this regard, I also want to thank my coworkers of the CW lab, Henning Moldenhauer, Janina Rautert, and Janina Schindler, who all contributed to this work in one way or another. I owe special thanks to my classmate and competitor Dennis Kudlacik, who accompanied me on my academic journey ever since the math classes before the start of our first semester and who was always a reliable office and laboratory neighbor. I'm very grateful to Prof. Dietmar Fröhlich for our fruitful discussions, which vastly extended my understanding of group theory and color-center physics.

Furthermore, I want to thank all the other members of our chair for the fruitful atmosphere and the fun times we had in Dortmund as well as abroad at the numerous conferences we visited together. In this context, my thanks also goes to our colleagues at the Ioffe institute in Russia with whom I spent my research stays. Special thanks goes to Prof. Bakhysh Bairamov for the warm welcome to his laboratory and home as well as for his never ending ideas for novel research aspects. I would like to thank Prof. Vladimir Popov as well as Dr. Evan Glaser and Dr. Tom Kennedy for providing various diamond samples. Moreover, I thank Dr. Dimitri Azamat for his theoretical calculations and Dr. Vitalii Ivanov as well as Prof. Marek Godlewski for contributing to the ODMR research. In addition to my scientific coworkers, I want to thank our technical staff, Lars Wieschollek, Thomas Stöhr, and Klaus Wiegers for laboratory maintenance and their supportive crafting as well as our secretaries Michaela Wäscher and Nina Collette for shielding me from the bureaucratic struggle.

My special thanks goes to my girlfriend Tina, who patiently supported me even when I stayed late at work. Moreover, I thank all my friends and especially my role-playing mates who offered welcome distraction from writing my thesis. Particularly I am thankful to Lena Uesbeck for proofreading my entire thesis. Last but not least, I want to thank my parents Heike and Hans-Jürgen, as well as my aunt Lisa for their continuous support during my whole academic career.